2017

Engineered quasi-phase matching for nonlinear quantum optics in waveguides

BOSTON UNIVERSITY

COLLEGE OF ENGINEERING

Dissertation

ENGINEERED QUASI-PHASE MATCHING FOR NONLINEAR QUANTUM OPTICS IN WAVEGUIDES

by

MACKENZIE A. VAN CAMP

B.A., Lawrence University, 2009
M.S., Massachusetts Institute of Technology, 2013

Submitted in partial fulfillment of the

requirements for the degree of

Doctor of Philosophy

2017

Approved by

First Reader

Alexander V. Sergienko, Ph.D.
Professor of Electrical and Computer Engineering
Professor of Physics

Second Reader

Anna K. Swan, Ph.D.
Associate Professor of Electrical and Computer Engineering
Associate Professor of Materials Science and Engineering
Associate Professor of Physics

Third Reader

Roberto Paiella, Ph.D.
Professor of Electrical and Computer Engineering
Professor of Materials Science and Engineering

Fourth Reader

Enrico Bellotti, Ph.D.
Professor of Electrical and Computer Engineering
Professor of Materials Science and Engineering

In the face of overwhelming odds, I'm left with only one option:
I'm gonna have to science the shit outta this.

Matt Damon as Mark Watney, *The Martian* (2015)

Acknowledgments

I would like to give my heartfelt thanks to Professor Alexander Sergienko, whose support, expertise, and patience have been invaluable. I am a better scientist and a better person for having worked with him, and he will always have my respect and gratitude.

Many thanks to all my past and present coworkers in the Quantum Communication and Measurement Group. A particular thank you to John Snyder, who programmed the FPGA used in this work and who has been my cleanroom buddy for the last two years, and to Abu Thomas, who helped make and test our first waveguide devices. I would also like to thank Andrew Fraine for showing me the ropes, Casey Fitzpatrick for sharing his enthusiasm about machine learning, and David Simon and Olga Minaeva for their collaboration on publications. To Shuto Osawa, Deniz Aybas, and Nick Nardelli, I would like to express my enthusiasm and optimism for their future careers, and wish them all the best.

This work would not be possible without the wonderful people and facilities present at Boston University. Thank you to Paul Mak of the Optoelectronics Processing Facility for his tireless work to keep everything running at full capacity, Bob Sjostrom at the Engineering Product Innovation Center for machining my grinding mounts with superhuman precision, and the team at the Scientific Instrumentation Facility for making my poling chamber and end-face polishing mounts. Thank you to my committee for their time and feedback, and to all the wonderful staff in the ECE and Photonics Center offices.

Thank you to my friends. To Shannon O'Leary and Adam Clausen, whom I miss terribly. To Ron Walsworth, who was always there with a smile and a hug when I needed advice. To my roommates Andrew and Tanya, who kept me from becoming a complete science hermit. To Meredith and Jim, Michelle and Matt, Rob D. and

Lindsay, Dave and Lori, whose companionship and friendship made the years go by faster.

Thank you to my family, whose confidence in me never wavered.

And thank you most of all to Rob, my partner of over a decade. His love, support, and sacrifices helped me reach this point, and I would like to dedicate this dissertation to him. I love you, Rob. Here's to our next adventure ♡

ENGINEERED QUASI-PHASE MATCHING FOR NONLINEAR QUANTUM OPTICS IN WAVEGUIDES

MACKENZIE A. VAN CAMP

Boston University, College of Engineering, 2017

Major Professor: Alexander V. Sergienko, Ph.D.
Professor of Electrical and Computer Engineering
Professor of Physics

ABSTRACT

Entanglement is the hallmark of quantum mechanics. Quantum entanglement — putting two or more identical particles into a non-factorable state — has been leveraged for applications ranging from quantum computation and encryption to high-precision metrology. Entanglement is a practical engineering resource and a tool for sidestepping certain limitations of classical measurement and communication. Engineered nonlinear optical waveguides are an enabling technology for generating entangled photon pairs and manipulating the state of single photons. This dissertation reports on: i) frequency conversion of single photons from the mid-infrared to 843nm as a tool for incorporating quantum memories in quantum networks, ii) the design, fabrication, and test of a prototype broadband source of polarization and frequency entangled photons; and iii) a roadmap for further investigations of this source, including applications in quantum interferometry and high-precision optical metrology.

The devices presented herein are quasi-phase-matched lithium niobate waveguides. Lithium niobate is a second-order nonlinear optical material and can mediate optical energy conversion to different wavelengths. This nonlinear effect is the basis of both

quantum frequency conversion and entangled photon generation, and is enhanced by i) confining light in waveguides to increase conversion efficiency, and ii) quasi-phase matching, a technique for engineering the second-order nonlinear response by locally altering the direction of a material's polarization vector. Waveguides are formed by diffusing titanium into a lithium niobate wafer. Quasi-phase matching is achieved by electric field poling, with multiple stages of process development and optimization to fabricate the delicate structures necessary for broadband entangled photon generation.

The results presented herein update and optimize past fabrication techniques, demonstrate novel optical devices, and propose future avenues for device development. Quantum frequency conversion from 1848nm to 843nm is demonstrated for the first time, with $> 75\%$ single-photon conversion efficiency. A new electric field poling methodology is presented, combining elements from multiple historical techniques with a new fast-feedback control system. This poling technique is used to fabricate the first chirped-and-apodized Type-II quasi-phase-matched structures in titanium-diffused lithium niobate waveguides, culminating in a measured phasematching spectrum that is predominantly Gaussian ($R^2 = 0.80$), nearly eight times broader than the unchirped spectrum, and agrees well with simulations.

Contents

1 Introduction **1**

1.1 Motivation 1

1.2 The importance of quantum frequency conversion 1

1.3 Customizable spectral and polarization entanglement for high-resolution optical measurements 2

1.4 Summary of the present state of the art 3

1.5 Structure of the dissertation 6

2 Theory **8**

2.1 Nonlinear frequency conversion in $\chi^{(2)}$ materials 8

2.1.1 Origin of nonlinearity in lithium niobate 9

2.1.2 Classical second-order nonlinear processes 10

2.1.3 Phase matching 14

2.2 Quantum processes in $\chi^{(2)}$ materials 17

2.2.1 Quantization of the electromagnetic field 17

2.2.2 Quantum frequency conversion 18

2.2.3 Spontaneous parametric down conversion 18

2.2.3.1 SPDC with engineered poling 19

2.3 Quantum two-photon polarization interferometry 20

2.3.1 Configuration 1: birefringent delay before beamsplitter 21

2.3.2 Configuration 2: birefringent delay after beamsplitter 23

2.3.2.1 Setup and theory 23

2.3.2.2 Even-order dispersion cancellation 23
2.3.2.3 Optimization with genetic algorithms 25

3 Fabrication technology development 28

3.1 Diffused titanium waveguides in lithium niobate 28
3.1.1 Titanium diffusion 28
3.2 Poling lithium niobate 29
3.2.1 Fundamentals of domain inversion 29
3.2.2 Poling dynamics 31
3.2.3 Poling apparatus 32
3.2.4 Poling procedure 34
3.2.4.1 Back-poling after titanium diffusion 34
3.2.4.2 Summary of electrode photolithography 35
3.2.4.3 Poling parameters 37
3.2.4.3.1 QFC samples 38
3.2.4.3.2 First Type-II samples 40
3.2.4.3.3 Nucleation and duty cycle homogeneity . . . 40
3.2.4.3.4 Final apodized Type-II samples 43
3.2.4.4 Dielectric breakdown during poling 44

4 Type-0 QFC in Ti:PPLN 47

4.1 Design and predicted performance 47
4.2 Experiment setup 48
4.3 Results 50

5 Type-II SPDC/SH in Ti:PPLN and two-photon quantum polarization interferometry 52

5.1 Unchirped Type-II 52
5.1.1 SH experiment and results 52

5.1.2 Two-photon interferometry experiment setup 53
5.1.3 Two-photon interferometry results and troubleshooting 54
5.2 Linearly-chirped Type-II 57
5.2.1 SH results 57
5.2.2 Two-photon interferometry results 58
5.3 Apodized chirp Type-II 58
5.3.1 Design of apodized poling 58
5.3.2 SH results 59
5.3.3 SPDC results and troubleshooting 61

6 Roadmap for future technology development 64

6.1 Overcoming spectral phase 64
6.1.1 Origin of spectral phase limitations 64
6.1.2 Asymmetric poling for improved spectral phase 66
6.1.3 Phase correction after pair generation 67
6.2 Alternate fabrication methodologies 69
6.2.1 Poling 70
6.2.1.1 Electrode material 70
6.2.1.2 Surface poling 70
6.2.1.3 Direct writing 71
6.2.1.4 Light-assisted poling 72
6.2.2 Waveguides 72
6.2.2.1 Diffused zinc channel waveguides 72
6.2.2.2 Ridge waveguides 73
6.3 Sensing applications 74
6.4 Plug-and-play quantum optics 74

7 Conclusions 76

A Fabrication instructions **79**

A.1 Summary of steps 79

A.2 Materials 80

A.3 Dicing 81

A.4 Removal of tape residue 82

A.5 3-step cleaning process 82

A.6 Titanium deposition 83

A.6.1 Using the Angstrom system: 84

A.6.2 Using the CHA system: 84

A.7 Lithography: Waveguides 84

A.8 Diffusion 87

A.9 Grinding and back-poling 89

A.10 Nichrome deposition 94

A.11 Lithography: periodic poling 95

A.12 Periodic poling 95

A.13 End-face polishing 96

B Relationship between SPDC and SH bandwidths **99**

B.1 SPDC bandwidth 100

B.2 SH bandwidth 100

B.3 SPDC/SH bandwdth ratio 101

References **102**

Curriculum Vitae **110**

List of Tables

2.1 Possible phase matching configurations for lithium niobate. The d_{eff} values are for congruent LN. 16

5.1 SPDC power loss budget for unchirped Ti:PPLN 2-photon quantum interferometry experiment. 57

5.2 Total waveguide transmission efficiencies for H, V polarized light in the final apodized sample (output power/input power; includes coupling efficiency and scattering loss). 62

A.1 Diffusion procedure 87

List of Figures

2·1 The atomic structure of lithium niobate in the ferroelectric (a, c) and paraelectric (b) phases. The shaded regions ΔLi and ΔNb show the displacement of lithium (gray) and niobium (white) ions from the oxygen (red) sublattice between the para- and ferroelectric phases. This displacement gives rise to the spontaneous polarization P_s, which can be either parallel (a) or antiparallel (c) to the crystal $\vec{c}$ (z) axis (Prezas and Graca, 2016). 10

2·2 Illustration of the electron cloud displacement and resulting potentials for different strength nonlinearities. Figure from (Thomas, 2010). . . 11

2·3 Birefringent (a) and quasi- (b) phase matching for DFG. 14

2·4 Intensity of the ider as a function of crystal length for perfectly phase matched (a), quasi-phase matched (b), and poorly phase matched (c) x-propagating collinear DFG in the absence of walk-off. Figure from (Boyd, 2008). 15

2·5 Illustration of poling with linear chirp. Figure modified from (Fraine, 2015). 20

2·6 Illustration of the two-photon quantum polarization interferometer and expected interferograms for a sample after (A) and before (B) the beamsplitter (Fraine, 2015) 21

2·7 Illustration of the simplest case of Hong-Ou-Mandel-like two-photon polarization interferometry (monochromatic, degenerte signal and idler), with the birefringent delay line after the beamsplitter. 22

3·1 Simulated mode profiles for the Ti:LN waveguides fabricated in this work. The titanium stripe is 7μm wide and 100nm thick before diffusion, and is diffused for 7 hours at 1060C. White lines at $z = 0$ indicate the LN-air interface. TE-like modes have ordinary polarization, and TM-like modes have extraordinary polarization; in the following experiments, these correspond to H- and V-polarized modes. 30

3·2 The stages of domain inversion. Poling is achieved by applying voltage $V \geq V_c$ across the sample via patterned electrodes on the +z face and uniform electrical contact to the -z face (a). Inverted domains nucleate at the edges of the electrodes where the z-component of the electric field is highest (b). The tips of the domains rapidly propagate to the -z face (c) and coalesce under the electrodes (d) before expanding outward at a slower rate (e). 31

3·3 Schematic of the poling chamber. 32

3·4 Diagram of the electric field poling apparatus. The target voltage is set by the FPGA and amplified by a TREK 20/20C high voltage amplifier. The high-voltage signal passes through a 1MΩ current-limiting resistor 33

3·5 Illustration of inverted domain layer after high-temperature titanium diffusion (a), after removal of the inverted layer (b), and after back-poling (c). 35

3·6 Summary of the procedure for fabricating "resist window" electrical contacts for periodic poling. From left to right, resist is spun on to the sample, exposed under UV illumination through a photomask, and developed. After developing, the sample is baked to improve dielectric strength and chemical resistance. 36

3·7 Summary of the procedure for fabricating nickel chromium electrodes under photoresist. Step-by-step fabrication instructions are given in Appendix A. 37
3·8 Poling waveform for QFC samples. Inset shows detail of the mask design and resulting domains. 39
3·9 Zoomed-out image showing regions of patchy poling on the QFC sample shown in Fig. 3·8 39
3·10 Back-poling (a) and periodic poling (b) waveforms for the sample that yielded most of the SPDC and two-photon polarization interferometry results, and a representative image of poling quality in that sample, revealed by etching in HF (c). Inverted domain boundaries are at the outer edge of each oval. The macroscopically patchy poling from Fig. 3·9 is resolved, but there is still a large variation in the duty cycle (59% to 90% in this image). 41
3·11 Demonstration of poling-induced duty cycle inhomogeneity. Each column was poled with a different duty cycle, with period 9.5μm. A section of photomask with a 9.5μm period and three different duty cycles is shown in (a). From left to right the duty cycles are 30%, 25%, and 20%. The photolithography is shown in (b). The domains revealed by HF etching after poling are shown in (c), illustrating the poling-induced non-uniformity of the duty cycle. 42
3·12 Simplified illustration of uneven domain nucleation. Note that the period (measured from center-to-center of the inverted domains) remains constant, but the duty cycle varies. 42

3·13 Diagram of optimized poling waveform for use with NiCr electrodes. Axes are not to scale. The general form of the voltage pulse is based on (Batchko et al., 1999), with the addition of fast feedback and empirical optimization of the static voltage levels and ramp rates. 44

3·14 Back-poling (a) and periodic poling (b) waveforms for the final apodized SPDC methodology, with representative HF-etched domains (c). The vertical lines of dots are regions of swelling on top of the waveguides. The mean duty cycle is $66 \pm 2\%$ 45

4·1 Motivation for QFC experiments (a), and selection of pump wavelength to avoid conversion of Stokes Raman scattering (b). 48

4·2 Setup for QFC experiments. A tunable c-band laser and an EDFA were used to generate wavelength tuning curves and conversion spectra; all other measurements were taken with a pulsed 1550nm laser attenuated through an adjustable fiber attenuator. 49

4·3 From L to R: measured 1550nm TM-like (e), 1550nm TE-like (o), and 843nm TM-like (e) mode profiles. Z and y are crystallographic axes; the waveguide is x-propagating. The 1550nm mode profiles have $> 90\%$ overlap with a standard SMF-28 fiber. 50

4·4 Results of QFC measurements. From L to R: conversion efficiency, signal-to-noise ratio, and wavelength tuning curves. Points are measured data, and lines in (a) and (c) are fits based on the coupled mode equations. The polynomial fit in (b) is to guide the eye. 51

5·1 SH spectrum (a) and intensity as a function of input polarization (b) for an unchirped Type-II sample. SH power is maximized with D or A polarized input, but reduces to zero for H or V, as expected. Blue points are measured data and red lines are simulations. 53

5·2 Setup for 2-photon polarization interferometry experiments. 54
5·3 2-photon polarization interferogram from an unchirped Type-II SPDC sample at 90.5C, integrated for 300s at each point with 1mW of pump power (a), and distinguishability of H, V polarized photons at th end of each arm of the interferometer and immediately after the waveguide (b). Points are measured data, and lines are sinusoidal fits. The poling data for this sample are in Fig. 3·10. 55
5·4 2-photon polarization interferogram from a linearly-chirped (1%) Type-II SPDC sample at 93.5C with 2.5mW pump and integrated for 300s per point (a), and the corresponding SH spectrum (b). Blue points are measured data. The red curve is a sinusoidal fit in (a), and the simulated SH spectrum in (b). The poling data for this sample are in Fig. 3·10. 57
5·5 From left to right: poling profile, simulated SH and SPDC spectra, and interferograms. From top to bottom: unchirped poling, 1% linear chirp, optimal apodized linear chirp, and a simplified apodized chirp designed for easier fabrication. The first 3 designs are in a 16.5mm waveguide, and the easier apodized chirp is in a 10mm waveguide. All are designed for operation at 165C, and all interferograms are comprised of fast, 6.34fs period fringes. 60
5·6 Best SH spectrum obtained from the final batch of apodized samples. The poling data for this sample are in Fig. 3·14 61
5·7 SPDC H, V distinguishability measured at the output of the waveguide in the final apodized sample. The poling data for this sample are in Fig. 3·14. 63

6·1 Different poling profiles along the length x of the nonlinear crystal interaction region. 68

6·2 The SPDC spectrum, phase δ, and the optimized interferogram produced using poling Eq. 2.37 in case of N = 11. The spectral width of the intensity envelope (FWHM) is 135 nm. The inset illustrates a blow-up of the central portion of the plot illustrating clean oscillations inside a smooth envelope. The interferogram visibility is 90.3% and the FWHM is 54fs 69

A·1 Photograph of clean samples taped to the electron beam sample mount, in preparation for titanium deposition. This is a double batch. 83

A·2 Titanium diffusion setup. 88

A·3 Photograph of Ti:LN waveguides after diffusion. The speckles on the top surface are normal, and are presumed to be due to lithium oxide out diffusion. 89

A·4 Mount used for grinding the back face of the sample after titanium diffusion. 90

A·5 Left: the halves of the poling chamber, with gaskets. Right: the assembled poling chamber. 92

A·6 Mount used for end-face polishing. 97

A·7 Microscope image of a polished waveguide end-face 97

List of Abbreviations

A	Anti-diagonal (polarization)
D	Diagonal (polarization)
DAQ	Data Acquisition (module)
DFG	Difference Frequency Generation
E	Extraordinary (polarization)
EDFA	Erbium-Doped Fiber Amplifier
FPGA	Field-Programmable Gate Array
FWHM	Full Width at Half-Max
GA	Genetic Algorithm
H	Horizontal (polarization)
HOM	Hong-Ou-Mandel (interferometry)
LAP	Light-Assisted Poling
LCD	Liquid Crystal Display
LLAP	Latent Light-Assisted Poling
LN	Lithium Niobate
NiCr	Nickel chromium
NSD	Nucleation Site Density
O	Ordinary (polarization)
OR	Optical Rectification
PC	Personal Computer
PE	Proton Exchange
PE:LN	Proton Exchanged Lithium Niobate (waveguide)
PMD	Polarization Mode Dispersion
PPLN	Periodically Poled Lithium Niobate
QFC	Quantum Frequency Conversion
QOCT	Quantum Optical Coherence Tomography
QPM	Quasi Phase Matching
RAM	Random-Access Memory
SFG	Sum Frequency Generation
SH	Second Harmonic (generation)
SIMS	Secondary-Ion Mass Spectroscopy

continued on next page

continued from previous page

SLM	.....	Spatial Light Modulator
SPDC	.....	Spontaneous Parametric Down Conversion
TE	.....	Transverse Electric (mode)
Ti:LN	.....	Titanium diffused LN (waveguide)
Ti:PPLN	.....	Titanium diffused waveguide in PPLN
TM	.....	Transverse Magnetic (mode)
V	.....	Vertical (polarization)
WDM	.....	Wavelength De-Multiplexer

Chapter 1

Introduction

1.1 Motivation

This work presents new fabrication techniques, designs, and implementations of waveguide-based quantum devices in the nonlinear material lithium niobate. The advancements presented in this dissertation are a step towards bringing quantum devices out of the laboratory and into computers, networks, and sensors.

1.2 The importance of quantum frequency conversion

Quantum frequency conversion (QFC) is an enabling technology for integrating quantum memories in quantum networks. Quantum memories are defined as a system that can store units of quantum information — *i.e.*, qubits — and are necessary for quantum computation in the same way that classical memories (random access memory (RAM), flash memory, *etc*) are necessary for conventional computation (Brennen 2015). Optical photons are the preferred quantum information carriers for much the same reasons that they dominate modern classical communications – photons move fast and their internal state (energy, momentum) typically does not interact much with the environment, so they can transmit information quickly and with high fidelity over long distances. Most classical memories, however, are written and read electronically, not optically. Integrating classical memories in optical networks thus requires electrical-to-optical transmission *via* light emitting diodes or lasers, and optical-to-

electrical reception *via* photodiodes. Quantum memories, by comparison, are made of superpositions between energy levels in atomic or solid state systems. They are typically read and written optically, but not necessarily at useful wavelengths for integration into a telecommunications network (*i.e.*, the telecommunications C-band from 1530nm to 1565nm). Quantum memories have been demonstrated in systems ranging from atomic vapor cells (Novikova et al., 2012) to Bose-Einstein condensates (Riedl et al., 2012), trapped ions (Kielpinski et al., 2001), and solid state systems (Morton et al., 2008), each of which operates at an optical wavelength dictated by the storage media. Integration of these systems into a network requires low-loss conversion of individual photons from one wavelength to another, without altering the photons' quantum mechanical state (Kumar, 1990). One result of this dissertation is the demonstration of a quantum frequency converter designed to integrate metastable xenon quantum memories operating at 853nm into a telecommunications network operating in the C-band (Thomas et al., 2015).

1.3 Customizable spectral and polarization entanglement for high-resolution optical measurements

Quantum interferometry is a valuable tool in multiple quantum information applications such as Bells inequality violation, quantum communication, and quantum teleportation. The use of *broadband* polarization-entangled photons enables high-resolution quantum imaging (Mohan et al., 2009), quantum optical coherence tomography (QOCT) (Abouraddy et al., 2002), and measurement of polarization mode dispersion (Fraine et al., 2012)(Fraine, 2015), and helps in boosting the performance of other types of optical sensors. In order to produce a desired quantum state entangled simultaneously in polarization and frequency, pairs of photons are generated via Type-II spontaneous parametric down conversion (SPDC) in quasi-phase matched

periodically poled lithium niobate. The region of nonlinear interaction is spatially constrained by a titanium-diffused waveguide (Ti:LN). The down conversion spectrum is intentionally broadened by engineered chirping of the quasi-phase matching period. The chirp periodicity is apodized closer to edges of interaction region in order to smooth spectral modulations and produce a smooth Gaussian-shaped spectral envelope. This apodization helps to minimize the width and increase the visibility of the intensity correlation interferogram, and thus optimizes its performance capabilities as an interferometric sensor. The presence of frequency entanglement enables use of the quantum effect of even-order dispersion cancellation and avoids the detrimental effects of dispersive envelope broadening. Together, these advantages improve the resolution and sensitivity of quantum interferometric sensors in comparison with its conventional optical counterparts (Fraine, 2015).

1.4 Summary of the present state of the art

Lithium niobate is heralded as "the silicon of photonics", due in part to its large nonlinear optical coefficient and broad transparency window from 350nm to over 5μm (Manzo et al., 2013). While nonlinear optical devices in lithium niobate waveguides are a robust area of research, far fewer authors have extended these technologies to quantum devices capable of supporting polarization entanglement. Fewer still have attempted to control the effective nonlinear coefficient to the level demonstrated in this dissertation. This work reports the first combination of the versatile but technically challenging titanium-diffused lithium niobate waveguide technology with *engineered aperiodic quasi-phase-matching*, a method for imposing fine spatial control of the effective nonlinear coefficient and sculpting it along the length of the waveguide.

The two core technologies used in this work are titanium-diffused lithium niobate (Ti:LN) waveguides and quasi-phase matching. Ti:LN waveguides were first

demonstrated at Bell Laboratories in 1974 (Schmidt and Kaminow, 1974), but were overtaken in popularity by proton exchange waveguides (PE:LN), first demonstrated in 1982 (Jackel et al., 1982). Proton exchange waveguides are markedly easier to fabricate, with peak processing temperatures below 300C. Ti:LN waveguide fabrication typically requires sustained temperatures in excess of 1000C for approximately 8 hours. This high-temperature processing causes unwanted diffusion of lithium oxide out of the crystal lattice, which complicates subsequent fabrication steps and reduces yield. Ti:LN waveguides, however, can support both TE-like and TM-like modes, while proton exchange waveguides can only support TM-like modes. As of the date of this publication, Ti:LN is the only LN waveguide technology that has been used for direct generation of orthogonally-polarized frequency-entangled photon pairs. While parallel-polarized photon pairs *can* be manipulated into orthogonal polarizations and even polarization entanglement, they require the complication of either multiple sources or an external polarization Sagnac interferometer, both of which would require active optical phase stabilization for the interferometric applications described in this work (Arahira et al., 2012).

Quasi-phase matching (QPM) is a technique for manipulating the effective nonlinear index of lithium niobate and other ferroelectric nonlinear optical materials. In brief, QPM works by locally inverting the direction of the material's polarization vector, creating a linear pattern of alternating "up" and "down" domains along the length of the waveguide (details in Chapter 2). This inversion typically takes the form of a square wave with fixed period and duty cycle, and serves to manage the relative phase of the multiple wavelengths involved in the nonlinear interaction *without altering the linear refractive index*. QPM facilitates higher overall conversion efficiencies by enabling the pump, signal, and idler wavelengths to stay approximately in phase as they propagate. Adjusting the period of a uniform QPM grating can shift

the peak efficiency of the target nonlinear interaction to anywhere in the material's transparency window, provided energy and momentum are conserved. This tuning effect is the most common application of QPM, and the technology for fabricating constant QPM gratings is well-developed in bulk LN (Myers et al., 1995), PE:LN (Yamada et al., 1993), and Ti:LN (Amin et al., 1997), although Ti:LN is less common due to the fabrication challenges described above. The high conversion efficiency necessary for QFC is enabled by QPM in waveguides, and this works' demonstration of QFC to 843nm with 1550nm and 1848nm input fields in Ti:LN is the first at that wavelength combination.

QPM is not limited to uniform gratings, and spatial variations of the period and/or duty cycle can be used to further tailor the phase-matching bandwidth. Broadly speaking, these "engineered" aperiodic QPM gratings fall into 3 categories: cascaded, interlaced, and chirped/apodized. Cascaded gratings are comprised of two or more regions of uniform poling, one after another. Applications include multi-stage processes, such as converting the wavelength of the pump laser and then using the new wavelength to seed a second nonlinear process (Lee et al., 2003). Interlaced QPM devices perform two or more nonlinear processes simultaneously over the entire length of the device by alternating between the constituent QPM periods, and applications include post-selection-free generation of non-degenerate polarization and frequency hyperentangled photon pairs (Thomas, 2010). The previous reference is the only implementation of these methodologies in Ti:LN waveguides in the literature. With dual periods of 9.30μm and 9.37μm in a single waveguide, it represents the most complex aperiodic poling structure implemented in Ti:LN prior to this work.

The engineered QPM in this work is chirped and apodized, meaning the QPM period varies monotonically along the length of the waveguide to broaden and shape the phasematching spectrum. The design presented in Chapter 3 is optimized by a

genetic algorithm which compares the output — in this case, the two-photon polarization interferogram — with a target function, and iteratively modifies the poling structure until the target is met or the output ceases to improve. Engineering of the interferogram through simple linear chirps was demonstrated in bulk periodically poled potassium titanyl phosphate (KTP) in 2012, as well as a theoretical treatment of iteratively optimized apodized chirps for narrowing the two-photon polarization interferogram (Fraine, 2015). Linear and apodized chirps have also been implemented in bulk LN (Bortz et al., 1994) and PE:LN waveguides (Langrock et al., 2007), but without assessment of their performance in the quantum limit. This work is the first demonstration of 1) chirped and apodized QPM in Ti:LN waveguides, and 2) SPDC and two-photon quantum polarization interferometry with photons from an engineered, chirped and apodized aperiodic QPM waveguide source.

1.5 Structure of the dissertation

The structure of the dissertation is as follows:

- Chapter 2 presents the theoretical underpinnings of the dissertation, including both classical and quantum nonlinear frequency conversion in $\chi^{(2)}$ materials, an overview of two-photon quantum polarization interferometry, and a description of the genetic algorithm used to optimized the engineered QPM profile.

- Chapter 3 describes the fabrication technologies used to create engineered QPM Ti:LN waveguides, starting with conventional techniques from the literature and ending with the optimized technique developed for this work.

- Chapter 4 describes the Type-0 QFC sample design, experiments, and performance.

- Chapter 5 describes the Type-II engineered aperiodic QPM sample design, experiments, and performance. Classical and quantum results for unchirped, linearly chirped, and engineered apodized chirps are presented.

- Chapter 6 presents a roadmap for future technology development, including possible avenues for further narrowing the interferogram, improving fabrication, applying the broadband source described in Chapter 5 for ultra-high-resolution measurements of polarization mode dispersion, and developing engineered apodized QPM in waveguides into a turn-key technology platform.

- Chapter 7 is the summary and conclusion.

Chapter 2

Theory

2.1 Nonlinear frequency conversion in $\chi^{(2)}$ materials

Nonlinear materials can convert optical energy to different wavelengths, provided energy and momentum are conserved. Consider the general case of a dielectric without free charges or magnetization. The Maxwell equations (Ampere's Law, Faraday's Law, and Gauss's Laws for electric and magnetic fields) are given by

$$\begin{aligned} \nabla \times \vec{E} &= -\frac{\partial}{\partial t}\vec{B} \\ \nabla \times \vec{B} &= \frac{\partial}{\partial t}\vec{D} \\ \nabla \cdot \vec{D} &= 0 \\ \nabla \cdot \vec{B} &= 0, \end{aligned} \tag{2.1}$$

with the constituent relations

$$\begin{aligned} \vec{D} &= \epsilon_0 \vec{E} + \vec{P} \\ \vec{B} &= \mu_0 \vec{H} \end{aligned} \tag{2.2}$$

and where, following the convention of (Boyd, 2008), the nonlinear polarization is expressed as a power series in orders of electric field:

$$\vec{P} = \epsilon_0 \left(\chi^{(1)} \vec{E} + \chi^{(2)} \vec{E}^2 + \chi^{(3)} \vec{E}^3 ... \right) = \vec{P}^{(1)} + \vec{P}^{NL}. \tag{2.3}$$

Taking the curl of Ampere's Law and sequentially substituting in the remaining three Maxwell equations and constituent relations gives the wave equation

$$\nabla^2 \vec{E} - \frac{n^2}{c^2}\frac{\partial^2}{\partial t^2}\vec{E} = \frac{1}{\epsilon_0 c^2}\frac{\partial^2}{\partial t^2}\vec{P}^{NL}, \tag{2.4}$$

which is simply the familiar wave equation for the propagation of light in a vacuum with the addition of a driving term from the nonlinear material. Lithium niobate is a $\chi^{(2)}$ material, meaning the nonlinear response is dominated by the $\chi^{(2)}\vec{E}^2$ term and higher orders can be neglected.

2.1.1 Origin of nonlinearity in lithium niobate

Lithium niobate ($LiNbO_3$) belongs to a class of anisotropic materials called *negative uniaxial crystals*, meaning the linear component of the refractive index of one axis within the crystal lattice (the *extraordinary* axis) is less than the index of the other two (the *ordinary* axes). Lithium niobate is also a *perovskite*, a class of crystal structure with A and B cations in a sublattice of X anions and formulae of the form ABX_3. Although stoichometric lithium niobate wafers are commercially available, this work uses wafers with the more common "congruent" composition, which are about 1% lithium deficient. The lithium niobate lattice consists of alternating planes of oxygen containing lithium ions and cages of oxygen containing niobium ions, as shown in Fig. 2·1, and is ferroelectric below the Curie temperature $C_T = 1140$C (Smolenskii et al., 1966). The extraordinary axis is thus the z axis of the crystal with linear refractive index $n_e(\omega)$, and the x and y axes have linear refractive index $n_o(\omega) > n_e(\omega)$. The polarization of lithium niobate arises from the displacement of the positively charged lithium and niobium ions from the negatively-charged oxygen sublattice. This displacement of the ions causes an overall separation of the center of mass of the positive and negative charges, resulting in an effective cubic potential

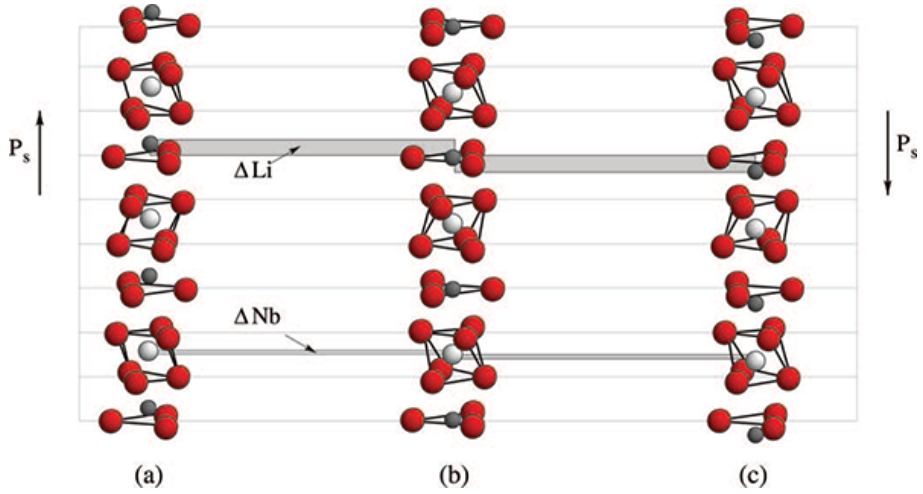

Figure 2·1: The atomic structure of lithium niobate in the ferroelectric (a, c) and paraelectric (b) phases. The shaded regions ΔLi and ΔNb show the displacement of lithium (gray) and niobium (white) ions from the oxygen (red) sublattice between the para- and ferroelectric phases. This displacement gives rise to the spontaneous polarization P_s, which can be either parallel (a) or antiparallel (c) to the crystal $\vec{c}$ (z) axis (Prezas and Graca, 2016).

(Boyd, 2008). This separation is shown schematically in Fig. 2·2.

2.1.2 Classical second-order nonlinear processes

Consider the case where a piece of lithium niobate is illuminated by two monochromatic lasers at frequencies ω_P and ω_S and amplitudes $|E_P| \geq |E_S|$ propagating along the crystal x axis. For historical reasons, the stronger of the two fields is called the *pump* and the weaker is called the *signal*. In the coordinate system of the crystal axes, the net incident electric field can be approximated as a plane wave

$$\vec{E}_{in} = \vec{E_P} e^{-i\left(\omega_P t - \vec{k}_P(\omega_P) x\right)} + \vec{E}_S e^{-i\left(\omega_S t - \vec{k}_S(\omega_S) x\right)} + c.c. \tag{2.5}$$

with wavevectors $\vec{k}_{P,S}(\omega) = k_o(\omega)\,\hat{y} + k_e(\omega)\,\hat{z}$ and $k_{o,e}(\omega) = \omega\sqrt{\epsilon_{o,e}(\omega)\,\mu(\omega)} = \frac{\omega n_{o,e}(\omega)}{c}$. If the phases are absorbed into $\vec{E}_{P,S}$, the nonlinear polarization ($\vec{P}^{NL} =$

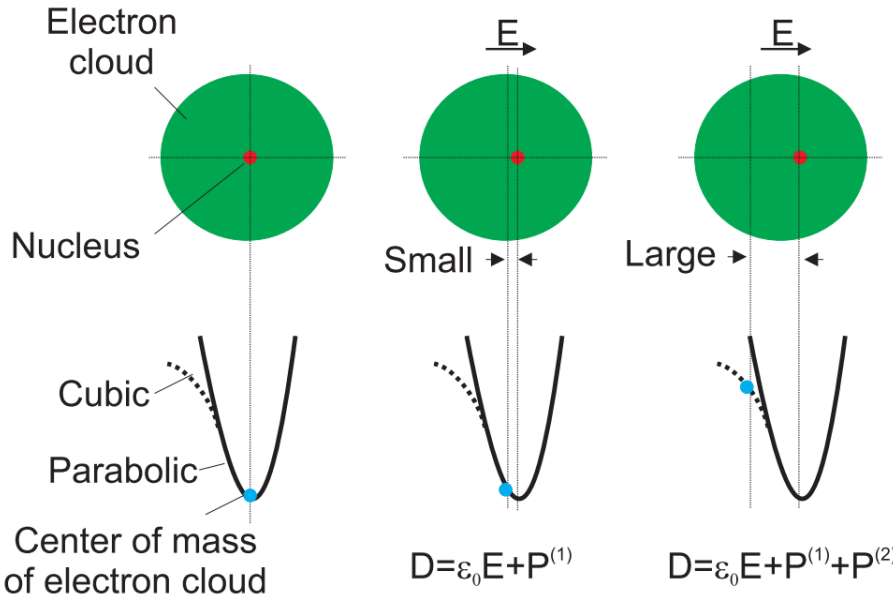

Figure 2·2: Illustration of the electron cloud displacement and resulting potentials for different strength nonlinearities. Figure from (Thomas, 2010).

$\epsilon_0\chi^{(2)}\vec{E}^2$ from Eq. 2.6) is then given by

$$\vec{P}^{NL} = \epsilon_0\chi^{(2)}\left[\vec{E}_P^2 e^{-i(2\omega_P)t} + \vec{E}_S^2 e^{-i(2\omega_S)t} + 2\vec{E}_P\cdot\vec{E}_S e^{-i(\omega_P+\omega_S)t} + 2\vec{E}_P\cdot\vec{E}_S^* e^{-i(\omega_P-\omega_S)t} + c.c\right] + 2\epsilon_0\chi^{(2)}\left[\vec{E}_P\cdot\vec{E}_P^* + \vec{E}_S\cdot\vec{E}_S^*\right] \quad (2.6)$$

and contains frequencies not present in the original pump and signal fields.

Consider the terms of in Eq. 2.6 one at a time. Again following historical convention, a field at a new frequency generated by the pump and signal is called the *idler*, with frequency ω_I. Four basic classical processes are possible, each representing a different way to achieve energy conservation between the three fields. The first and second terms in Eq. 2.6 represent second harmonic generation (SH), where $\omega_I = 2\omega_{P,S}$. Since SH only depends on a single input field, it is typically performed at a single input frequency (*i.e.*, only one input laser is used and $\omega_S = \omega_P$). The third and fourth terms are sum and difference frequency generation (SFG, DFG), where

$\omega_I = \omega_P \pm \omega_S$. Note that second harmonic generation can be considered a special case of SFG. The fifth and sixth terms of Eq. 2.6 are a quasi-DC process called optical rectification (OR), which causes an intensity-dependent change in the polarization. Nonlinear devices are typically designed and operated so that a single process (SH, SFG, DFG, or OR) dominates at a given $\omega_{P,S,I}$, and the other terms can be neglected.

The magnitude of each of the above nonlinear processes is governed by the nonlinear susceptibility tensor $\chi^{(2)}$. In theory, $\chi^{(2)}$ has 81 components corresponding to the 3^3 possible combinations of pump, signal, and idler polarization in the $(\hat{x}, \hat{y}, \hat{z})$ basis. In practice, geometrical and permutation symmetry constraints reduce the number of nonzero terms in lithium niobate to just 8 terms, many of which are degenerate. In the limit where the nonlinear susceptibility is independent of frequency (*i.e.*, when the system fulfills the Kleinman symmetry condition (Boyd, 2008)), the nonlinear susceptibility tensor of congruent lithium niobate reduces to

$$\begin{aligned} d = \frac{1}{2}\chi^{(2)} &= \begin{bmatrix} 0 & 0 & 0 & 0 & d_{31} & -d_{22} \\ -d_{22} & d_{22} & 0 & d_{31} & 0 & 0 \\ d_{31} & d_{31} & d_{33} & 0 & 0 & 0 \end{bmatrix} \\ &= 1\text{pm/V} \begin{bmatrix} 0 & 0 & 0 & 0 & 4.5 & -2.4 \\ -2.4 & 2.4 & 0 & 4.5 & 0 & 0 \\ 4.5 & 4.5 & 31.5 & 0 & 0 & 0 \end{bmatrix} (Koetitz, 1990). \end{aligned} \tag{2.7}$$

In the case of collinear DFG with all beams propagating along the crystal x axis,

$$\begin{aligned} &\vec{P}_{NL} = 2\epsilon_0 d \vec{E}_{in}^2 (\omega_P, \omega_S) \\ &= 4\epsilon_0 \begin{bmatrix} 0 & 0 & 0 & 0 & d_{31} & -d_{22} \\ -d_{22} & d_{22} & 0 & d_{31} & 0 & 0 \\ d_{31} & d_{31} & d_{33} & 0 & 0 & 0 \end{bmatrix} \begin{bmatrix} 0 \\ E_y(\omega_P) E_y(\omega_S) \\ E_z(\omega_P) E_z(\omega_S) \\ E_y(\omega_P) E_z(\omega_S) - E_z(\omega_P) E_y(\omega_S) \\ 0 \\ 0 \end{bmatrix}. \end{aligned} \tag{2.8}$$

With the nonlinear susceptibility tensor, one can solve the wave equation Eq. 2.4. For brevity this section will highlight phase matching in the case of DFG with collinear pump, signal, and idler propagating along the crystal x axis, and will operate in the paraxial approximation. The analysis is identical for SFG up to the sign of the signal terms.

A plane wave pump and signal as in Eq. 2.5 can be re-written in the collinear approximation as

$$E_{in} = A_P e^{-i(\omega_P t - k_P x)} + A_S e^{-i(\omega_S t - k_S x)} + c.c. \tag{2.9}$$

where $A_{P,S}$ are the amplitudes of the signal and idler waves. The DFG idler, then, will have the form

$$E_I = A_I e^{-i(\omega_I t - k_I x)} + c.c., \tag{2.10}$$

with $\omega_I = \omega_P - \omega_S$. From Eq. 2.6 and Eq. 2.7, the nonlinear polarization is

$$P^{NL} = 4 d_{eff} E_P E_S e^{-i\omega_I t} = 4 d_{eff} A_P A_S e^{-i(\omega_I t - (k_P - k_S)x)}, \tag{2.11}$$

where d_{eff} is the effective nonlinear polarization for the chosen pump, signal, and idler polarizations.

Substituting the above into the full wave equation Eq. 2.4, simplifying, and applying the slowly varying amplitude approximation $\left(\left| \frac{d^2 A_I}{dx^2} \right| << \left| \frac{dA_I}{dx} \right| \right)$ yields

$$\frac{dA_I}{dx} = \frac{2 i d_{eff} \omega_I^2}{k_I c^2} A_P A_S e^{-i\Delta k x} \tag{2.12}$$

where $\Delta k = k_P - k_S - k_I$ is called the wave vector mismatch. The idler amplitude after length L of material is then given by

$$A_I(L) = \frac{2 i d_{eff} \omega_I^2 A_P A_S}{k_I c^2} \int_0^L e^{-i\Delta k x} dx. \tag{2.13}$$

Note that this eqution is valid even when Δk is a function of position, which will be relevant in the later discussion of engineered quasi-phase matching.

2.1.3 Phase matching

In addition to the energy conservation constraints discussed above, efficient frequency conversion requires *phase matching*. In brief, phase matching dictates that efficient transfer of energy to the idler field only occurs when the idler generated at each point along the length of the nonlinear material is in phase with the previously generated idler. For brevity this section will highlight phase matching in the case of DFG with collinear pump, signal, and idler. The analysis is identical for SFG up to the sign of the signal terms.

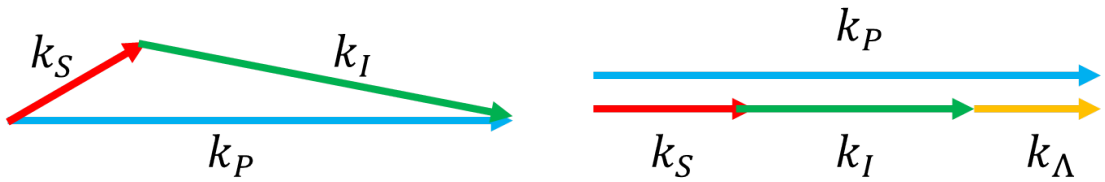

(a) (b)

Figure 2·3: Birefringent (a) and quasi- (b) phase matching for DFG.

In the plane wave approximation, the DFG pump, signal, and idler fields have phases $\phi_j = \vec{k}_j(\omega_j)\, x$ for $j = P, S, I$. In bulk nonlinear materials with uniform polarization and collinear propagation of all three beams, phase matching occurs when

$$\Delta k_{DFG} \equiv k_P - k_S - k_I = \frac{1}{c}\left(\omega_P n_P - \omega_S n_S - \omega_I n_I\right) = 0 \tag{2.14}$$

If $\Delta k_{DFG} \neq 0$, chromatic and polarization dispersion causes the waves to oscillate in and out of phase as they propagate, resulting in a net conversion efficiency that

periodically returns to zero. The spatial wavelength Λ_0 of the oscillation is

$$\Lambda_0 = 2 * L_c = \frac{2\pi}{k_P - k_S - k_I}, \tag{2.15}$$

where L_c is the coherence length.

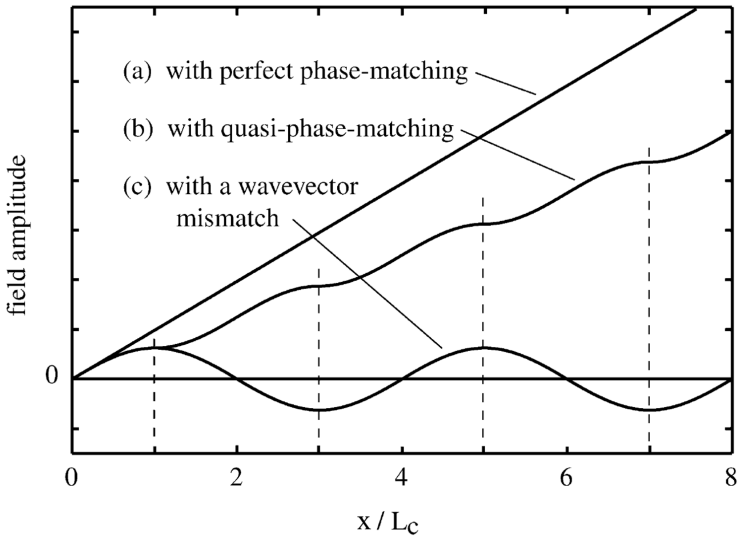

Figure 2·4: Intensity of the ider as a function of crystal length for perfectly phase matched (a), quasi-phase matched (b), and poorly phase matched (c) x-propagating collinear DFG in the absence of walk-off. Figure from (Boyd, 2008).

It is useful to classify phase matching configurations by the polarizations of the pump, signal, and idler. By historical convention, the configuration with the signal and idler both orthogonal to the pump is called Type-I phase matching, and the configuration with mutually orthogonal signal and idler is called Type-II. A third process with all fields parallel (Type-0) is also possible, but only in systems with quasi-phase matching (QPM), which is discussed in the next subsection.

Early experiments in nonlinear frequency conversion used thin pieces of birefringent crystals as the nonlinear medium (Klyshko et al., 1970). Phase matching was achieved by tilting the crystal with respect to the pump beam, creating an effec-

Table 2.1: Possible phase matching configurations for lithium niobate. The d_{eff} values are for congruent LN.

Type	Polarization P/S/I	d_{eff} [pm/V]
Type-0	ooo	$d_{22} = 2.4$
	eee	$d_{33} = 31.5$
Type-I	eoo	$d_{31} = 4.5$
Type-II	oeo	$d_{31} = 4.5$
	ooe	$d_{31} = 4.5$

tive ordinary index $n_{o_{eff}}(\theta)$. Fine-tuning of the phase matching is typically done by adjusting the crystal temperature, as most nonlinear materials have temperature-dependent indicies of refraction. This combination of angle and temperature tuning is known as *birefringent phase matching*, as it achieves phase matching using only the birefringent properties of the bulk material.

Birefringent phase matching is relatively straightforward to achieve, but fundamentally limits flexibility and conversion efficiency of the source. Temperature tuning can only compensate relatively small wave vector mismatches, which limits the possible frequency combinations. Angle tuning causes walk-off between the beams, limiting the effective interaction length and thus the peak conversion efficiency.

Quasi-phase matching improves flexibility and efficiency by allowing a much broader range of frequency and polarization combinations to interact along an arbitrarily long sample. Inverting the polarization every L_c flips the sign of the nonlinear coefficient while leaving the linear index unchanged. This inverts the phase of the generated idler, resulting in a monotonic growth in the conversion efficiency as the fields propagate through the material. Furthermore, any pump/signal/idler wavelength and polarization combination supported by the material can be achieved without tuning the crystal angle. This has the dual benefits of eliminating walk-off, and of allowing multiple processes to be phase matched within a single crystal. The periodic inversion of the polarization is called *periodic poling*, and in the simplest case of a uniform

grating it adds an additional lattice term to the phase matching condition:

$$\Delta k = k_P - k_S - k_I - \frac{2\pi}{\Lambda} = 0. \tag{2.16}$$

2.2 Quantum processes in $\chi^{(2)}$ materials

2.2.1 Quantization of the electromagnetic field

To construct a quantum mechanical treatment of the above nonlinear states, it is convenient to work in the second quantization. While the first quantization of the electromagnetic field expresses many-body states in terms of energy and momentum of each individual photon, the second quantization exploits the indistinguishability of particles in the same state and expresses the many-body state in terms of the number of photons in each mode of the field (*i.e.*, the second quantization is in the Fock basis of number states).

The canonical operators for mode j in the Fock basis are the annihilation and creation operators $\hat{a}_j$ and $\hat{a^\dagger}_j$, which lower and raise the number n of photons in state $|n\rangle_j$ by 1, respectively:

$$\hat{a}_j |n\rangle_j = \sqrt{n}\,|n-1\rangle_j \tag{2.17}$$

$$\hat{a}_j^\dagger |n\rangle_j = \sqrt{n+1}\,|n+1\rangle_j \tag{2.18}$$

$$\hat{N}_j |n\rangle_j \equiv \hat{a}_j^\dagger \hat{a}_j |n\rangle_j = n\,|n\rangle_j \tag{2.19}$$

$$\left[\hat{a}_i \hat{a}_j^\dagger\right] = \hat{a}_i \hat{a}_j^\dagger - \hat{a}_j^\dagger \hat{a}_i = \delta_{ij} \tag{2.20}$$

$$[\hat{a}_i \hat{a}_j] = \left[\hat{a}_i^\dagger \hat{a}_j^\dagger\right] = 0. \tag{2.21}$$

The following discussion assumes that the pump intensity remains constant throughout the length of the sample, and can be treated as a classical field with constant intensity. This is known as the non-depleting pump approximation. The pump, signal, and idler are also assumed to be collinear and paraxial.

2.2.2 Quantum frequency conversion

DFG and SFG become quantum in the limit where, on average, one signal photon is in the sample at a time (or, for a gated detection scheme, one signal photon is incident on the crystal per gate window). In this regime, a single photon can be converted from signal to idler with high efficiency while preserving the photons phase and entanglement (Kumar, 1990). This section considers QFC based on SFG; DFG differs only by the sign of ω_S.

The two-photon probability amplitude is given by the Fourier transform of the second-order nonlinear coefficient,

$$\tilde{\chi}^{(2)}\left(\omega_S, \omega_P + \omega_S\right) = \mathrm{sinc}\left(\Delta k L/2\right) e^{-i\Delta k L}. \tag{2.22}$$

where L is the length of the nonlinear material and $\Delta k = k_P + k_S - k_I - \frac{2\pi}{\Lambda}$. In the non-depleting pump approximation, the two-photon wavefunction can be written

$$|\Psi\rangle = \int d\omega\, \tilde{\chi}^{(2)}\left(\omega_S, \omega_P + \omega_S\right) \hat{a}_S\left(\omega_S\right) \hat{a}_I^{\dagger}\left(\omega_P + \omega_S\right) |10\rangle\,, \tag{2.23}$$

where $\hat{a}_S\left(\omega_S\right)$ and $\hat{a}_I^{\dagger}\left(\omega_P + \omega_S\right)$ are the annihilation and creation operators for the signal and idler, respectively, and $|10\rangle$ is the initial Fock state of one signal photon and zero idler photons (Boyd, 2008).

2.2.3 Spontaneous parametric down conversion

Spontaneous parametric down conversion is a method for producing entangled photons with a second-order nonlinear material. It is analogous to classical DFG, in the limit that the signal beam is removed and its role filled by vacuum fluctuations. As with QFC, the two-photon probability amplitude is given by the Fourier transform

of the second-order nonlinear coefficient,

$$\tilde{\chi}^{(2)}\left(\omega_S, \omega_P - \omega_S\right) = \mathrm{sinc}\left(\Delta k L/2\right) e^{-i\Delta k L}. \tag{2.24}$$

where L is the length of the nonlinear material and $\Delta k = k_P - k_S - k_I - \frac{2\pi}{\Lambda}$. In the non-depleting pump approximation, the two-photon wavefunction is

$$|\Psi\rangle = \int d\omega\, \tilde{\chi}^{(2)}\left(\omega_S, \omega_P - \omega_S\right) \hat{a}_S^{\dagger}\left(\omega_S\right) \hat{a}_I^{\dagger}\left(\omega_P - \omega_S\right) |00\rangle\,. \tag{2.25}$$

2.2.3.1 SPDC with engineered poling

The spectrum of down-converted photons can be engineered by altering the poling profile. Typically, phase matched interactions use the same poling period along the entire device. Since SPDC is a spontaneous process, the down-converted photons will populate the entire bandwidth defined by the phase matching conditions. One result of this work is making this quantum state more suitable for polarization sensitive interferometric sensing by broadening the phase matching spectrum while preserving the unique feature of frequency entanglement that is responsible for the quantum dispersion cancellation effect. This is achieved by chirping and apodizing the poling profile via the k-vector.

A non-uniform poling profile is modeled by representing each domain of the device as its own crystal. The engineered SPDC two-photon amplitude is given by

$$\tilde{\chi}^{(2)}\left(\omega_S, \omega_P - \omega_S\right) = \sum_n D\left(\vec{X}_n\right) \mathrm{sinc}\left(\Delta k \left| D\left(\vec{X}_n\right)\right| /2\right) e^{-i\Delta k\left(\frac{D\left(\vec{X}_n\right)}{2} + \phi\left(\vec{X}_n\right)\right)}, \tag{2.26}$$

where $\vec{X} \equiv \frac{2}{L}\vec{x} - 1$ is a normalized coordinate along the propagation direction with N elements, $D\left(\vec{X}_n\right)$ defines the poling profile, and $\phi_j\left(\vec{X}_n\right) = \sum_{j=n+1}^{N} \vec{X}_j$ is the phase accumulated by photons generated in each segment. In the specific case of a linear chirp, as shown in Fig. 2·5, the poling profile is $D\left(\vec{X}_n\right) = \frac{\Lambda_0}{2\left(1+c_1\vec{X}\right)}\left(-1\right)^n$, with

$\Lambda_0 = 2\pi/L_c$.

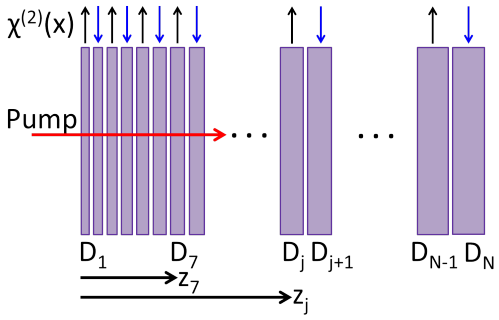

Figure 2·5: Illustration of poling with linear chirp. Figure modified from (Fraine, 2015).

2.3 Quantum two-photon polarization interferometry

As described above, at degeneracy Type-II SPDC generates pairs of orthogonally polarized frequency-entangled photons. These photon pairs can be used for polarization-sensitive quantum interferometry, which has numerous metrological and sensing applications (see Chapter 1). The interferometric techniques described here can be viewed as a polarization-based modification of Hong-Ou-Mandel (HOM) interferometry (Hong et al., 1987)(Dauler et al., 2000). The basic interferometer setup is shown in Fig. 2·6. The birefringent polarization delay changes the degree of overlap between two photons of orthogonal polarizations. The visibility of intensity correlation modulation (quantum interference) is directly proportional to the degree of indistinguishability between two photons arriving at the single-photon detectors. Two modes of operation are described. First is a description of the case where a variable birefringent delay is placed before the beamsplitter. This configuration is most closely related to traditional HOM interferometry, with the interferogram taking the form of a dip indicating the indistinguishability of the photons. Second is a description of the case where the variable birefringent delay and sample are placed after the beamsplitter.

In this configuration, the interferogram takes the form of rapid phase fringes with an envelope given by 2 times the HOM-like interferogram.

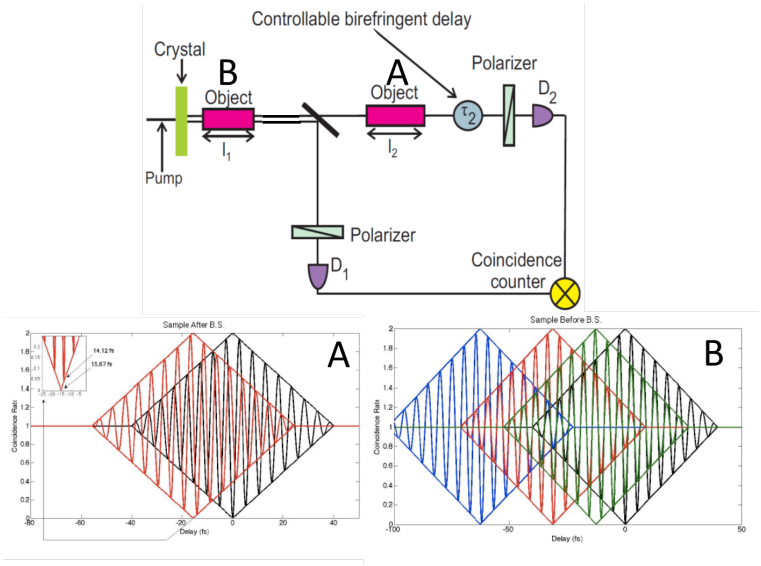

Figure 2·6: Illustration of the two-photon quantum polarization interferometer and expected interferograms for a sample after (A) and before (B) the beamsplitter (Fraine, 2015)

.

2.3.1 Configuration 1: birefringent delay before beamsplitter

In the time domain, the signal and idler photons are rectangular pulses with width equal to the coherence time $\tau_c = L\left(\frac{1}{v_o} - \frac{1}{v_e}\right)$, where $v_i \equiv \frac{\partial\omega}{\partial k_i} = \frac{c}{n_i + \omega\frac{\partial n_i}{\partial\omega}}$ is the group velocity of polarization i. The difference in group velocities also causes signal and idler photons to emerge from the crystal at different times, with the horizontally polarized photon leading the vertically polarized photon. At degeneracy and in the monochromatic idler limit, immediately after the crystal the state of the signal and idler photons is $|\Psi\rangle = \left|H\left(-t - \frac{\tau_c}{2}\right)V\left(t + \frac{\tau_c}{2}\right)\right\rangle$; a representation of this state is shown in Fig. 2·7. The birefringent delay before the beamsplitter slows down the horizontal photon with respect to the vertical, so the two wavepackets can be moved across each

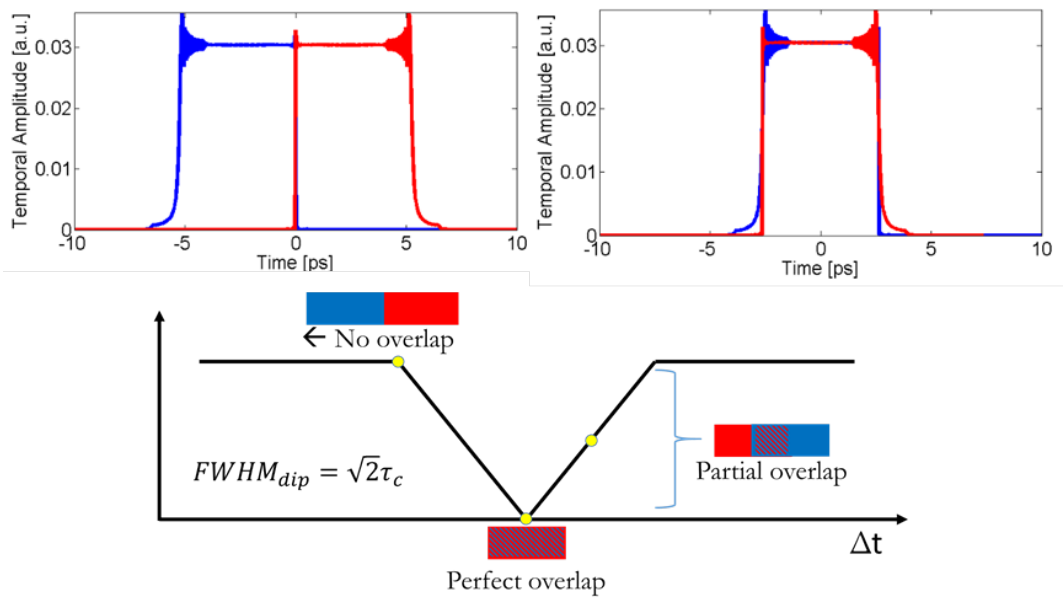

Figure 2·7: Illustration of the simplest case of Hong-Ou-Mandel-like two-photon polarization interferometry (monochromatic, degenerte signal and idler), with the birefringent delay line after the beamsplitter.

other in time (Fig. 2·7), making the wavefunction

$$|\Psi\rangle = |H(\tau_D - t)\, V(t - \tau_D)\rangle\,, \tag{2.27}$$

where $\tau_D = t_d - \frac{\tau_c}{2}$ and $t_d = \Delta n_D(\omega)\, L_D/c$ is the delay introduced by a birefringent delay line with index difference Δn_D and length L_D. After the non-polarizing beamsplitter, the state is

$$\begin{aligned}|\Psi\rangle = {} & |H(\tau_D - t)\, V(t - \tau_D)\rangle_A + |H(\tau_D - t)\, V(t - \tau_D)\rangle_B \\ & + |H(\tau_D - t)\rangle_A\, |V(t - \tau_D)\rangle_B + |V(t - \tau_D)\rangle_A\, |H(\tau_D - t)\rangle_B\,.\end{aligned} \tag{2.28}$$

Since the detection configuration only registers coincidences, post-selection reduces the state to

$$|\Psi\rangle = |H(\tau_D - t)\rangle_A\, |V(t - \tau_D)\rangle_B + |V(t - \tau_D)\rangle_A\, |H(\tau_D - t)\rangle_B\,. \tag{2.29}$$

Polarizers set at +45 (A) and -45 (B) degrees project this state into the diagonal/anti-diagonal basis, resulting in

$$|\Psi\rangle = |D(\tau_D - t)\rangle_A |D(t - \tau_D)\rangle_B - |A(t - \tau_D)\rangle_A |A(\tau_D - t)\rangle_B . \tag{2.30}$$

When $\tau_D = 0$ $\left(t_d = \frac{\tau_C}{2}\right)$ the terms cancel.

2.3.2 Configuration 2: birefringent delay after beamsplitter

2.3.2.1 Setup and theory

If the birefringent delay is placed after the beamsplitter it applies a differential phase to each polarization. The state after the delay line is given by

$$|\Psi\rangle = |H(\tau_D - t)\rangle_A |V(t - \tau_D)\rangle_B e^{in_{Do}(\omega_S)L_D\omega_S/c} - |V(t - \tau_D)\rangle_A |H(\tau_D - t)\rangle_B e^{in_{De}(\omega_I)L_D\omega_I/c}, \tag{2.31}$$

where $n_{Do,De}$ are the ordinary and extraordinary indices of the delay line. After projection into the diagonal/anti-diagonal basis, the state is

$$|\Psi\rangle = (|D(\tau_D - t)\rangle_A |D(t - \tau_D)\rangle_B - |A(t - \tau_D)\rangle_A |A(\tau_D - t)\rangle_B) \left(e^{in_{Do}(\omega_S)L_D\omega_S/c} - e^{in_{De}(\omega_I)L_D\omega_I/c}\right). \tag{2.32}$$

The measured amplitude $\langle\Psi|\Psi\rangle$ thus has a sinusoidal term dependent on the birefringence of the delay line, and the interferogram will have an envelope defined by 2 times the HOM-like interferogram, filled with fast phase-dependent fringes.

2.3.2.2 Even-order dispersion cancellation

Even-order dispersion cancellation is a uniquely quantum phenomena that enables a quantum polarization interferometer to have higher resolution than its classical analog. Even-order dispersion cancellation arises from the frequency anti-correlation

of the SPDC the signal and idler. For a given pump frequency, energy conservation requires that $\omega_P = \omega_S + \omega_I$. This can be re-written

$$\omega_P = (\omega_P/2 + \Omega) + (\omega_P/2 - \Omega)\,, \tag{2.33}$$

where $\omega_S = \omega_P/2 + \Omega$ and $\omega_I = \omega_P/2 - \Omega$. In other words, frequency anti-correlation means that if the frequency of the signal increases by Ω, the frequency of the idler must decrease by the same amount.

Frequency anti-correlation between the signal and idler is the origin of even-order dispersion cancellation. Terms of the form

$$\Delta k\,(\omega) = k_S - k_I = k\,(\omega) - k\,(-\omega)\,, \tag{2.34}$$

when Taylor-expanded into their even and odd components, can be re-written

$$\Delta k\,(\omega) = [k_{odd}\,(\omega) + k_{even}\,(\omega)] - = [k_{odd}\,(-\omega) + k_{even}\,(-\omega)] = 2k_{odd}\,(\omega)\,, \tag{2.35}$$

since by definition $k_{odd}\,(\omega) = -k_{odd}\,(-\omega)$ and $k_{even}\,(\omega) = k_{even}\,(-\omega)$. Similarly, the product $k\,(\omega)\,k\,(-\omega)$ is also odd. Thus the phase velocity dispersion between the signal and idler

$$\Delta v_p = \frac{\omega}{k\,(\omega)} - \frac{\omega}{k\,(-\omega)} = \omega \frac{-\Delta k\,(\omega)}{k\,(\omega)\,k\,(-\omega)} \tag{2.36}$$

only contains odd orders, as does the group velocity dispersion $\Delta v_g = \frac{d\omega}{dk(\omega)} - \frac{d\omega}{dk(-\omega)}$.

In addition to canceling the 2nd, 4th, and higher even orders of dispersion, frequency correlation also cancels the zeroth order of dispersion. Consider the case of the quantum polarization interferometer with the birefringent delay line after the beamspiltter. Classically, if a sample is placed before the beamsplitter the group velocity dispersion of the sample will shift (1st order dispersion) and broaden (2nd+ order) the interferogram envelope, and the phase velocity dispersion will shift the fringes (0th

order dispersion). In the quantum case, even-order dispersion cancellation protects the envelope from broadening due to 2nd (4th, etc) order dispersion, so the dominant effect the sample will have on the envelope is just a shift due to 1st order dispersion. Zeroth-order dispersion cancellation means that the phase fringes will not shift when a sample is introduced.

The phase fringes can thus be used as a static reference for measuring the shift in the envelope due to 1st order group velocity dispersion (Fraine et al., 2012)(Dauler et al., 2000)(Fraine, 2015)(Sergienko et al., 1996). This *quantum vernier effect* allows the 1st order group velocity dispersion to be measured to higher precision than classically possible. In the limit where the interferogram envelope is the width of a single phase fringe, the group velocity dispersion can theoretically be measured to within 2 attoseconds, the same precision as the phase velocity (Dauler et al., 2000). The narrower the envelope, the closer the resolution approaches this limit. The interferogram envelope is defined by Fourier transform of the signal/idler spectrum, so the envelope narrows as the SPDC bandwidth increases.

2.3.2.3 Optimization with genetic algorithms

To best exploit the quantum vernier effect, the interferogram envelope must 1) be as narrow as possible, 2) be free of side-lobes, and 3) have the highest visibility possible, ideally 100%. Linear chirping of the local QPM structure has been successfully implemented to broaden the phase matching bandwidth of conventional parametric amplifiers and converters, as well as in quantum Hong-Ou-Mandel interference experiments based on Type-I down conversion (Fraine, 2015). One known problem is that linear chirping of periodic structure in nonlinear crystals inevitably deforms the initial $\mathrm{sinc}\,(\omega)$ spectral phase matching profile (Kuo et al., 2013)(Thomas et al., 2015) and reduces parametric amplification of Gaussian signals. A special process of chirping and apodization was introduced with the goal of smoothing the spectral intensity

profile in parametric amplifiers (Ballato and Gupta, 2006)(Jaeger et al., 1993) leading to a quasi-Gaussian spectral intensity envelope. The production of broadband and simultaneously high quality hyper-entangled (spectral and polarization entanglement) photon states for quantum interferometry is a more demanding task. In addition to the broad and smooth spectral intensity profile of the source, quantum interferometry relies on the purity of the generated spectral and polarization entanglement. It is known from the early days of quantum optics that the quality of quantum interference with Type-II down conversion depends on complete indistinguishability of contributions from orthogonally polarized photons produced in different parts of the nonlinear interaction region, and on the stable phase relationship between all conjugated signal and idler spectral components (Dauler et al., 2000)(Giovannetti et al., 2006)(Thomas, 2010). The "quantumness" of the source is reflected in the peak fringe visibility: anything less than 100% indicates reduced entanglement, and $\leq 50\%$ indicates a classical state.

This work developed two methodologies for optimization of the interferogram width, shape, and visibility by chirping and apodizing the local QPM wave-vector (Van Camp et al., 2016)(Thomas et al., 2016). Both techniques are based on the genetic algorithm (GA) optimization method because the problem of reaching the target function with an arbitrary poling profile is not well suited for optimization algorithms based on numerical differentiation. The target poling profile $D\left(\vec{X}_n\right)$ (see Eq. 2.26) is

$$D\left(\vec{X}_n\right) = \frac{\Lambda_c}{2}\left(1 + \sum_{j=0}^{N} \alpha_{2j+1}\left(\vec{X}_n - \beta_{2j+1}\right)^{2j+1}\right)^{-1}, \tag{2.37}$$

where α_{2j+1} and β_{2j+1} are the coefficients solved for by the genetic algorithm. The poling profile is built on odd-order polynomials as they are known to symmetrically broaden and smooth the spectrum (Fraine, 2015). As an example, a symmetric 1% linear chirp is given by $\alpha_1 = 0.01$ with all other coefficients set to zero. The GA is

initiated by setting a target interferogram envelope full width at half-max (FWHM) σ. The GA and iteratively optimizes the poling profile until the target function

$$G(\sigma) = \left(\frac{FWHM\left(\left|\tilde{\chi}^{(2)}\right|\right) - \sigma}{\sigma} \right)^2 + (1-V)^2 + (1-p)^2 \tag{2.38}$$

is minimized, where p is the number of lobes in the interferogram envelope, V is the peak fringe visibility, and $\tilde{\chi}^{(2)}$ is the two-photon amplitude given in Eq. 2.24.

This dissertation also includes development of the theory of asymmetric odd polynomial poling terms ($\beta_{2j+1} \neq 0$), and a second GA target function for better exploiting these terms to further optimize the interferogram. Discussion of this alternate optimization scheme is in Chapter 6. Due to the fabrication challenges described in Chapter 3, the experimental results presented in the following chapters used the simpler optimization methodology presented in Eqs. 2.37, 2.38.

Chapter 3

Fabrication technology development

3.1 Diffused titanium waveguides in lithium niobate

3.1.1 Titanium diffusion

Diffused titanium channel waveguides in LN (Ti:LN) were first reported in reference (Schmidt and Kaminow, 1974), and first combined with periodic poling in reference (Amin et al., 1997). The primary benefit of Ti:LN waveguides over the more common proton exchange (PE) waveguides is that Ti:LN guides both TE-like and TM-like modes (ordinary and extraordinary polarization), while PE waveguides only support TM-like modes.

The index change in Ti:LN is directly proportional to the titanium concentration. For an x-propagating titanium stripe of width w along the crystal y axis and thickness τ above the crystal z axis, the concentration profile $c(y,z)$ after diffusion for t seconds is given by Fick's Law (Fontaine et al., 1986):

$$c(y,z) = \frac{\rho N_A \tau}{M_{Ti} d_z \sqrt{\pi}} \left[\operatorname{erf}\left(\frac{\frac{w}{2}+y}{2\sqrt{D_y t}} \right) + \operatorname{erf}\left(\frac{\frac{w}{2}-y}{2\sqrt{D_y t}} \right) \right] e^{-z^2/2\sqrt{D_z t}} \tag{3.1}$$

where $\rho = 4.507 \frac{g}{cm^3}$ is the bulk density of titanium, $N_A = 6.02214179 \times 10^{23} mol^{-1}$ is Avogadro's number, $M_{Ti} = 47.867 \frac{g}{mol}$ is the molar mass of titanium, and D_y and D_z are the diffusion coefficients at the diffusion temperature. This work uses a diffusion temperature of 1060C, and the diffusion coefficients $D_y = 6.26 \frac{\mu m^2}{hr}$ and $D_z = 0.57 \frac{\mu m^2}{hr}$ from reference (Fukuma and Noda, 1980). The wavelength-dependent increase in

the refractive indices is

$$\Delta n_e(\lambda, c) = Ec\frac{0.839\lambda^2}{\lambda^2 - 64500} \tag{3.2}$$

$$\Delta n_o(\lambda, c) = (Fc)^{0.55}\frac{0.800\lambda^2}{\lambda^2 - 80660} \tag{3.3}$$

with wavelength λ in units of nanometers and fitting parameters $E = 1.2 \times 10^{-23} cm^3$ and $F = 1.3 \times 10^{-25} cm^3$ (Strake et al., 1988).

Waveguide fabrication begins with electron-beam deposition of a 100nm thick layer of titanium on the -z face of a z-cut piece of lithium niobate. The titanium stripes are defined by a standard photolithographic process with Shipley S1818 positive photoresist, and etched in a 20:1:1 H_2O:HCl:H_2O_2 bath (Williams et al., 2003). After removing the remaining photoresist, the samples are placed in a tube furnace and ramped up to 1060C over 1 hour in a wet argon atmosphere. Diffusion occurs for 7 hours at 1060C in a wet argon atmosphere, and then the temperature is ramped back down to room temperature over 1 hour in a wet oxygen atmosphere. The presence of water vapor helps reduce the diffusion of lithium oxide out of the sample (Nozawa et al., 1990). Argon reduces unwanted domain inversion on the +z face during diffusion (Nakamura et al., 1987), and the final ramp-down in oxygen helps to partially repair diffusion-induced defects in the oxygen sublattice near the surface of the sample (Nozawa et al., 1990). Simulated mode profiles are shown in Fig. 3·1.

3.2 Poling lithium niobate

3.2.1 Fundamentals of domain inversion

Inversion of the spontanious polarization $\vec{P}_s$ is achieved by applying a sufficiently large electric field across the crystal to shift the Li and Nb ions with respect to the oxygen sublattice, as shown in Fig. 2·1. The coercive field V_c for congruent LN is typically about 21.5kV/mm (Kim et al., 2002), but can vary somewhat for wafers from different

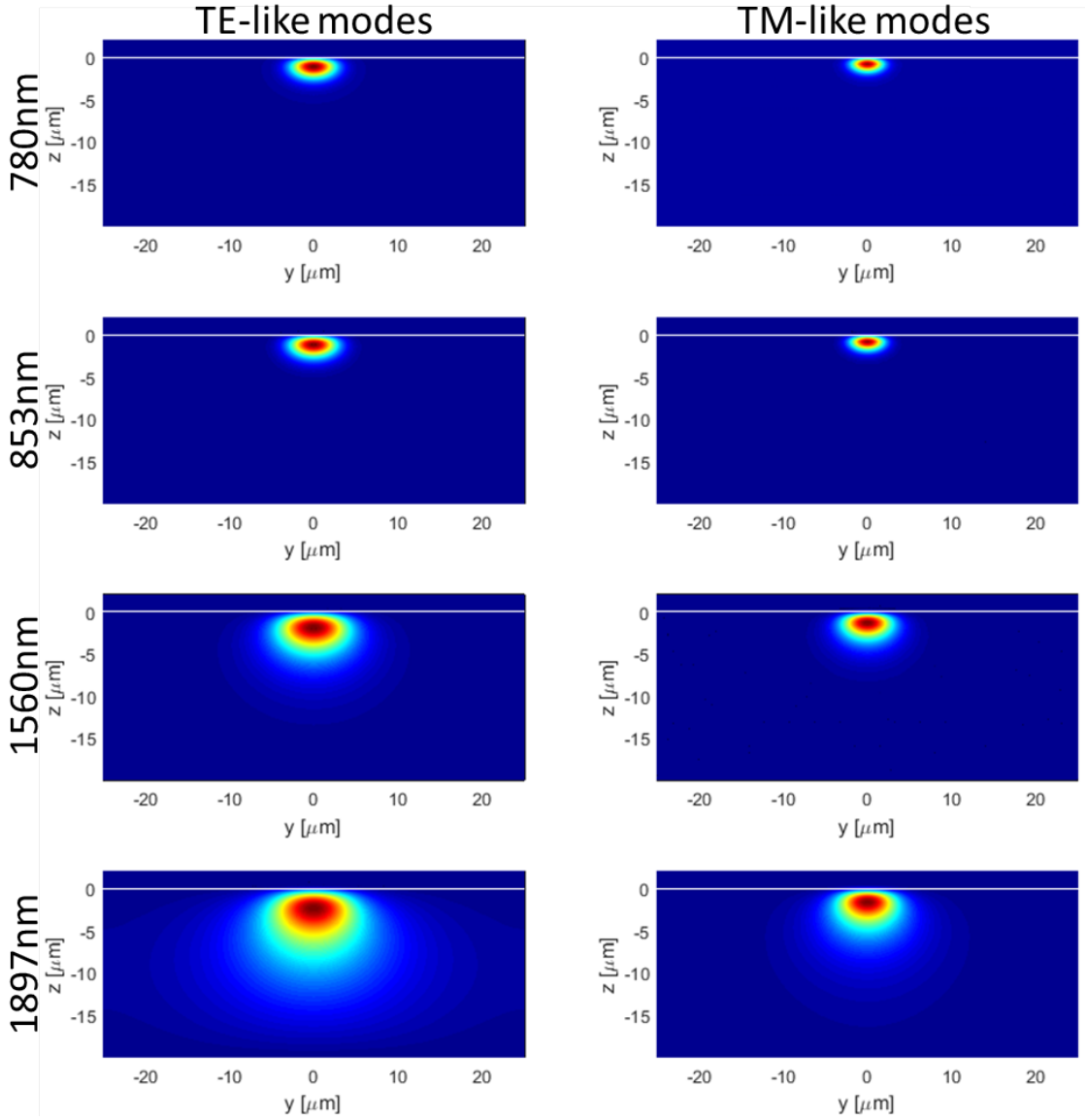

Figure 3·1: Simulated mode profiles for the Ti:LN waveguides fabricated in this work. The titanium stripe is 7μm wide and 100nm thick before diffusion, and is diffused for 7 hours at 1060C. White lines at $z = 0$ indicate the LN-air interface. TE-like modes have ordinary polarization, and TM-like modes have extraordinary polarization; in the following experiments, these correspond to H- and V-polarized modes.

vendors due to varying stoichiometry, contaminants, and accuracy of the wafer cut with respect to the crystal orientation (Abernethy, 2002). The DC breakdown field

of congruent LN is about 26kV/mm, but the crystal can survive brief excursions to higher fields (Miller, 1998).

3.2.2 Poling dynamics

The most common method of achieving domain inversion is *electric field poling*, where electrodes on the +z face define the area to be inverted, and a voltage $V > V_c$ is applied across the z axis. Some researchers have explored alternate methods for domain inversion, such as intense infrared irradiation (Chen et al., 2016) or direct-writing with an electron beam (Restoin et al., 2001), both of which are discussed further in Chapter 6. This work exclusively uses electric field poling.

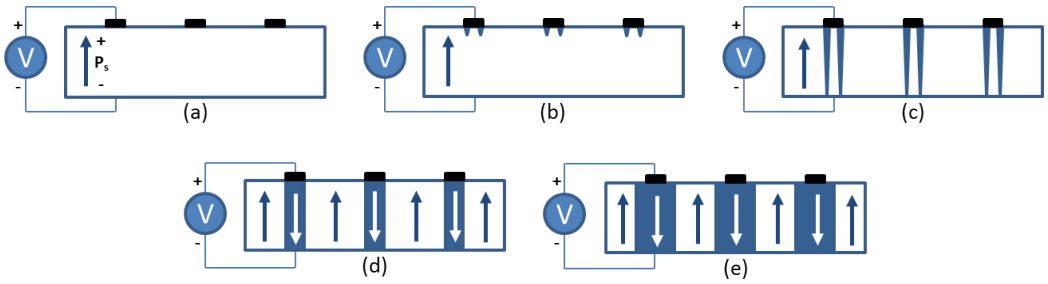

Figure 3·2: The stages of domain inversion. Poling is achieved by applying voltage $V \geq V_c$ across the sample via patterned electrodes on the +z face and uniform electrical contact to the -z face (a). Inverted domains nucleate at the edges of the electrodes where the z-component of the electric field is highest (b). The tips of the domains rapidly propagate to the -z face (c) and coalesce under the electrodes (d) before expanding outward at a slower rate (e).

Domain inversion from electric field poling can be broken down into four main stages: nucleation, tip propagation, domain coalescence, and wall propagation, which are summarized in Fig. 3·2 (Miller, 1998)(Kwon et al., 2006). In the nucleation phase, small regions of inverted polarization form on the surface of the crystal, typically on the +z face. The nucleation site density (NSD) depends on the z-component of the local field amplitude and is highest at the edge of the electrodes due to fringe field

effects (Miller, 1998). NSD also depends on the choice of electrode material, and this dependence was explored in depth in (Miller, 1998). The tips of the inverted domains rapidly propagate to the -z face of the crystal and coalesce into a solid region of domain inversion under the electrodes. Finally, the domain walls propagate away from the electrodes at a rate dependent on the applied field and electrode spacing.

3.2.3 Poling apparatus

The poling apparatus is shown in Fig. 3·3. The desired regions of domain inversion are lithographically defined on the +z face, as described in Sec. 3.2.4. The sample is then loaded into an acrylic poling chamber, held between two silicone rubber gaskets. The gaskets serve the dual purpose of distributing the mechanical stress on the sample, and of electrically isolating the ± z faces. The dimensions of the gasket opening define the maximum invertible area.

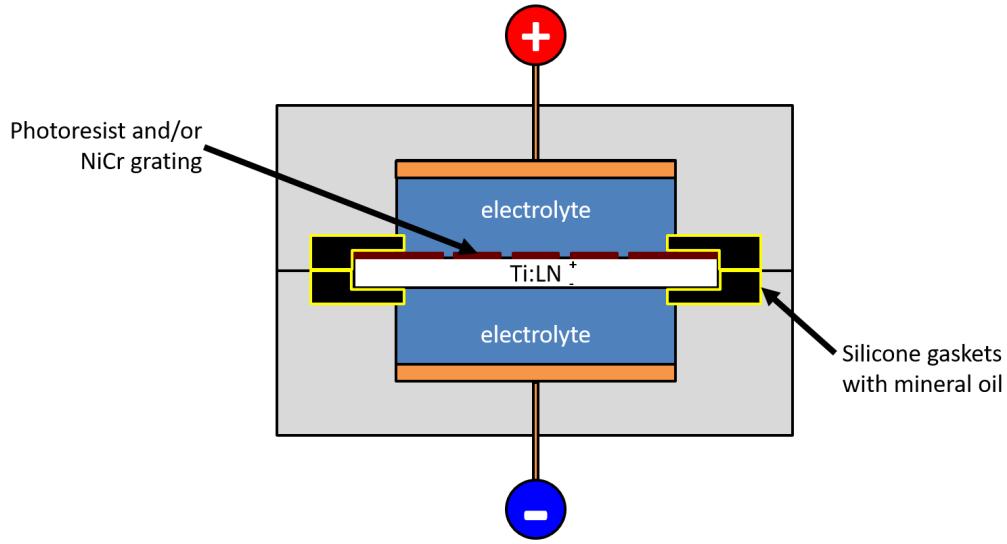

Figure 3·3: Schematic of the poling chamber.

After the sample is loaded, each half of the poling chamber is filled with a liquid

electrolyte solution. The electrolyte makes electrical contact between the sample and the brass electrodes embedded in the chamber wall. Many different electrolytes are used in the literature, with the most common being a saturated solution of lithium chloride salt in either DI water or isopropanol. Some papers report that a wide variety of electrolytes are equally well-suited for poling lithium niobate (Miller, 1998), and others report a preference for a water- or isopropanol-based solution depending on the poling parameters, due to their differing conductivities (Miller et al., 1996). This work never had success with a water-based electrolyte, with 100% of the attempts resulting in electrical breakdown of the sample. The lack of consensus regarding electrolyte choice presents an opportunity for future research into the optimal electrolyte for different poling voltage waveforms. This work exclusively uses a saturated solution of lithium chloride in isopropanol. This choice of electrolyte resulted in better survival of the samples.

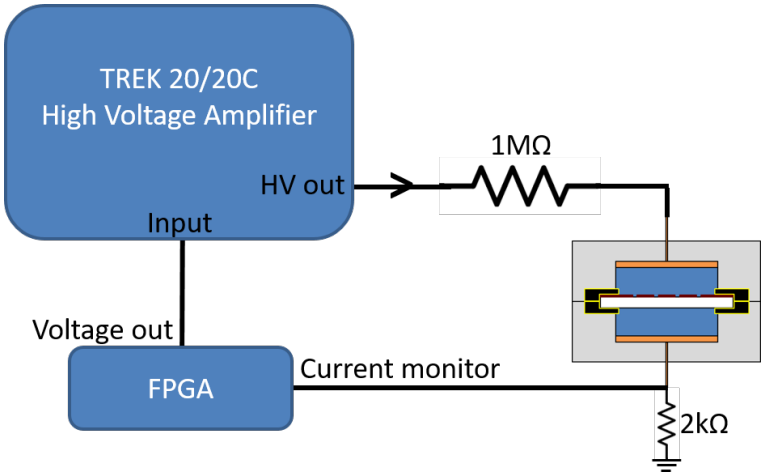

Figure 3·4: Diagram of the electric field poling apparatus. The target voltage is set by the FPGA and amplified by a TREK 20/20C high voltage amplifier. The high-voltage signal passes through a 1MΩ current-limiting resistor

The poling chamber is part of the larger poling circuit shown in Fig. 3·4. The desired waveform and feedback parameters are implemented with either a PC connected

to a data acquisition module (DAQ), or with a Zedboard/Xylinx field-programmable gate array (FPGA) development board which runs the poling independently of the PC. Using an FPGA allows for much faster feedback than possible with the PC alone, with response times on the order of 7us, compared to 1ms for the PC/DAQ (note that this is the time for the PC/DAQ to switch from *writing* to *reading* and back, which is the limiting time for enacting a feedback operation. The average cycle time is much lower). The FPGA or DAQ output is amplified on a TREK 20/20C high voltage amplifier, through a current-limiting 1MΩ resistor, and to the poling chamber. A series resistor after the chamber serves as a current monitor. A summary of the poling waveform and feedback system delveoped in this work is given in Section 3.2.2, with the full details of the entire optimized fabrication and poling procedure in Appendix A.

3.2.4 Poling procedure

3.2.4.1 Back-poling after titanium diffusion

The high temperatures required for titanium diffusion also lead to diffusion of lithium oxide out of the crystal. This lithium "out diffusion" combines with pyroelectric effects to generate a thin ($\approx 50\mu m$) layer of inverted domains on the +z face of LN (Hofmann et al., 1999), creating the situation shown in Fig. 3·5. Titanium diffusion into the +z face of LN can also cause domain inversion on its own, separate from out diffusion and pyroelectric effects (Miyazawa, 1979), so titanium waveguides destined for electric field poling must *always* be diffused on the -z face.

The inverted domain layer on the +z face frustrates future attempts at domain inversion, and must be mechanically removed prior to further processing. For this reason the waveguides are diffused into the -z face, which experiences far less spontaneous inversion during diffusion. The inverted layer is removed on a standard lapping and polishing mount, and then polarization of the crystal is inverted over the entire

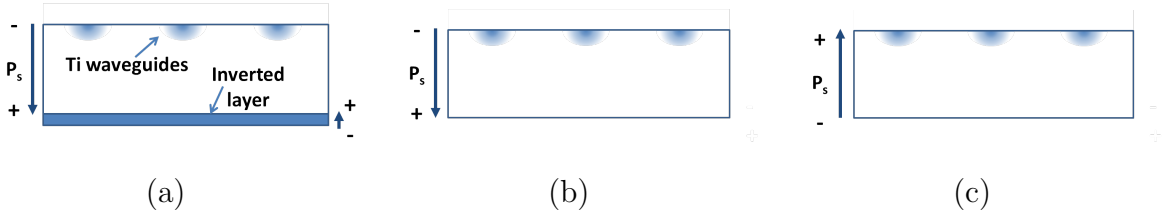

Figure 3·5: Illustration of inverted domain layer after high-temperature titanium diffusion (a), after removal of the inverted layer (b), and after backpoling (c).

area defined by the opening in the silicone gasket (*i.e.*, the maximum polable area). This results in the waveguides being on the +z face, which is ideal for the subsequent patterned poling step and also cleans up any domain noise in the bulk of the crystal.

3.2.4.2 Summary of electrode photolithography

The poling electrical contacts are defined photolithographically. For the QFC portion of this work, the electrical contacts were simply openings in an insulating layer of photoresist, where the electrolyte could contact the lithium niobate. This methodology produced poor results for the more complicated domain patterns necessary for engineered SPDC, and was replaced with nickel chromium (NiCr) electrodes under a layer of photoresist, with a single window in the resist for contact between the NiCr and the electrolyte. This section summarizes both techniques, and the fabrication details developed in this work are in Appendix A.

Electrical contacts defined by openings in photoresist are the simplest way to define regions of domain inversion. "Resist window" electrical contacts are commonly used in the literature for simple devices with large regions of homogeneous domain periodicity and duty cycle, and were used for the only other example of aperiodically poled Ti:LN in the literature (Thomas, 2010). The fabrication steps are summarized in Fig. 3·6. A layer of photoresist is spun on the +z face of the sample after back-poling, and electrolyte contact windows are defined by UV exposure through an

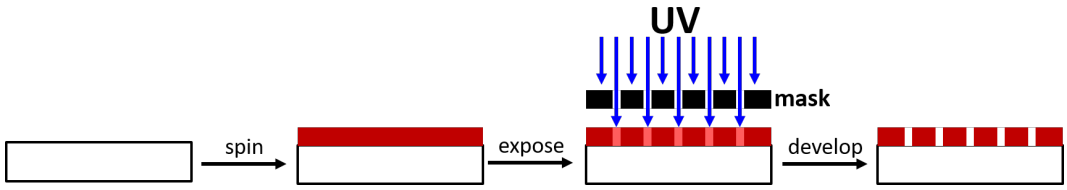

Figure 3·6: Summary of the procedure for fabricating "resist window" electrical contacts for periodic poling. From left to right, resist is spun on to the sample, exposed under UV illumination through a photomask, and developed. After developing, the sample is baked to improve dielectric strength and chemical resistance.

appropriate mask. After development, the sample is deliberately over-baked to improve the photoresist's dielectric strength and chemical resistance to the electrolyte solution (Nakamura et al., 2002).

Early research in periodic poling of lithium niobate found that metal electrodes can enhance the nucleation site density (NSD) compared to resist windows, with NiCr (80:20 Ni:Cr) electrodes providing the largest NSD enhancement compared to other metals (Miller, 1998). Increased NSD improves poling homogeneity across the sample, since more of the sample will be in the same phase of the domain inversion process at a given time. The effects of metal electrodes are discussed in further detail in Chapter 4.

Fabrication of NiCr electrodes under photoresist is summarized in Fig. 3·7. A layer of NiCr is deposited on the +z face of the sample via DC plasma sputtering. The electrodes are defined by the same photolithographic process used for the resist window electrodes, but with an opposite-tone mask. After development and post-baking, the NiCr electrodes are revealed by etching in MicroChem chromium etchant (Ceric ammonium nitrate : perchloric acid : H_2O = 10.9% : 4.25% : 84.85%). The remaining photoresist is stripped away, and a second photolithography cycle is performed to define an insulating photoresist layer, with one or more windows to

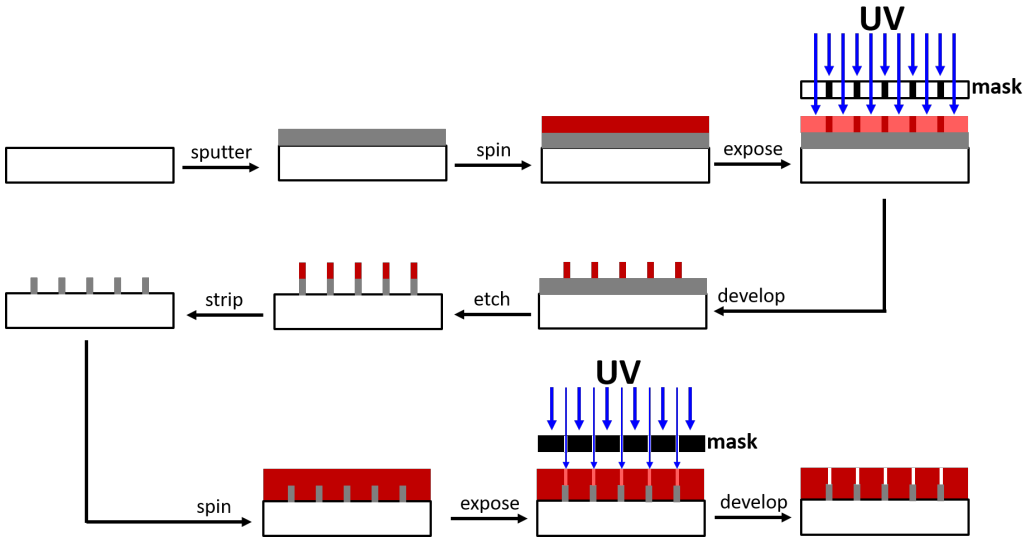

Figure 3·7: Summary of the procedure for fabricating nickel chromium electrodes under photoresist. Step-by-step fabrication instructions are given in Appendix A.

allow electrical contact between the NiCr and the liquid electrolyte.

3.2.4.3 Poling parameters

The form of the poling voltage pulse also affects the resulting poling quality, and the optimal parameters evolved over the course of this work. The initial QFC experiments performed in the course of this dissertation used samples with relatively large domains ($\approx 10\mu$m) and a constant target period and duty cycle along the length of each waveguide, and worked well with a simplified surface poling technique base on a 3-stage poling voltage waveform without grinding or back-poling. The majority of samples for SPDC and two-photon interferometry experiments were poled using a modified version of the same waveform, with the addition of grinding and back-poling. Chirped and apodized domains for broadband SPDC did not turn out well with this methodology, however, and the final optimized fabrication procedure required development of a methodology combining NiCr electrodes, faster feedback on the poling

voltage, and an 8-stage poling waveform for successful poling.

3.2.4.3.1 QFC samples The QFC samples reported in Chapter 4 were poled with the simple poling waveform shown in Fig. 3·8. Note that the high-voltage amplifier multiplies the DAQ output by a factor of 2000. The DAQ output voltage is slowly ramped up at 10mV/μs until current began to flow across the sample, signifying the onset of poling. The DAQ voltage then jumps to 5.55V (11.1kV across the sample), an empirically-found value that was high enough to produce a low-noise poling current and low enough to prevent electrical breakdown of the sample. The current is monitored and integrated to calculate the accumulated charge, and when the target charge is reached the voltage ramps down to zero. The slight negative dip at the end of the poling current is a sign of mild *backswitching*, a relaxation of part of the freshly-poled domains to their original polarity which occurs when the voltage is reduced too quickly (Batchko et al., 1999). In this instance, however, it proved small enough to be neglected.

This sample was also an attempt at "surface poling", a simplified poling technique where the sample is not ground or back-poled after titanium diffusion and the inverted domains are shallowly defined on the top surface only (Janner et al., 2008). Surface poling is reported to be a good technique for fabricating small domains on top of waveguides, but it did not perform well on these samples. Surface poling resulted in some areas of well-defined domain inversion and was sufficient to achieve the QFC result, but the surface poled samples suffered from macroscopically patchy poling as seem in Fig. 3·9. Changes to the poling waveform and electrode configuration did not resolve the issue. This patchiness resulted in an a reduction of the effective sample length and motivated adopting the more conventional methodology of grinding and back-poling prior to periodic poling.

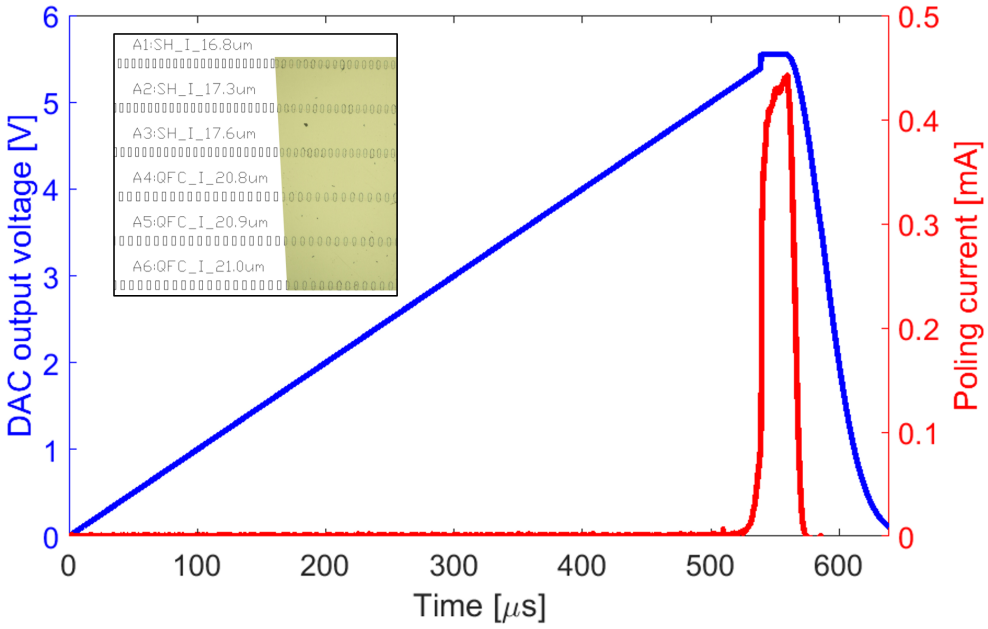

Figure 3·8: Poling waveform for QFC samples. Inset shows detail of the mask design and resulting domains.

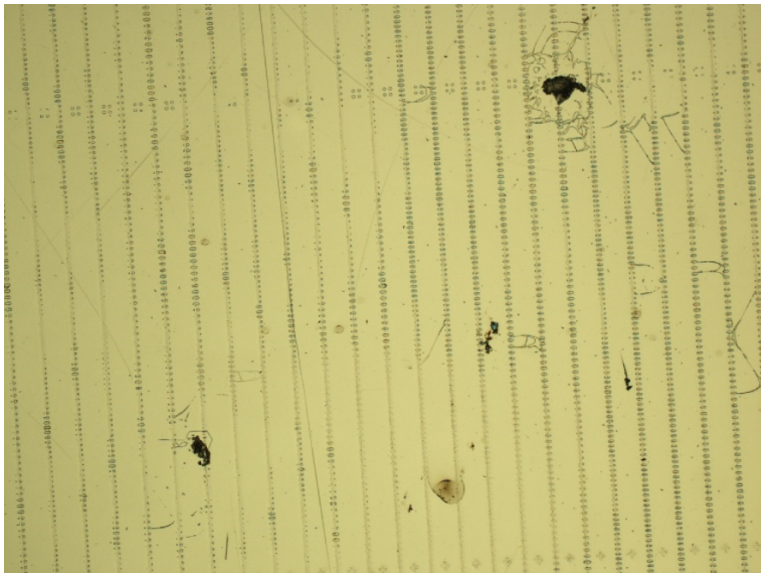

Figure 3·9: Zoomed-out image showing regions of patchy poling on the QFC sample shown in Fig. 3·8

3.2.4.3.2 First Type-II samples The majority of the Type-II SPDC and two-photon interferometry results reported in Chapter 5 are from samples fabricated by grinding and back-poling the sample after titanium diffusion, then performing periodic poling with resist windows. The poling waveforms for the most successful sample are shown in Fig. 3·10. The poling waveform has the same shape and switch conditions as in Fig. 3·8, with the initial ramp rate reduced to 2mV/μs. The slower ramp was empirically found to reduce breakage for ground and back-poled samples, which tend to be more fragile due to mechanical stress and thickness inhomogeneities. A representative image of the poling quality achieved with the back-poling and resist windows methodology is shown in Fig. 3·10(c). The addition of the back-poling step resolved the large-scale patchiness of the periodic poling, in conjunction with increasing the periodic poling charge target to accommodate poling through the thickness of the sample. The duty cycle, however, ranged from 50% to complete merging of adjacent domains, with duty cycles from 59% to 90% visible in the representative $\approx$ 250μm by 150μm area shown in Fig. 3·10(c). The poling was adequate for SPDC and interferometry with a constant poling period, had borderline performance for linearly chirped poling, and was inadequate for apodized poling due to unwanted extra frequency components in the poling lattice (see Chapter 5).

3.2.4.3.3 Nucleation and duty cycle homogeneity Closer investigation revealed that the duty cycle inhomogeneity persisted regardless of the initial duty cycle of the resist window, even for samples without waveguides. This suggests that the problem lies at least partially in the poling methodology, as opposed to defects caused by titanium diffusion. A representative experiment performed with a range of design duty cycles in a sample without waveguides (but *with* back-poling, to ensure a uniform starting polarity) is shown in Fig. 3·11. Fig. 3·11(a) shows the photomask used for the experiment. Each column has a different duty cycle; the period is 9.5μm

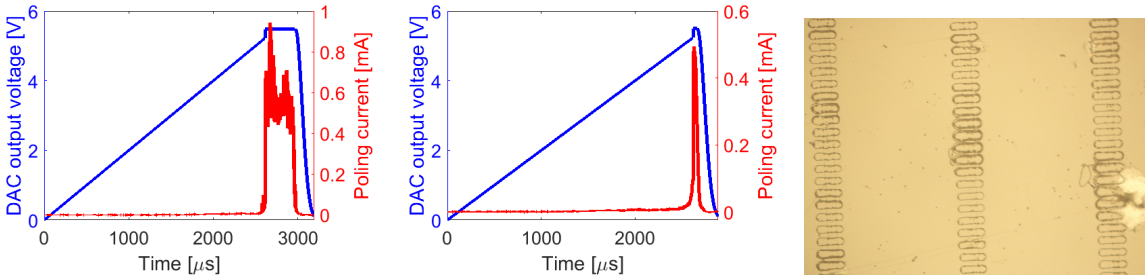

(a) (b) (c)

Figure 3·10: Back-poling (a) and periodic poling (b) waveforms for the sample that yielded most of the SPDC and two-photon polarization interferometry results, and a representative image of poling quality in that sample, revealed by etching in HF (c). Inverted domain boundaries are at the outer edge of each oval. The macroscopically patchy poling from Fig. 3·9 is resolved, but there is still a large variation in the duty cycle (59% to 90% in this image).

throughout, and from left to right the duty cycles are 30% (2.85μm), 25% (2.74μm), and 20% (1.90μm). Fig. 3·11(b) shows the resist windows. The resist window width increases uniformly in the projection from mask to photoresist due to resolution limitations of the SUSS MicroTek MA6 mask aligner used in this work (see Appendix A), but the duty cycle remains homogeneous in each column. After poling, the sample is briefly etched in HF to reveal the domain inversion, shown in Fig. 3·11(c). The 30% duty cycle design is clearly unsuitable, as more than half of the domains merge with their nearest neighbor. The column designed for 25% resulted in a mean duty cycle of $79 \pm 11\%$. The 20% column performed best, with mean duty cycles $62 \pm 11\%$.

The duty cycle variation in Fig. 3·10(c) and Fig. 3·11 and the patchy poling in Fig. 3·9 can be explained by uneven domain nucleation, which was improved in the final batch of samples with a combination of NiCr electrodes and a modified poling waveform. The effects of uneven nucleation are illustrated schematically in Fig. 3·12. If nucleation occurs at all of the electrodes but at different times, the resulting domain grating will have constant period but inhomogeneous duty cycle as in Fig. 3·10(c).

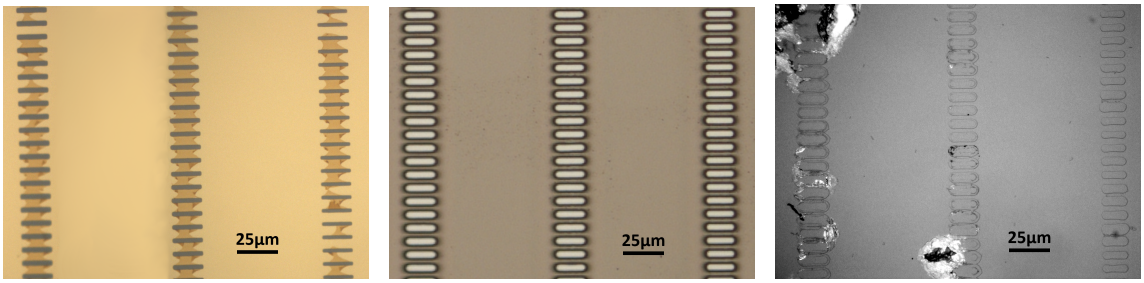

(a) (b) (c)

Figure 3·11: Demonstration of poling-induced duty cycle inhomogeneity. Each column was poled with a different duty cycle, with period 9.5μm. A section of photomask with a 9.5μm period and three different duty cycles is shown in (a). From left to right the duty cycles are 30%, 25%, and 20%. The photolithography is shown in (b). The domains revealed by HF etching after poling are shown in (c), illustrating the poling-induced non-uniformity of the duty cycle.

If nucleation only occurs at electrodes in some areas of the sample, domains will be missing or fragmented as in Fig. 3·9. As discussed in Section 3.2.4.2, metal electrodes, and NiCr in particular, can improve nucleation site density along the electrode edges by up to a factor of 20 compared to resist windows (Miller, 1998). Additionally, simultaneity of the domain nucleation can be improved by adding a short, high-voltage spike to the beginning of poling, as nucleation is effectively instantaneous at fields above 24kV/mm (Miller, 1998).

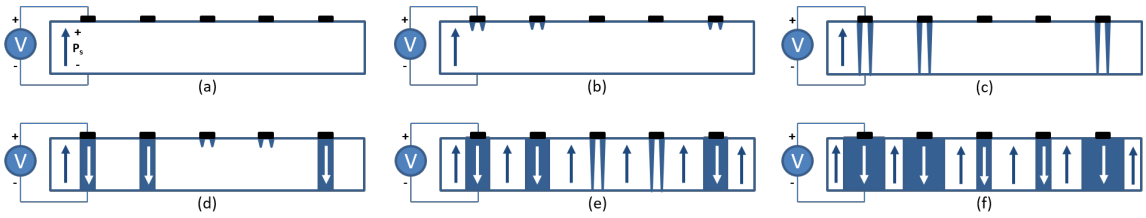

Figure 3·12: Simplified illustration of uneven domain nucleation. Note that the period (measured from center-to-center of the inverted domains) remains constant, but the duty cycle varies.

A diagram of the final poling waveforms used with NiCr electrodes in this work

is shown in Fig. 3·13. The voltage pulse is based on the waveform used in (Batchko et al., 1999), empirically optimized for this application, and implemented with active fast feedback from the FPGA system described in Sec. 3.2.4. The fast-feedback FPGA system is crucial in this methodology for controlling the poling current. First, the FPGA output voltage is ramped linearly from 0V to 5.3625V (10.725kV after amplification) at a rate of 30mA/ms (a), which is slightly below the coercive field. The voltage is then held constant for 10ms to allow for relaxation of piezoelectric strain on the crystal (b), and then discontinuously increased to 7V (14kV) and held for 0.1ms to initiate poling and rapidly nucleate the domains (c). The voltage then quickly ramps down at 900mA/ms until the poling current reduces to 1mA (d). Poling proceeds at this voltage until the current falls below 0.1mA, signifying the end of poling (e). The voltage then ramps down again at 900mA/ms until it returns to the hold voltage (f), where it waits again for 10ms (g). Finally, the voltage is ramped down at 30mA/ms (h). If the sample breaks during step (e), the fast ramp-down is engaged until the current falls below 100mA; this usually prevents the sample from completely shattering, and the only sign of dielectric breakdown is a single pinprick hole burned through the sample ($\approx 100\mu$m diameter). If the sample has accumulated enough charge, it can still be used for optical tests as the hole typically only damages one or two waveguides.

3.2.4.3.4 Final apodized Type-II samples The final experimental results in this work were achieved with a sample poled with the above methodology of NiCr electrodes under photoresist with fast feedback. The backpoling and periodic poling waveforms are shown in Fig. 3·14(a) and (b), and an HF-etched region of a sample poled with similar parameters is shown in Fig. 3·14(c). There was some current noise towards the end of back-poling, but this is common and does not affect the final result. The periodic poling was programmed to terminate when the accumulated

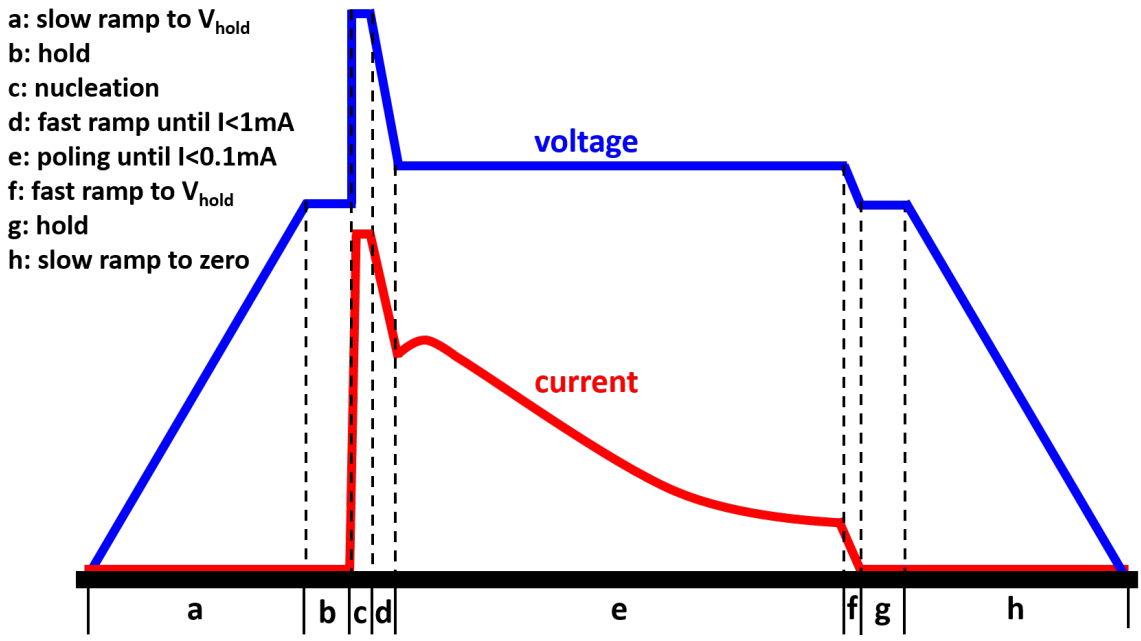

Figure 3·13: Diagram of optimized poling waveform for use with NiCr electrodes. Axes are not to scale. The general form of the voltage pulse is based on (Batchko et al., 1999), with the addition of fast feedback and empirical optimization of the static voltage levels and ramp rates.

charge reached 70μC, but the sample developed a small hole at 67.4μC. The hole only damaged one waveguide and the accumulated charge was within 4% of the design target, so this sample was used for optical tests reported in Chapter 4. The duty cycle was significantly more homogeneous than previous tests. Multiple images like Fig. 3·14(c) taken at random locations in the sample and analyzed with MATLAB's image processing and signal processing toolboxes yielded a mean duty cycle of 66$\pm$2%.

3.2.4.4 Dielectric breakdown during poling

Even with optimization of the poling waveforms, the majority of periodic poling attempts ended with either a small burn or the sample completely shattering. This sharply limited the number of samples available for optical testing. A few other au-

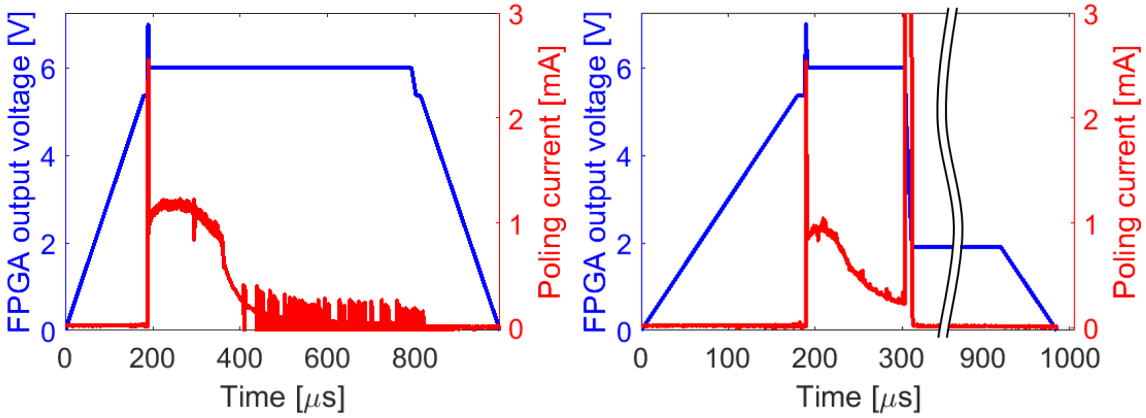

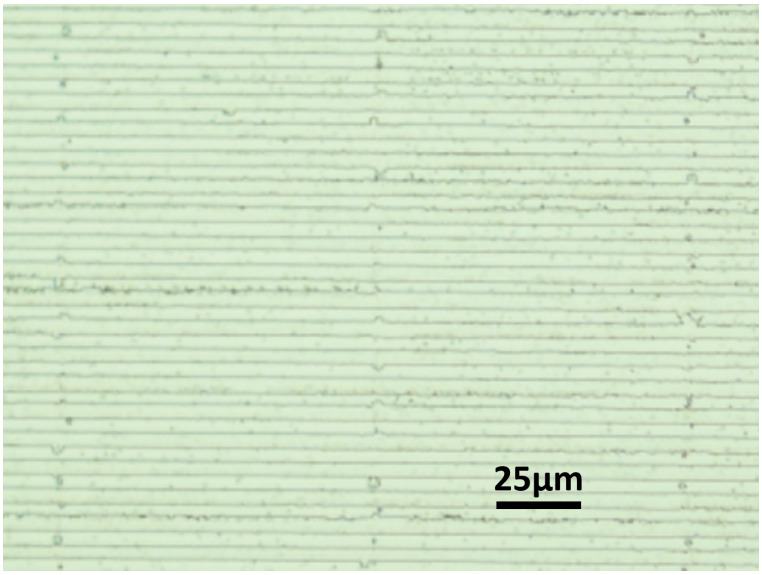

Figure 3·14: Back-poling (a) and periodic poling (b) waveforms for the final apodized SPDC methodology, with representative HF-etched domains (c). The vertical lines of dots are regions of swelling on top of the waveguides. The mean duty cycle is $66 \pm 2\%$

thors have successfully fabricated and tested Ti:PPLN devices, but their reported fabrication methodologies leave out many key details. Other authors also do not report typical breakage rates other than to note that some breakage during poling is normal, particularly for ground and back-poled titanium-diffused samples that

may have grinding-induced thickness inhomogeneities or other microscopic damage from mechanical and/or thermal stress. Personal communication with an alumnus of the Integrated Quantum Optics group at the University of Paderborn suggests that around 25% of their Ti:PPLN samples break during periodic poling. In this work the rate was nearly three times that, plus attrition at other stages of fabrication (*e.g.*, during grinding, back-poling, or polishing the endfaces for optical testing), despite the beginning of this work drawing on the published details of the Paderborn and Stanford procedures and then optimizing the lithography, grinding, and poling over dozens of fabrication runs. To maximize transparency, a detailed account of the this work's entire fabrication procedure is given in Appendix A.

Chapter 4

Type-0 QFC in Ti:PPLN

4.1 Design and predicted performance

Quantum frequency conversion (QFC) is the conversion of a single photon from one wavelength to another. QFC has applications as an intermediary between quantum memories or quantum information processing systems and the telecom band (Fernandez-Gonzalvo et al., 2013). QFC also has promise as an enabling technology for detection of weak signals at wavelengths where no suitable detectors exist, by shifting the photon to a wavelength where high-efficiency, low-noise detectors are available (i.e., the visible band).

QFC is a stimulated process achieved through sum- or difference-frequency generation, and requires the high conversion efficiency only possible in periodically poled waveguides. It was thus a good initial testing ground to demonstrate Ti:PPLN devices with low loss and high conversion efficiency. Even though Ti:PPLN can support Type-0, -I, and -II interactions, initial tests were performed with Type 0 due to the larger nonlinear coefficient and the relative ease of fabricating larger domains. Samples were designed to convert 1550nm photons to 853nm, mediated by an 1897nm pump. The goal of conversion between these frequencies is integration of metastable xenon quantum memory systems (such as those investigated by our collaborators at University of Rochester (Hickman, 2017)) into conventional telecommunications networks, as shown in Fig. 4·1. The pump is chosen to be on the red side of the signal to avoid conversion of the pumps Raman scattering, which would appear as spurious

photons at the QFC wavelength (Kuo et al., 2013)(Thomas et al., 2015).

The QFC samples were designed for operation at 80C with poling period 20.8μm. Fabrication of the devices followed the procedure in Appendix A, with the omission of the backgrinding and backpoling steps which were introduced later. Due to laser availability, conversion is demonstrated from 1897nm to 853nm using a 1550nm pump, instead of converting from 1550nm to 853nm with an 1897nm pump. These are complementary processes, and demonstration of one shows that the device is also suitable for the other.

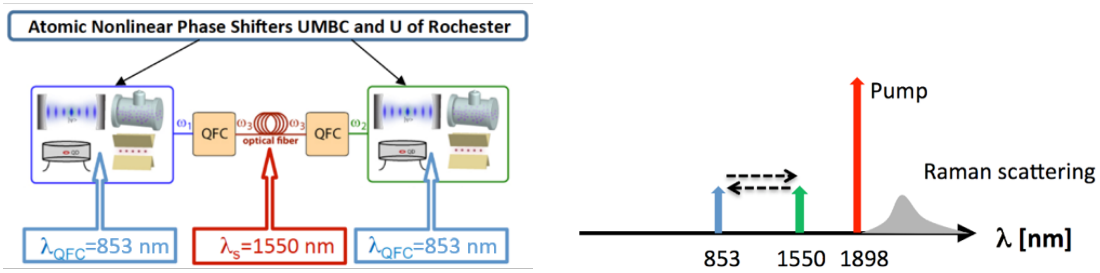

Figure 4·1: Motivation for QFC experiments (a), and selection of pump wavelength to avoid conversion of Stokes Raman scattering (b).

4.2 Experiment setup

The experimental apparatus is shown in Fig. 4·2. For quntum experiments the pump laser is a 1550nm PicoQuant pulsed diode laser with 4ps pulse width and 1MHz rep rate, amplified by an erbium doped fiber amplifier (EDFA) with 80mW peak output power. The signal laser is a Thorlabs 1.9um tunable external cavity laser, attenuated by a JDS fiber attenuator to an average of 1 photon per pump pulse (1 photon per 4ps at 1.9μm = 26nW). Both lasers are fiber pigtailed and pass through polarization adjustment paddles before being combined on a wavelength division multiplexer (WDM). The beams are launched into free space and coupled in and out of the sample

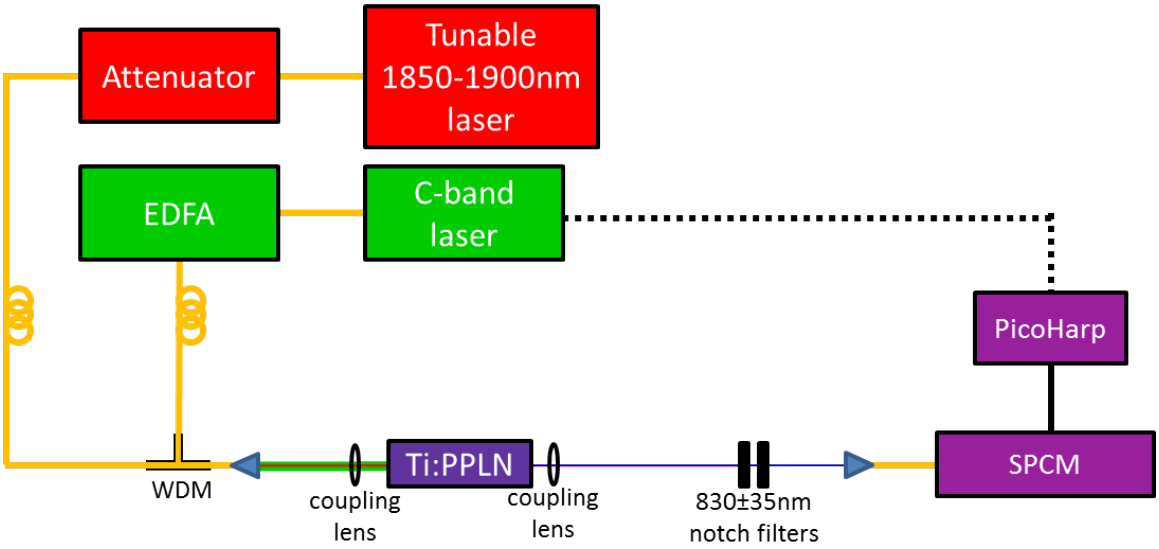

Figure 4·2: Setup for QFC experiments. A tunable c-band laser and an EDFA were used to generate wavelength tuning curves and conversion spectra; all other measurements were taken with a pulsed 1550nm laser attenuated through an adjustable fiber attenuator.

using aspheric lenses. The sample is mounted in a heated chuck on a 5-axis stage to facilitate alignment and allow easy lateral translation of the sample to bring different waveguides into the beam path. The output of the waveguide is filtered with a stack of 830 +/- 35nm notch filters to reject the pump and signal, and the idler is coupled back into fiber and detected on a PerkinElmer SPCM-AQR-15 silicon single photon counting module (SPCM). The electrical output of the SPCM and the trigger from the PicoQuant are sent to a PicoHarp 300 coincidence detector. For classical measurements of the SFG bandwidth, the pulsed pump laser is replaced with a continuous-wave tunable C-band external cavity diode laser and the single photon detector is replaced with an OceanOptics USB+ spectrometer.

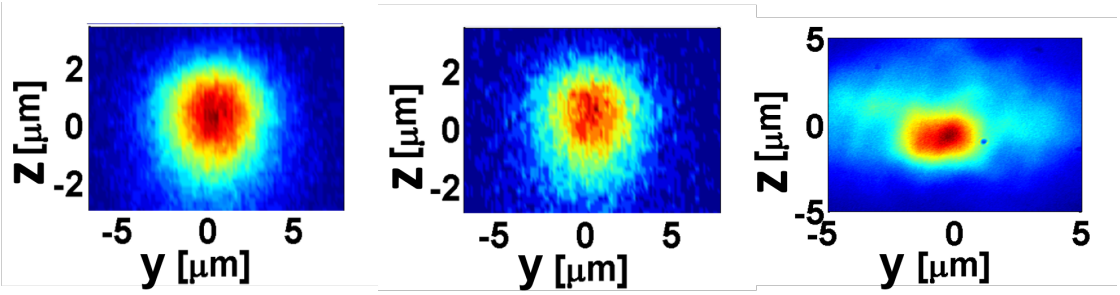

Figure 4·3: From L to R: measured 1550nm TM-like (e), 1550nm TE-like (o), and 843nm TM-like (e) mode profiles. Z and y are crystallographic axes; the waveguide is x-propagating. The 1550nm mode profiles have $> 90\%$ overlap with a standard SMF-28 fiber.

4.3 Results

Mode profiles are shown in Fig. 4·3, and The waveguides demonstrate single-mode operation at 1550nm, and can produce single-mode QFC at 843nm. The 1550 modes have $> 90\%$ overlap with the mode of a standard SMF-28 fiber.

QFC data are shown in Fig. 4·4. Single-photon conversion efficiency was measured up to 75%, with a signal-to-noise ratio of 430 and measured tuning curves that match well with prediction. This result compares favorably with other Type-I QFC results in the literature (Kuo et al., 2013), and is the first reported implementation of 1848nm to 843nm QFC in a Ti:PPLN waveguide (Thomas et al., 2015).

The QFC conversion efficiency is shown in Fig. 4·4(a). Points are measured efficiency at each pump power, and the experiment is configured so 100% conversion efficiency corresponds to detection of one QFC photon per detection gate. Error bars represent a combination of $\sqrt{N}$ Poisson noise, detector dark counts, and unwanted counts from stray pump photons. The signal-to-noise ratio in Fig. 4·4(b) is not intrinsic to the QFC process. Rather, it reflects a combination of both the inherent limitation of photon shot noise and the practical limitations of imperfect filtering and

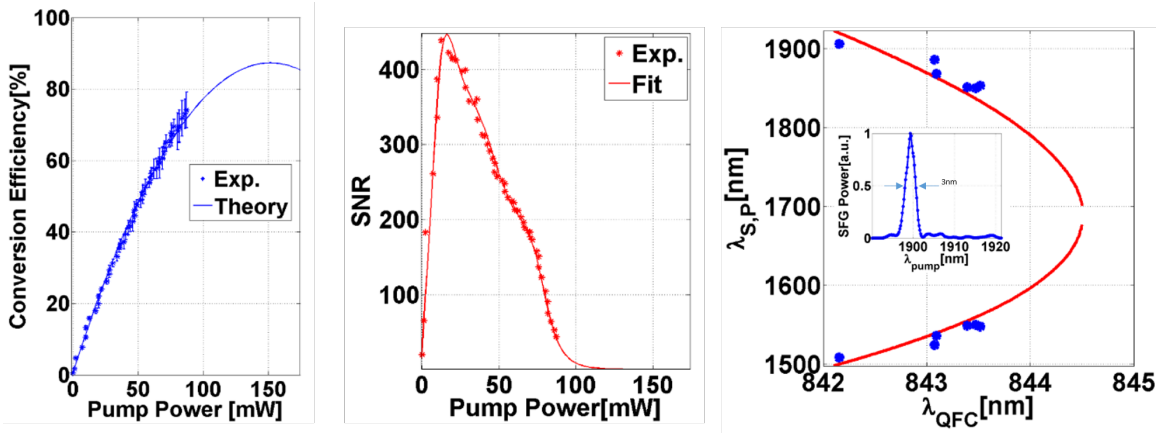

Figure 4·4: Results of QFC measurements. From L to R: conversion efficiency, signal-to-noise ratio, and wavelength tuning curves. Points are measured data, and lines in (a) and (c) are fits based on the coupled mode equations. The polynomial fit in (b) is to guide the eye.

detection.

The wavelength tuning characteristics of the device agree with predictions from simulation of the coupled mode equations, with the exception of a 10nm offset from the design QFC wavelength. While the samples were designed for peak conversion to 853nm at 80C, the peak QFC efficiency was at 843nm (see Fig. 4·4(c)), likely due to novice fabrication errors. While it is possible to compensate this offset with temperature tuning, a shift of 10nm would have required a 50C increase to 130C, which the first-generation heated sample chuck used in this work was not capable of delivering. Later generations of samples did not have this offset, and typically achieve phase matching at the desired wavelength within 10C of the design temperature. The heater was also rebuilt to accommodate higher temperature operation.

Chapter 5

Type-II SPDC/SH in Ti:PPLN and two-photon quantum polarization interferometry

5.1 Unchirped Type-II

5.1.1 SH experiment and results

Results from preliminary tests on 16mm long waveguides with unchirped domains are shown in Fig.5·1 (see Fig. 3·10 for fabrication details), beginning with a study of second harmonic generation in this device. The device is pumped with narrow-band 1561.8nm laser light from a tunable Sacher Lynx laser. Fig.5·1(a) shows the normalized SH phase matching spectrum obtained by sweeping the pump laser wavelength. The location of the center of the spectrum is adjusted by tuning the sample temperature. The measured data (blue asterisks) agree well with the simulation (red line), and both have a full width at half maximum (FWHM) of 0.3nm. This indicates that the poling spans the length of the waveguide, and there are not and large gaps. If only part of the waveguide was poled, the effective length would be shorter and the spectrum would be broader than expected. The duty cycle variation discussed in Chapter 3 reduces the peak efficiency, but does not alter the shape of the unchirped spectrum enough to be measurable with the detection sensitivity of the spectrometer. Ideally, the poling would be characterized by measuring the SPDC spectrum directly, but it is too dim for a direct spectral measurement. For samples with uniform peri-

odic poling, SH phase matching bandwidth is identical to the SPDC bandwidth but about 3.5 times narrower (full details in Appendix B). Fig.5·1(b) proves that the SH is from Type-II phase matching; the SH power is zero for purely horizontal or vertical pump polarization $(0°, 90°)$, and maximized for diagonal or anti-diagonal polarization $(45°, 135°)$.

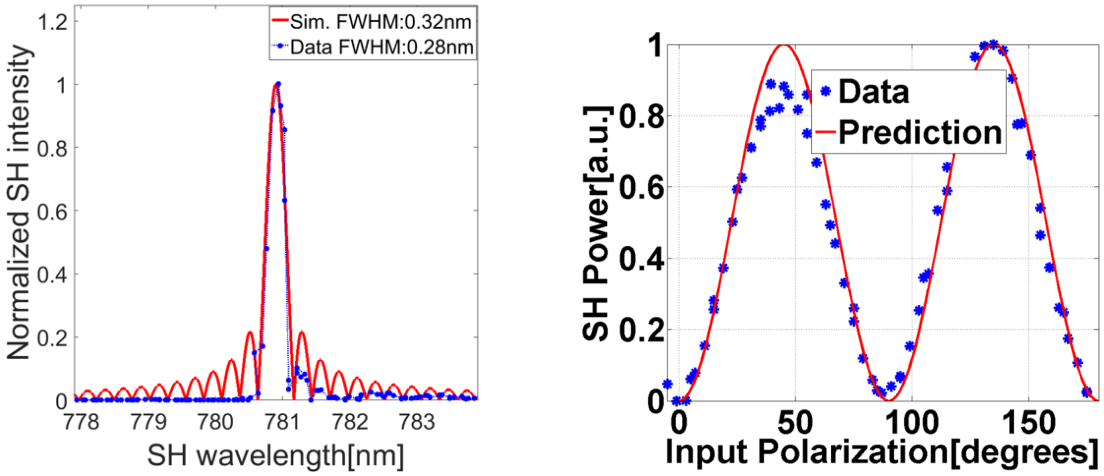

(a) (b)

Figure 5·1: SH spectrum (a) and intensity as a function of input polarization (b) for an unchirped Type-II sample. SH power is maximized with D or A polarized input, but reduces to zero for H or V, as expected. Blue points are measured data and red lines are simulations.

5.1.2 Two-photon interferometry experiment setup

The experimental apparatus for quantum interferometry is shown in Fig. 5·2. The Ti:PPLN waveguide is pumped by a narrowband 780.9 nm diode-pumped solid state laser. The power of the beam is adjusted with a half-wave plate and polarizing beam-splitter cube, which also enforces horizontal polarization. The pump is coupled in and out of the waveguide in free space with aspheric lenses. The pump is filtered out after the waveguide, and the intrinsic birefringent delay between the orthogonally polarized signal and idler photons is compensated by a total of 4cm of z-cut quartz.

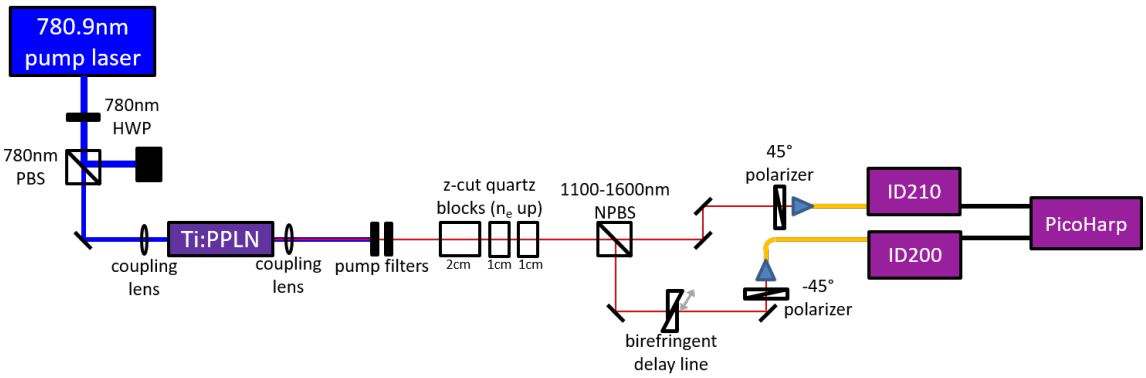

Figure 5·2: Setup for 2-photon polarization interferometry experiments.

The down-converted photons are split into two paths by a non-polarizing beamsplitter cube, and a variable birefringent (z-cut quartz) delay is introduced in one arm to introduce a phase delay between the signal and idler photons. Both arms of the interferometer have analyzers at $\pm 45°$ projecting the signal and idler photons into the diagonal/antidiagonal basis before detection to erase polarization distinguishability. The photons are detected on idQuantique ID210 and ID200 detectors, and coincidences are detected on a PicoHarp 300 coincidence counter.

5.1.3 Two-photon interferometry results and troubleshooting

Early measurements of SPDC were promising. Fig. 5·3 shows a few fringes from the center of the interferogram, taken with 100kHz trigger and 20us gate width on the SPCMs. The available birefringent delay lines were too short to trace out the entire interferogram envelope (73mm of quartz at 16.3fs/mm, for a maximum delay of 1.2ps), but the central fringes indicate the quality of the interference. As before, data are shown in blue and simulation in red. The measured period of 5.93fs is close to the predicted value of 6.34fs. The measured visibility of 74.2% is lower than expected, indicating distinguishability between the signal and idler photons.

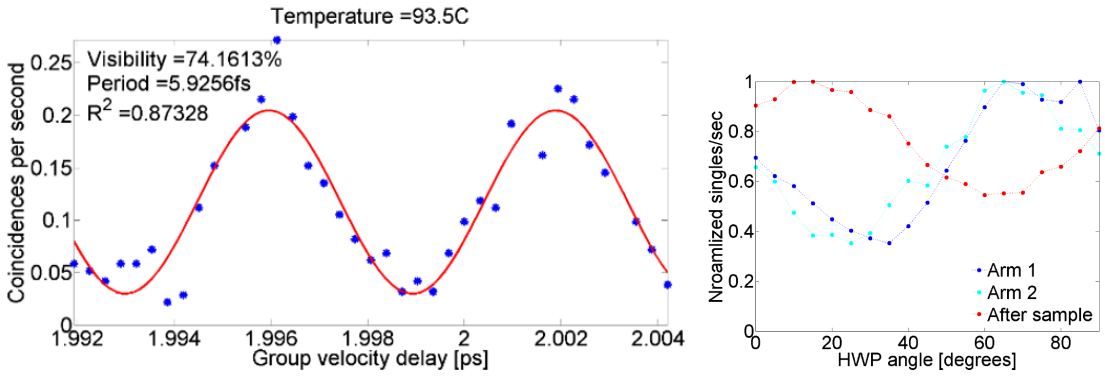

Figure 5·3: 2-photon polarization interferogram from an unchirped Type-II SPDC sample at 90.5C, integrated for 300s at each point with 1mW of pump power (a), and distinguishability of H, V polarized photons at th end of each arm of the interferometer and immediately after the waveguide (b). Points are measured data, and lines are sinusoidal fits. The poling data for this sample are in Fig. 3·10.

In an attempt to isolate the origin of the reduced interferogram visibility, the distinguishability of the H and V polarizations is measured in different locations in the interferometer by placing a half-wave plate in front of the polarizer. If the horizontal and vertical polarizations have identical amplitudes, rotating the polarizer will have no effect. Any difference in amplitude results in an oscillation between the H amplitude and the V amplitude. The amplitude S of the single photon ('singles') fringe limits visibility T of the two-photon interference to $T = \sqrt{1 - S^2}$ (Jaeger et al., 1993).

The results of this measurement in arms 1 and 2 are shown in blue and cyan in Fig. 5·3(b). The fringe visibility in both arms is 48%, which limits the 2-photon interferogram visibility to 88%. Repeating this measurement with the HWP, polarizer, and detector moved to immediately after the sample gives the data in red, with visibility 29% limiting the 2-photon interferogram visibility to 96%. The lower singles visibility at the output of the waveguide means that while the H and V polarizations

exit the sample with different amplitudes, most of the distinguishability comes from the interferometer itself. A likely culprit is spatial walk-off between the H and V modes in the birefringent delay elements, or a wedge in the sample end face resulting in different refraction of H and V as they exit the waveguide.

While it is theoretically possible to adjust the interferometer alignment to compensate walk-off between the polarization modes, this type of fine alignment proved nearly impossible due to low count rates. The SPDC power loss budget for the simplest case of unchirped Ti:PPLN 2-photon quantum interferometry is summarized in Table 5.1. Starting with 100% of the generated SPDC photons immediately after the wavguide, losses and detector parameters result in detection of no more that 0.06% of the generated photons. Detected power varies depending on detector model and settings; this work used an ID Quantique ID200 and an ID210, with maximum quantum efficiencies of 10% and 25%. The maximum power with gating is based off the fastest feasible trigger rate (1MHz) and longest gate open time (20ns) available to both detectors, leading to a maximum gate-open duty cycle of 2%. The peak coincidence rates in all two-photon experiments conducted in this work were less that 1 coincidence per second, making live manual optimization of the alignment impossible. Instead, the experiment is aligned by coupling a 1560nm laser through the sample (attenuated, so it will not damage the SPCMs) and using it to align the interferometer optics and the detectors. The 1560nm laser is then turned off, and the 780nm pump laser coupled into the sample without touching any optical elements downstream from the waveguide.

Table 5.1: SPDC power loss budget for unchirped Ti:PPLN 2-photon quantum interferometry experiment.

After element	SPDC power remaining
Waveguide	100%
Pump filters	94%
Static delay	80%
Beamsplitter	39%
Birefringent delay line	34%
Polarization analyzer	15%
1560nm filter	13%
Fiber to detector	9%
Max possible detected power (free-running)	1-2%
Max detected power with gating	0.02-0.06%

5.2 Linearly-chirped Type-II

5.2.1 SH results

Initial experimental tests of chirped structures were restricted to simple 1% linear chirps. As before, the sample length is 16.5mm. The SH spectrum is shown in Fig. 5·4(b). Qualitatively, the data have the expected shape – a steep-walled, flat-topped structure with ripples. The FWHM of the data, though, is more than three times narrower than the predicted SH spectrum. This is likely due to a combination of duty cycle variation and missing domains, particularly at the ends of the sample. A wedge between the sample and the photomask during resist window lithography can also add an unwanted linear chirp to the domains. An edge-bead removal step was added to the lithography procedure after this sample, and later batches were designed for only 10mm of poled length to avoid truncating the electrode pattern.

5.2.2 Two-photon interferometry results

A few representative fringes from the center of the interferogram are shown in Fig. 5·4(a). As in the unchirped case, the fringe period (6.16fs) is close to the predicted value of 6.34fs. The measured 57% visibility is both lower than predicted and lower than the

unchirped case, but is still non-classical and indicates a small degree of entanglement (Rarity et al., 2005). The distinguishability is likely due to a combination of imperfect alignment of the experimental apparatus and inherent asymmetry of the H and V photon amplitudes, as discussed above. Asymmetric spectra also introduce spectral distinguishability, which further lowers the interferogram visibility.

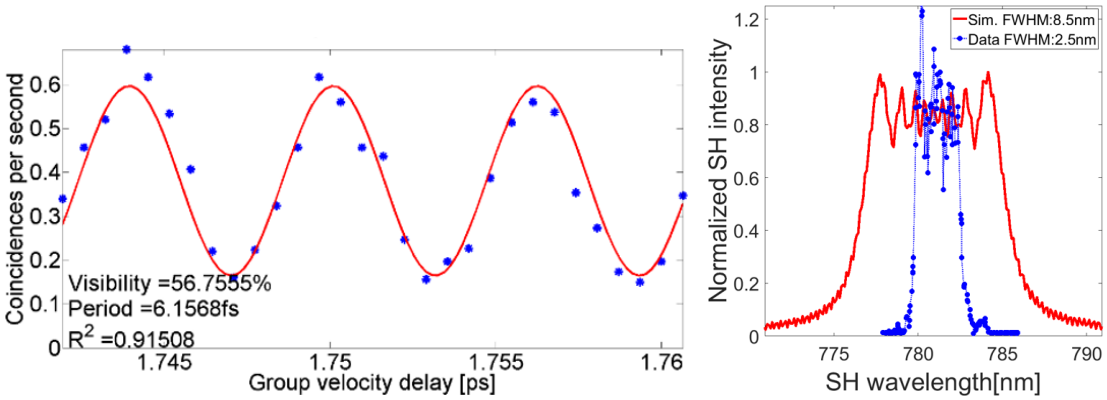

(a) (b)

Figure 5·4: 2-photon polarization interferogram from a linearly-chirped (1%) Type-II SPDC sample at 93.5C with 2.5mW pump and integrated for 300s per point (a), and the corresponding SH spectrum (b). Blue points are measured data. The red curve is a sinusoidal fit in (a), and the simulated SH spectrum in (b). The poling data for this sample are in Fig. 3·10.

5.3 Apodized chirp Type-II

5.3.1 Design of apodized poling

Optimal apodized poling profiles are found in MATLAB through a genetic algorithm which minimizes the FWHM of the interferogram (Van Camp et al., 2016). A comparison of unchirped, linearly chirped, and two different apodized poling profiles is shown in Fig. 5·5. For a sample of length 16.5mm, introducing a 1% linear chirp to the poling period increases the SPDC bandwidth from 2.3nm to 31nm and narrows

the interferogram envelope from 1.9ps to 137fs. The visibility of the interferogram remains high at 97%, but has unwanted side lobes that reduce its suitability for sensing applications (see Chapter 1). The genetic algorithm apodizes the linear chirp to narrow and smooth the interferogram envelope. The optimal apodized design broadens the spectral bandwidth to 73nm and narrows the interferogram envelope to 65fs while supressing the side lobes. The visibility, however, decreases to 65%, and falls off rapidly if the interferogram is narrowed any further via this method. The final row is a simplified, easier to fabricate version of the apodized design, with SPDC spectral bandwidth 35nm, interferogram FWHM 120fs, and visibility 94%.

Using the current algorithm, attempts to narrow the interferogram further in simulation have not been successful. The visibility of the interferogram decreases much faster than the width of the envelope. This degradation in visibility makes intuitive sense from the perspective of spectral phase and distinguishability. The more dramatic the chirp, the more the origin of each spectral component becomes localized to a particular region of the sample. This distinguishability takes the form of a spectral phase, which is mathematically responsible for reducing the interferogram visibility (see Chapter 6 for details). Future work will involve investigating other poling designs that might ameliorate the spectral phase.

5.3.2 SH results

The best experimental results obtained from an apodized poling profile are shown in Fig. 5·6, with poling data using the NiCr-under-resist methodology shown in Fig. 3·14. The SH spectrum is noisy and unusually dim, but the measured FWHM of 4.1nm agrees well with the predicted FWHM of 4.6nm. The agreement between simulation and experiment indicates that the poling issues are largely resolved, and that the final poling methodology successfully created the designed domain pattern.

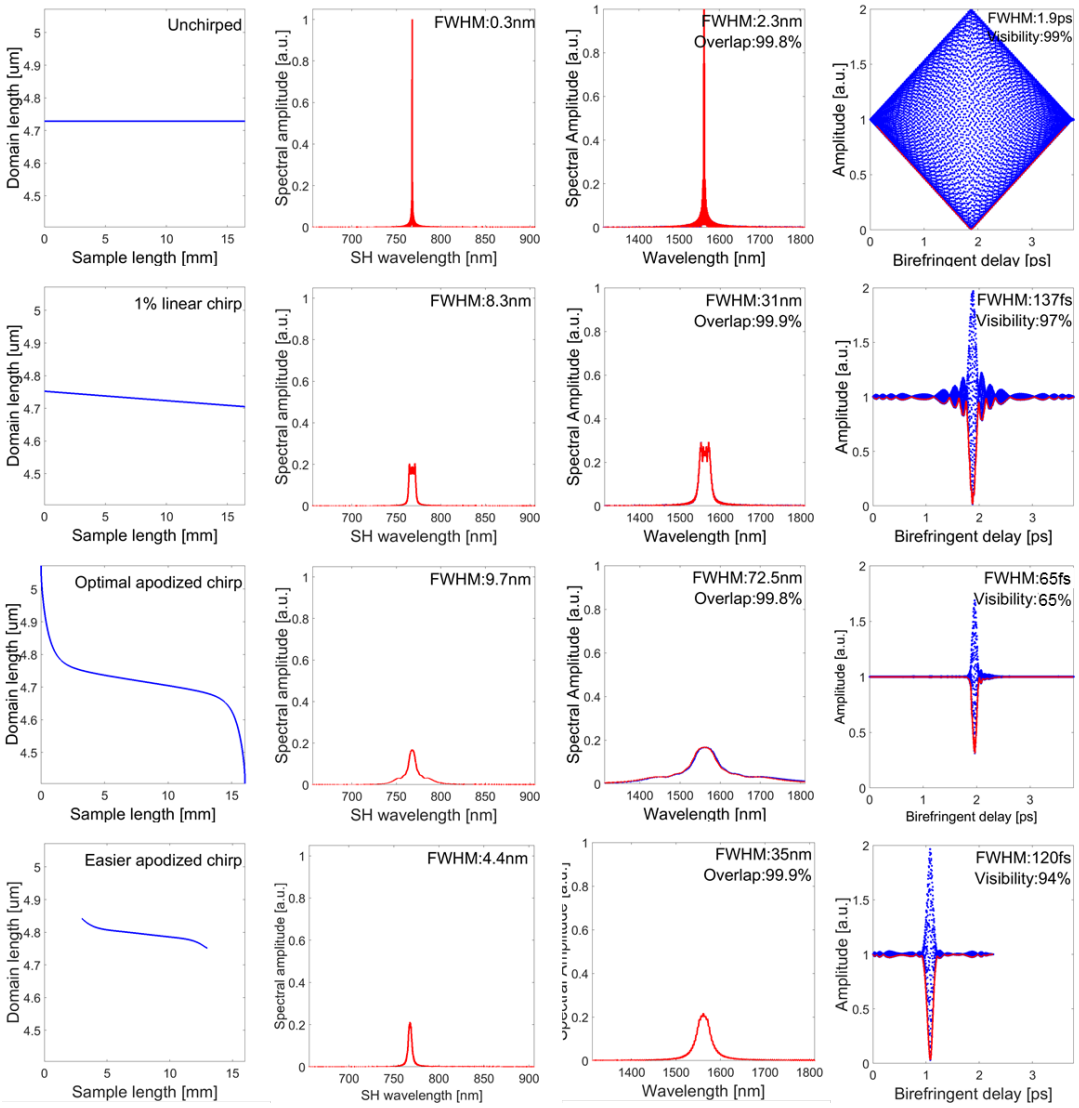

Figure 5·5: From left to right: poling profile, simulated SH and SPDC spectra, and interferograms. From top to bottom: unchirped poling, 1% linear chirp, optimal apodized linear chirp, and a simplified apodized chirp designed for easier fabrication. The first 3 designs are in a 16.5mm waveguide, and the easier apodized chirp is in a 10mm waveguide. All are designed for operation at 165C, and all interferograms are comprised of fast, 6.34fs period fringes.

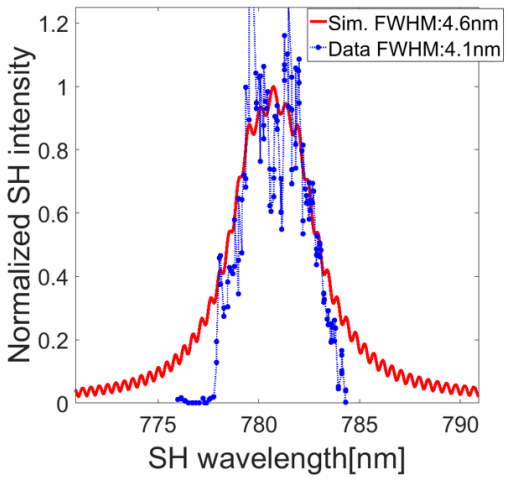

Figure 5·6: Best SH spectrum obtained from the final batch of apodized samples. The poling data for this sample are in Fig. 3·14

5.3.3 SPDC results and troubleshooting

The SPDC conversion efficiency also indicated high-quality poling. A measurement of the single-photon counts with 1.3mW pump, 90kHz trigger, 25ns gate, and 25% quantum efficiency on the ID210 SPCM yielded 39.1 single-photon counts per second. Taking into account the losses and detection efficiencies of Table 5.1 along with the predicted waveguide mode profiles, this implies that 605333 SPDC photons are generated per second for a conversion efficiency of 1.2E-10, or 9.2E-6%/W. This is actually four times *higher* than the predicted conversion efficiency of 2.9E-11. While some of this discrepancy is likely due to imperfect measurement of the losses, this also could imply that the actual waveguide modes in this sample are smaller than in the simulation, or that the average pump power in the waveguide is higher than the measured pump power at the output face.

The apodized sample suffers from unusual difficulties with guidance of TM-like (vertical/extraordinary polarized) modes at 1560nm. With 7.0mW of 1560nm power at the input facet, for example, the peak coupled power as measured at the output

Table 5.2: Total waveguide transmission efficiencies for H, V polarized light in the final apodized sample (output power/input power; includes coupling efficiency and scattering loss).

Wavelength	Input power	H (o, TE)	V (e, TM)
633nm	0.1mW	17%	15%
780nm	5.0mW	22%	18%
1560nm	7.0mw	21%	0.7%

facet is 1.5mW (21%) for horizontal polarization and only 50μW (0.7%) for vertical polarization. The 633nm HeNe laser (used for alignment) and the 780nm pump laser both have much more balanced H and V transmission through the sample, within the bounds of expected operation (17% and 15% for 633nm, and 22% and 18% for 780nm). The SH spectrum indicates that the small amount of vertically polarized 1560nm light guided through the sample is adequate to drive a stimulated process (albeit with low efficiency), but measurements of the SDPC H/V distinguishability indicate that *zero* vertically polarized SPDC photons are detected. This does not contradict the high SPDC efficiency reported above, as it is driven by a 780nm pump and it is still possibly to measure high efficiency conversion when half of each pair is lost. The loss of the vertically-polarized photons does, however, mean that the sample is unsuitable for two-photon quantum interferometry. This was confirmed by measuring the H/V photon distinguishability at the output of the waveguide, which confirmed that the surviving number of vertically-polarized photons was immeasurably small (Fig. 5·7).

It is unclear why this sample was unable to guide 1560nm TM-like modes. The waveguides were fabricated with the same parameters and processes as all previous samples, so low-frequency cutoff should not be a problem; the waveguide would need to be about 50% smaller for TM-mode cutoff to be an issue, which is an order of magnitude beyond typical batch-to-batch variations. The only difference in this round of fabrication was the change to NiCr electrodes. One theory is that the NiCr electrodes

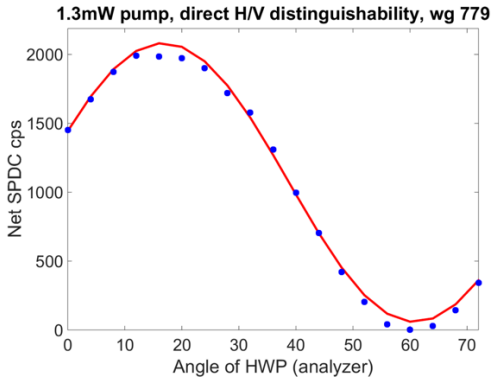

Figure 5·7: SPDC H, V distinguishability measured at the output of the waveguide in the final apodized sample. The poling data for this sample are in Fig. 3·14.

somehow damaged the top surface of the waveguide. The author who originally determined the relative NSD enhancement of various electrodes, including NiCr, did so in bulk LN without waveguides (Miller, 1998). It is possible that NiCr and Ti:LN are not compatible, perhaps due to nickel or chromium causing defects in the lithium niobate and lowering the photorefractive damage threshold. Photorefractive damage almost exclusively affects the extraordinary index, and both nickel and chromium are known LN defect species (Schwesyg, 2011). Pure chromium electrodes may be a useful compromise between NSD and waveguide damage. Other authors have successfully used pure chromium electrodes for poling Ti:LN, but only with constant period and duty cycle (Gui, 2010). Further investigation is needed on the effects of different electrode materials on titanium-diffused LN waveguides.

Chapter 6

Roadmap for future technology development

6.1 Overcoming spectral phase

As mentioned in Chapter 5, the chirping and apodization design methodology used in this work introduces an unwanted spectral phase. This phase broadens the interferogram, reduces fringe visibility, and is the limiting factor in this work's designs of SPDC sources for ultra-high-resolution PMD measurements. Some improvement is possible by deliberately introducing an asymmetry in the poling profile; theory and simulations for this technique are presented below (Thomas et al., 2016). The ultimate solution may lie in correcting the phase *after* photon pair generation.

6.1.1 Origin of spectral phase limitations

Spectral phase negatively impacts interferogram width and visibility because the generated photons are not Fourier transform limited. An optical pulse is transform limited if its time-bandwidth product is as short as possible for the given pulse shape, *i.e.*, if its spectral phase is flat or linear (Arfken and Weber, 2005). Consider the simplest cast of a photon pair generated by SPDC in a perfectly phase-matched sample of length L. The biphoton has uniform probability of being generated at any position along the length of the sample, so in the time domain the biphoton is a rectangular pulse with width equal to the transit time of the pump photon. The result of this indistinguishability is a sawtooth phase — linear overall, but zero at the nodes of

the resulting $sinc^2$ spectrum . The generated photons are transform-limited, and the shape of the interferogram envelope is described by the simple cartoon in Fig. 2·7.

The chirping and apodization methodology described in this work broadens the spectrum, but in doing so it introduces a nonlinear spectral phase and does not meaningfully alter the temporal width of the generated photons. The resulting photons are not transform limited, resulting in an interferogram broader and shorter than expected from the spectrum alone.

There are simple, intuitive explanations for both the nonlinear phase and the pulse width. The spectral phase is nonlinear because the QPM domain size varies along the length of the sample. This variation means that each spectral component is more likely to originate in a *particular location* in the sample, traveling a particular distance to the end face with a particular group velocity and acquiring a particular phase. This "spectral distinguishability *via* phase" worsens as the chirp increases and the origin of each spectral component is more localized, enforcing a hard limit on how narrow the interferogram can become before spectral distinguishability destroys the frequency entanglement entirely. Broaden the spectrum too far, and the photons lose their "quantumness" in the frequency domain.

The temporal width of the SPDC photons is roughly constant regardless of the chirp and apodization because the resulting changes in the effective nonlinear coefficient are small compared to the difference between lithium niobate and air. From the perspective of a pump photon, the discontinuous jump from a nonlinear coefficient of zero to one approximately equal to that of bulk lithium niobate dominates the temporal structure of the resulting biphoton. Chirping alters the effective nonlinear coefficient somewhat, but for the designs used in this work is it not enough to meaningfully alter the photons' temporal width. More aggressive chirping could alter the temporal shape, but at the cost of unacceptable spectral distinguishability.

6.1.2 Asymmetric poling for improved spectral phase

One way to ameliorate the spectral phase by adding a small, deliberate asymmetry to the poling profile. This work included the development and simulations of a non-standard asymmetric poling design that mitigates phase distortions associated with the process of chirping. Asymmetric poling significantly broadens the entangled source bandwidth while preserving high visibility quantum interferometric sensing (Thomas et al., 2016).

Due to the second-order dispersion cancellation effect discussed in Chapter 2, only *odd* orders of the spectral phase impact the interferogram. Linear phase does not limit phase-time bandwidth, as discussed above, so the relevant phase coefficient for optimizing two-photon quantum polarization interferometry is given by the odd orders ≥ 3 of the Talylor expansion of the dispersion-induced phase

$$\delta(\Omega) = \frac{2}{3!}\frac{d^3\phi}{d\Omega^3}\Omega^3 + \frac{2}{5!}\frac{d^5\phi}{d\Omega^5}\Omega^5 + ..., \tag{6.1}$$

where Ω is the detuning from the degenerate signal and idler frequency. The modified expression for the peak coincidence rate (when the group delay between the photons is perfectly compensated) becomes

$$R(\tau_{gr}) = \int_{-\infty}^{\infty} \left| |f(\Omega)| e^{i\omega_0\tau_{ph}} e^{i\delta(\Omega)} + |f(-\Omega)| \right|^2, \tag{6.2}$$

where $f(\Omega) = \tilde{\chi}^{(2)}(\omega_0 - \Omega, \omega_0 + \Omega)$ is the two-photon spectral amplitude, $\tau_{gr} = L\left(\frac{1}{u_H} - \frac{1}{u_V}\right)$ is group delay compensation required to temporally overlap the photons in terms of the waveguide length L and group velocities $u_{H,V}$, and τ_{ph} is the period of the interference fringe.

Some important quantum interference engineering principles emerge from analyzing Eq. 6.2. In order to achieve a 100% visibility of the envelope one must ensure

the coincidence counting rate R vanishes when the average group delay of the source is compensated by the birefringent delay line (BDL). This can be achieved when a spectral component symmetry condition is fulfilled: $|f(\Omega)|\, e^{i\delta(\Omega)} = |f(-\Omega)|$. In other words, two major conditions must be satisfied in the *phase-amplitude parameter space*: $|f(\Omega)| = |f(-\Omega)|$ for the amplitude and $\delta(\Omega) = constant$ for the phase. The latter implies $\delta(\Omega) = 0$ since $\delta(0) = 0$. This is a condition of complete indistinguishability between spectral components of correlated signal and idler waves over the full range of nonlinear phase matching in SPDC process.

A new target function (G) for the optimization process is based on this approach:

$$G(\sigma) = \int d\Omega \left[|\delta(\Omega)|^2 + ||f(\Omega)| - |f(-\Omega)||^2 \right] + \left| FWHM \left\{ |f(\Omega)|^2 \right\} - \sigma \right|^2 \quad (6.3)$$

The first term is a least-squares minimization of the residual phase $\delta(\Omega)$. The second term minimizes the asymmetry between correlated signal and idler spectral amplitudes in each photon pair. The third term is designed to achieve a specified full-width at half maximum (FWHM) bandwidth of the spectral amplitude. The optimization procedure implements a constraint to keep the minimum domain size to be above our lithographically feasible minimum domain size of 4μm. The resulting interferograms obtained using optimization procedure Eq. 6.3 in case of N = 11 is shown in Fig. 6·2. The optimized asymmetric poling profile is illustrated in Fig. 6·1. The resulting interferogram is a clean single peak with a narrow temporal envelope of 54fs FWHM and 90.3% visibility, a significant improvement on the 65fs FWHM and 65% visibility achieved with the GA target function presented in Chapter 2.

6.1.3 Phase correction after pair generation

The most versatile option for ameliorating spectral phase is to decouple the spectral amplitude and phase management. This could be achieved by dispersing the SPDC

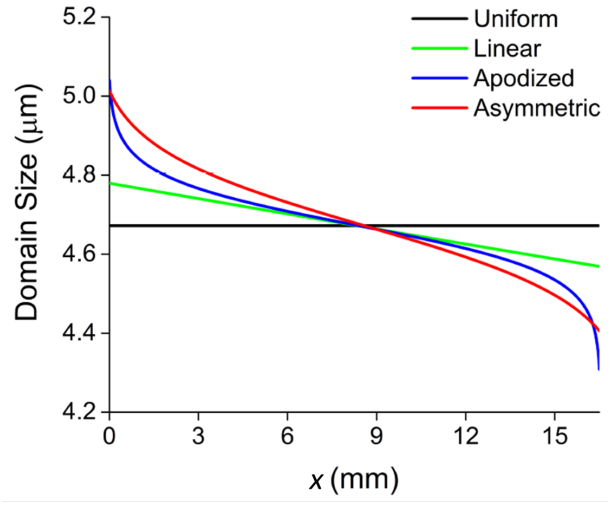

Figure 6·1: Different poling profiles along the length x of the nonlinear crystal interaction region.

on a prism and manipulating the phase with a one-dimensional spatial light modulator (SLM). Electronically addressed spatial light modulars are typically based on an array of liquid crystal cells (HOLOEYE Photonics, 2017b). The phase and/or amplitude of incident light is altered on a pixel-by-pixel basis by changing the potential across each cell, with the mode of operation determined by the liquid crystal material and the light polarization. By dispersing the down-converted photons in a prism, the spectral phase can be corrected in discrete blocks determined by the pixel pitch, pixel fill-factor, and spatial distribution of the light. The HOLOEYE GAEA-TELCO-033 reflective-mode SLM, for example, is 4094 pixels wide with 3.74μm pitch and 90% fill factor and can provide $> 2\pi$ phase modulation at 1550nm with 8-bit phase levels (256 steps). A 200nm spectral window spread over the full width of the sensor could then be spectrally phase-controlled in 0.05nm blocks and $\approx 2\pi/256 = 0.025$rad steps (HOLOEYE Photonics, 2017a). This variety of SLM has the downsides of 1) requiring a specific linear input polarization and 2) having a pixel fill factor less than 100%, which would result in periodic drop-outs in the spectrum. A new gen-

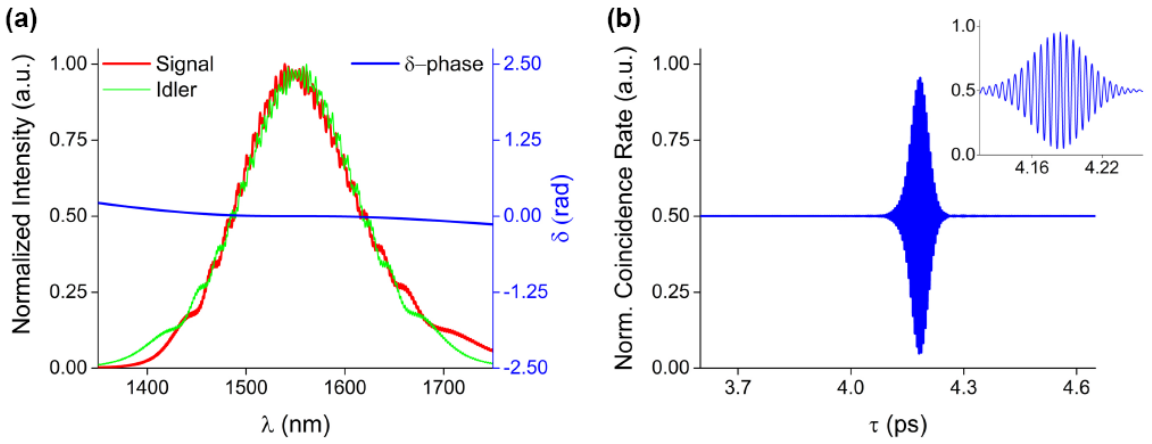

Figure 6·2: The SPDC spectrum, phase δ, and the optimized interferogram produced using poling Eq. 2.37 in case of N = 11. The spectral width of the intensity envelope (FWHM) is 135 nm. The inset illustrates a blow-up of the central portion of the plot illustrating clean oscillations inside a smooth envelope. The interferogram visibility is 90.3% and the FWHM is 54fs

eration of polarization-independent reflection-mode SLMs with 100% fill-factor are in development, however, and may have high-enough performance to phase correct hyperentangled photons for quantum interferometry (Meadowlark Optics, 2017).

6.2 Alternate fabrication methodologies

This work reports samples with either successful guidance of all desired polarizations and wavelengths *or* high-quality engineered poling, but not both. Future work must investigate alternate poling and/or waveguide methodologies to create broadband, efficient SPDC that is suitable for two-photon polarization interferometry.

6.2.1 Poling

6.2.1.1 Electrode material

There are multiple promising avenues for improving the poling methodology, ranging from variations on the present electric-field poling technique to direct laser writing of inverted domains. The simplest option is investigating the effects of alternate electrode materials over Ti:LN waveguides, as an extension of the work of (Miller, 1998). Such experiments would ideally be supplemented with secondary ion mass spectrometry (SIMS), or any other technique capable of mapping the composition and distribution of both the diffused titanium waveguides and the lithium oxide swelling above the waveguides. The goal of these experiments would be testing the theory that the NiCr electrodes are responsible for the poor guidance of 1560nm TM-like modes, and, if that is confirmed, finding the best alternate electrode material.

6.2.1.2 Surface poling

It may also be worth revisiting surface-poled waveguides, which were used in the QFC experiments. Surface poling with resist window electrodes and the slower, DAQ-based poling waveform produced very inhomogeneous poling (Fig. 3·9), but had the dual virtues of not requiring grinding/back-poling and of having a significantly lower breakage rate. One other author has reported successful surface poling with constant duty cycle and period on top of Ti:LN waveguides with breakage rates $< 10\%$ (Janner et al., 2008), but only for Type-0 down conversion and only with modifications to the titanium diffusion recipe (Janner et al., 2007). It is possible that combining the faster, FPGA-based poling waveform and/or metal electrodes with this modified surface poling methodology could yield high-quality chirped and apodized poling with a lower breakage rate.

6.2.1.3 Direct writing

Another avenue of investigation is direct writing of the inverted domains. This is a relatively new area of research and includes both electron beam and laser writing of domains, completely bypassing the need for conventional electric field poling. The electron beam technique has been demonstrated on Ti:LN waveguides in z-cut wafers (Restoin et al., 2001), but with poor duty cycle homogeneity. More recent work in electron beam poling of y-cut wafers with titanium and/or zinc waveguides also struggles with duty cycle homogeneity, and notes that the waveguide diffusion process both locally alters the coercive field and creates "pinning" defects that can impede domain wall motion (electron beam poling yields significantly better domain homogeneity for bulk samples) (Kokhanchik et al., 2012). The small write-window of electron beam lithographs also limits the poled area to less than $1mm^2$, so future work also would require development of a methodology to stitch multiple write areas together without introducing errors in the poling pattern. If these challenges can be overcome, then electron beam poling could be a viable route forward. Domain inversion via intense UV irradiation is also possible, and recent combination of this technique with a thin surface layer of chromium produced the first UV-based domain inversion deep enough for viable QPM in waveguides (Boes, 2016). It remains to be seen, however, if this technology works well with current waveguide fabrication techniques, and if the level of surface damage is tolerable. A recent collaboration based out of the Australian National University has also developed a direct domain writing technique with a femtosecond pulsed infrared laser, and successfully demonstrated second harmonic generation from 815nm to 408nm with a 2.5um period in Ti:LN waveguides (Chen et al., 2016). This is the most promising direct-write methodology, and it is worth investigating if this technique can deliver the necessary precision for apodized poling structures.

6.2.1.4 Light-assisted poling

A compromise between electric field poling and all-optical domain writing is light-assisted poling (LAP) or latent light-assisted poling (LLAP). LAP is a well-established phenomena where illumination of lithium niobate with cw or pulsed UV light during electric field poling reduces the coercive field (V_c). LAP provides a modest reduction in V_c for undoped LN, and a reduction of up to two orders of magnitude for magnesium-oxide-doped LN illuminated with ultrashort pulses (Valdivia et al., 2006). The newer LLAP technique permits illumination of an undoped LN sample up to 10 hours before electric field poling, which reduces the fabrication difficulty by allowing the two steps to be decoupled (Ying et al., 2009). It is worth investigating if LAP or LLAP could improve poling homogeneity without metal electrodes by ameliorating the coercive field inhomogeneities in Ti:LN waveguides, and reduce sample breakage by enabling lower poling voltages.

6.2.2 Waveguides

The waveguide is another potential area for improvement. Diffusion of zinc instead of titanium offers some simplifications to the fabrication technique and might improve poling homogeneity, but is a less mature technology. Ridge waveguides are another option, with methodologies ranging from combined diffusion and wet etching to ion beam milling. Direct writing of buried channel waveguides with pulsed lasers is another active area of research, but not viable for Type-II SPDC as the resulting structures poorly guide TE modes (Burghoff et al., 2007)(Mizeikis, 2012).

6.2.2.1 Diffused zinc channel waveguides

The technique for fabricating zinc-diffused waveguides is quite similar to that for titanium-diffused waveguides, with one key difference – lower diffusion temperature. The reduced diffusion temperature of 930C is sufficient to permit periodic poling

before diffusing, bypassing the difficulties of grinding and back-poling and avoiding any issues with diffusion-induced changes in coercive field and reducing unwanted lithium oxide out-diffusion (Ming, 2005). Zinc waveguides support both TE and TM modes and are resistant to photorefractive damage. The main drawback of zinc-diffused channel waveguides is the typical loss of ≈1dB/cm, compared to ≈ 0.1dB/cm for the best reported titanium-diffused waveguides. The higher loss makes zinc-diffused waveguides less suitable for applications like QFC where the goal is conversion and detection of every incoming signal photon, but for SPDC the loss can be compensated by the zinc waveguide's increased power handling capabilities. Simply increasing the pump power should raise the detected coincidence rates to (or beyond) levels measured in titanium-diffused waveguides, and Type-0 SPDC has already been successfully demonstrated in zinc-diffused LN waveguides (Zaske et al., 2011).

6.2.2.2 Ridge waveguides

The past decade of improvements in wafer bonding and ion implantation techniques have lead to a plurality of methodologies for fabricating LN ridge waveguides. Broadly speaking, these techniques can be divided into those that provide vertical confinement through zinc or titanium diffusion into the ridge structure (Gui, 2010), and those that vertically confine by bonding a thin LN layer to a lower-index substrate before etching (Chang et al., 2016)(Nishida et al., 2003). Some authors combine both techniques, creating compact and highly damage-resistant ridge waveguides (Hartung et al., 2008). Ridge fabrication techniques include wet etching (Hu et al., 2007), reactive ion etching (Gui, 2010), and focused ion beam milling (Hartung et al., 2008). Ridge waveguide losses are typically comparable to zinc-diffused waveguides (≈ 1dB/cm), and could likely work well for an SPDC source for two-photon polarization interferometry. The primary challenges with ridge waveguides would be selection

of a design from the zoo of available options and re-optimization of the poling methodology for a new waveguide geometry. Ridge waveguides likely have the most promise for future development of any of the above methodologies, but would also require the largest additional time investment to optimize for this work.

6.3 Sensing applications

Broadband SPDC and quantum polarization interferometry has applications in measurement of polarization mode dispersion (PMD) (Fraine et al., 2012) and low-coherence quantum optical interferometric tomography (QOCT) (Mohan et al., 2009) (Abouraddy et al., 2002) (Fraine, 2015). Quantum polarization interferometry is theoretically capable of measuring PMD with 10as resolution, which can improve characterization of dispersive elements like wavelength selective switches and multiplexers in metropolitan telecommunications networks or aid in the development and characterization of LCD-based technologies like spatial light modulators. Sub-femtosecond PMD resolution can also improve resolution of stress-induced birefringence in materials like silicon, with applications in semiconductor manufacturing quality control and in ultra-high-resolution fiber sensors. In terms of QOCT, measuring PMD with 10as timing resolution would be equivalent to measuring a 30nm displacement in free space. With the development of appropriate assays, this could be used for biological measurements such as determining if a protein is folded or unfolded. A combination of QOCT and PMD measurements could also be used for all-optical quality-control on birefringent materials such as gallium nitride in layered semiconductor devices.

6.4 Plug-and-play quantum optics

As lithium-niobate-on-insulator and other hybrid technologies mature, quantum interferometric sensors would benefit from full integration onto a chip. Integration

eliminates delicately-aligned free-space optics and adds the ability to integrate sources and detectors. Turning a room full of experimental apparatus into a tailor-made widget with simple inputs and outputs will dramatically increase the practical usefulness of quantum technologies, and make it easier for them to find applications outside the lab. The present integrated nonlinear photonics toolbox includes polarization rotators (van der Tol and Laarhuis, 1991)(Sung, 2013), beamsplitters and WDMs (Thomas, 2010), sources (Sohler et al., 2005), and single-photon detectors (Atikian et al., 2014)(Kahl et al., 2015). Other authors have already demonstrated plug-and-play quantum sources of heralded single photons (Montaut et al., 2017), photon triplets (Krapick et al., 2016), and entangled pairs (Herrmann et al., 2013)(Jin et al., 2014). Attempting full integration of a quantum interferometer is a logical goal, and would support deployment of quantum interferometers for the applications described in the previous section.

Chapter 7

Conclusions

This work broke new ground in aperiodically poled Ti:LN device fabrication, demonstrated QFC at a novel wavelength combination in Ti:LN waveguides, demonstrated the first two-photon quantum polarization interferometry with an aperiodically poled Ti:LN source, implemented engineered aperiodic poling to demonstrate broadened SH with a quasi-gaussian phasematching bandwidth in Ti:LN waveguides, developed a new framework for SPDC source design for two-photon quantum polarization interferometry, and presented a roadmap for future technology development and applications.

Electric field poling of Ti:LN was optimized for chirped and apodized poling with a uniform duty cycle throughout. The final result was a 10mm-long aperiodically poled region with a $66 \pm 2\%]$ duty cycle. This is a marked improvement on the results obtained from conventional poling methodologies presented in the literature, which produced patchy poling and large duty cycle variations. Optimization of the poling included switching to a fast-feedback FPGA system and switching from resist windows to nichrome electrodes.

This work made the first demonstration of quantum frequency conversion from 1848nm to 843nm. The device was designed for integration of a metastable xenon quantum memory into a telecommunications network. The measured single-photon conversion efficiency of 75% compares favorably with the literature.

Two-photon quantum polarization interferometry was demonstrated for the first time with an aperiodically poled Ti:LN waveguide source. A sample with a 1%

linear chirp yielded an interferogram fringe visibility of 57%, indicating a low level of entanglement. The SH spectrum of this source was also three times narrower than expected. The quality of these results emphasizes the complexity of fabricating aperiodically poled structures in Ti:LN with high enough quality for frequency entanglement, and motivated the fabrication advancements described above.

An engineered, broadened and smoothed phasematching bandwidth was demonstrated with a chirped and apodized poling profile after optimization of the fabrication techniques. The design broadened the SH phasematch bandwidth by a factor of 8.4 from 0.52nm to 4.4nm, and the measured bandwidth of 4.1nm matches simulation to within 7% of the target width. Further research is needed into the compatibility of NiCr electrodes with Ti:LN waveguides, however, as their use was correlated with poor guidance of long-wavelength TM-like modes.

A new methodology was presented for optimization of a chirped and apodized poling profile for two-photon quantum polarization interferometry. By exploiting even-order dispersion cancellation, it is only necessary to manage odd orders of the spectral phase in order to recover transform-limited performance. This methodology was implemented in simulation and achieved a smooth, high visibility (90.3%) interferogram with 54fs FWHM.

Finally, this work presented a roadmap for future device development and applications. Multiple avenues of investigation were proposed for further improving the poling quality, with zinc waveguides and latent light-assisted poling called out as promising options requiring relatively little modification to the fabrication procedure. Sensing applications of two-photon quantum polarization interferometry were discussed, including polarization mode dispersion measurements and quantum optical coherence tomography. The future of the technologies presented in this dissertation is fully integrated, plug and play devices that bring the power of quantum sensing

outside the confines of the laboratory.

Appendix A

Fabrication instructions

NOTE: this appendix is intended to be a stand-alone reference document, so there is some intentional repetition of information from the body of the dissertation.

A.1 Summary of steps

Step	**Equipment**	**Time (per 10 pcs)**
Dice wafers	Disco DAD 3000	1 hour
Remove tape residue	817 hood (acid)	30 minutes
3-step clean	815 hood (solvent/base)	30 minutes
Deposit titanium	Angstrom e-beam/CHA evaporator	4 hours
3-step clean and dehydrate	Photolithography bench, hard bake oven (120C)	1 hour
Spin on photoresist	Headway spinner	30 minutes
Soft bake	Soft bake oven (80C)	30 minutes
Expose and develop (waveguide mask)	Suss MA6 aligner	1 hour
Hard bake	Hard bake oven (120C)	1 hour
Etch waveguides and remove resist	817 hood (acid)	30 minutes
Diffusion	Tube furnace	9 hours
Grinding*	Grinder and polishing mount	˜40 mins per sample

continued on next page

continued from previous page		
Step	**Equipment**	**Time (per 10 pcs)**
Backpoling (several steps)*	Poling chamber, amplifier, feedback system	˜40 mins per sample
Deposit nichrome	Angstrom DC sputter system	4 hours
Spin on photoresist	Headway spinner	30 minutes
Soft bake	Soft bake oven (90C)	30 minutes
Expose and develop (electrode mask)	Suss MA6 aligner	1 hour
Hard bake	Hard bake oven (120C)	1 hour
Periodic poling (several steps)*	Poling chamber, amplifier, feedback system	˜40 mins per sample
Remove NiCr and photoresist	817 hood	30 mins
Polish end faces	Grinder and polishing mount	˜1 hour per sample

(*) step with elevated risk of breakage

A.2 Materials

The QFC and first SPDC/SH results reported in this dissertation used 40x50mm rectangular congruent LN wafers from Precision Micro Optics. The final apodized samples were fabricated from 3-inch round wafers from Gooch & Housego, part number 97-00567-03. In both cases, the wafers are polished to an optical finish on the z face, left at saw roughness on the +z face, and were 500μm thick. You can substitute other shapes or sizes of wafer, or use other brands, provided the wafers are z-cut, congruent, and polished to an optical finish on the z face. Note that poling voltages, duty cycle homogeneity, and optical damage thresholds vary from supplier to supplier and can even vary from order to order; we switched to Gooch and Hausego after a bad batch from PMO.

The diffused waveguides are made with 100nm thick, 99.995% pure titanium (Kurt J. Lesker part # EVMTI45QXQI).

The photomasks are made from 5x5x0.090 soda lime and low-reflective chrome blanks from Nanofilm, coated with 5300 of AZ1518 photoresist and soft-baked at 90C for 1hr (part number 509SLLRC15185K). Lithography is performed on the LN samples with S1818 positive photoresist, primed with HDMS.

The poling is done in a Plexiglas chamber, with a 1/8 thick, 30A hardness silicone rubber gasket. The dielectric strength, as reported by manufacturer, is 400-700 V/mil (We buy sheets of silicone (McMaster part 9010K13) and have it laser-cut to the desired gasket shape). The electrolyte is a saturated solution of lithium chloride powder in isopropanol.

A.3 Dicing

Due to the small inner diameter of our diffusion furnace, the samples must be diced before diffusion. Weve found it convenient to dice as the very first step, as the dicing process can damage the thin layer of titanium.

We use a DISCO DAD 3000 automatic dicing saw with DISCO blade ZHFX-SD1700-C1-50-CC (1700 grit, 0.64-0.76mm exposure, 0.025-0.030mm kerf). Technical specifications for this blade advertise average chip size when processing LiTaO3 wafers of ¡15um. While it is possible to use a blade intended for silicone dicing, it will result in severe chipping and complicate the polishing procedure. If the DISCO ZHFX-SD1700-C1-50-CC blade is no longer available, look for something recommended for LiTaO3 or LN.

We place the wafers on UV cutting tape with the rough +z side facing up. We dice through 400um of the wafer thickness in 4-5 passes, with 2mm/s feed and 30,000RPM spindle speed. The thickness of the sample+tape is typically 600-650um; the cuts are

at heights of 525, 425, 325, 225, and 125um. Leaving about 100um of the LN intact allows for easy cleaving. Weve found that this produces a cleaner edge than dicing through the entire thickness.

The wafer is diced into 2cmx1cm samples with the long side parallel to the x-axis. The waveguides will be x-propagating.

To remove the samples from the UV dicing tape, they are placed under a UV lamp for 1-2 minutes then gently peel off the tape. During the peeling process, the samples will cleave apart from each other.

A.4 Removal of tape residue

To remove tape residue and any other surface contaminates, the samples undergo a multi-step cleaning process. First, they are soaked for 10 minutes in 9:1 H_2SO_4:H_2O_2 ("piranha solution"). Mixing piranha solution is very exothermic, so we let the mixture cool for about 1 minute before adding the samples.

Note that a 3:1 H_2SO_4:H_2O_2 mixture is the more traditional ratio for piranha solution, but we found that the samples often broke when cleaned with a solution of that ratio, even when it was allowed to cool for 3-5 minutes before adding the samples. We hypothesize that the breakage was due to thermal shock.

After processing with piranha the samples undergo the 3-step cleaning process.

A.5 3-step cleaning process

This cleaning procedure is very important and is repeated multiple times throughout the fabrication process. Rinse the samples with DI water and place in an acetone bath for 5 minutes. This is followed by 5 minutes in an isopropanol bath, then 5 minutes in DI water. Finally, the samples are thoroughly dried with a nitrogen gun. Use the ultrasonic cleaner for the first iteration of this process after

tape adhesive removal. Do *not* use the ultrasonic cleaner at later iterations, as it can peel off the titanium or NiCr stripes.

A.6 Titanium deposition

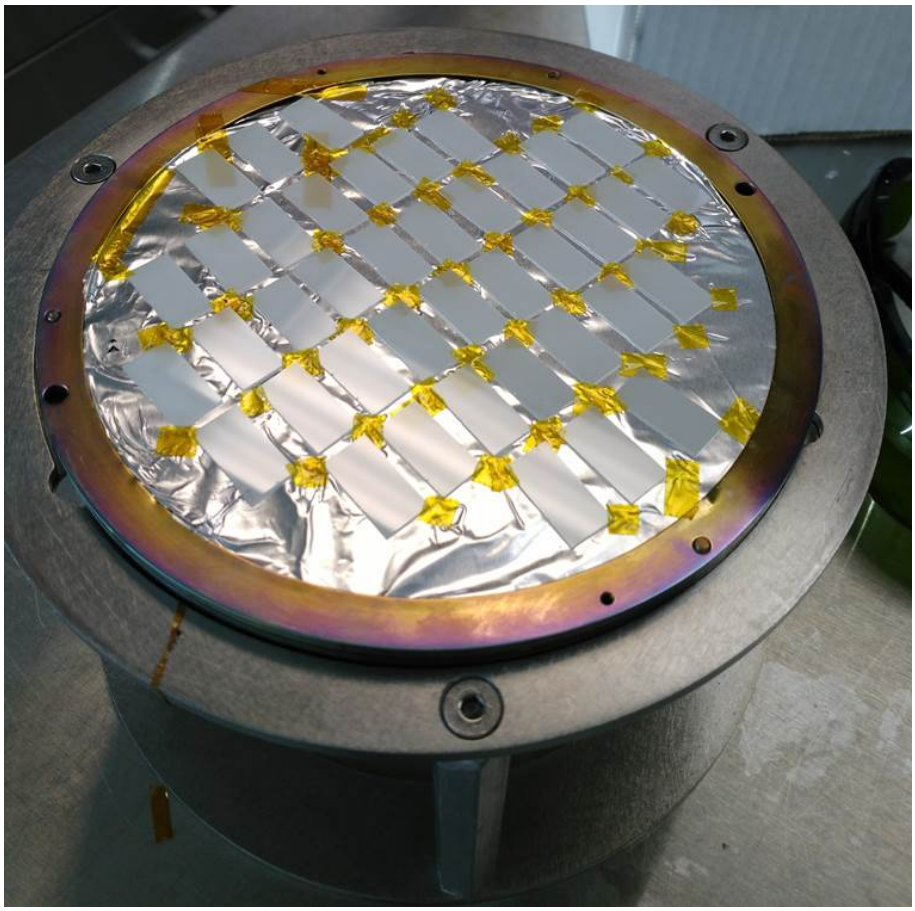

Figure A·1: Photograph of clean samples taped to the electron beam sample mount, in preparation for titanium deposition. This is a double batch.

Immediately after cleaning, mount the samples to a foil-covered e-beam evaporator sample holder with kapton tape as shown in Fig. A·1. We make sure not to cover more than 2mm of each edge of the sample with tape, since the center 6x16mm region will be periodically poled and we wish to fill it as much as possible with waveguides.

We also make sure not to cover the short edges with tape, as the x-propagating Ti-diffused waveguides need to go all the way to the edge of the sample. Alternately, one may tape the corners only to cover less of the surface area of each sample. The titanium for the diffused waveguides is deposited in an e-beam evaporator. One of two systems may be used - procedures for both are detailed below. Both use a crystal monitor to measure the thickness of the deposited material, but tend to overshoot the desired thickness. Regardless of the system used, measure the titanium thickness after deposition with the Tencor instruments Alpha-Step 500 surface profiler.

A.6.1 Using the Angstrom system:

After loading the samples, the chamber should be pumped down to at the most 10^{-7} torr for deposition to occur. A recipe for the Angstrom system is saved in the computer; the key parameters are the final thickness of 90nm, peak power of 40%, and deposition rate of 0.5Å/s. We target 90nm as the system tends to overshoot slightly. When deposition is complete, allow the samples some time to cool while the chamber is vented.

A.6.2 Using the CHA system:

In the event the Angstrom system is out of service we also have access to a CHA Solution e-beam system. Weve found that programming in 90nm thickness results in the desired 100nm thickness. Deposition is done at 0.1Å/s, and the soak power is set to 15%. After deposition, the samples are allowed to cool for 15 minutes before venting the chamber.

A.7 Lithography: Waveguides

When doing lithography, always wear a face mask! LN is pyroelectric, and its inherent static charge will attract dust and debris from your

mouth and face. Also wear a beard net, if applicable.

After titanium deposition, the waveguides are lithographically defined on the samples. We begin by cleaning the samples again (in the Class 100 lithography room), and then dehydrating the samples for 30min in a 120C oven. The samples are then individually coated with S1818 photoresist (*NB*: formerly used HDMS primer but found that it reacted strangely during periodic poling) in a Headway spinner. The spinning recipe is as follows, and results in a 2.2μm thick layer of resist:

- Turn on spinner vacuum using the switch near the back of the machine
- Program in the following spin recipe: ramp at 100rpm/s to 500rpm, hold 1s, ramp at 500rpm/s to 2000rpm, hold 30s, ramp down at 100rpm/s (This is recipe #8 on the BU spinner).
- Place sample on the chuck (one of the smaller ones works),
- Use eyedropper to completely cover sample surface with S1818 photoresist. The surface tension of the resist will cause it to look like a lozenge on top of the sample. Make sure the resist goes completely to the edges and corners, and gently suck up any bubbles with the pipette. Try to prevent the resist from spilling over the edges of the sample, as any that gets on the back will need to be removed later.
- Spin with the above recipe.

Due to the small size and rectangular shape of the samples it is crucial to remove photoresist at the edges where it beads up on the sample, as it can disturb proper mask alignment. To remove edge beads, the wooden shaft of a cotton-tip applicator can be used to hold the sample along one edge while the end of another one (or the same one broken in two) can be used to gently wipe the resist off the outer $\approx$ 1mm of the sample.

The samples are then soft-baked in a 90C oven for 30min. We place the samples in a makeshift tray made from aluminum foil and place a foil "lid on top to prevent dust from settling on the fresh resist. Take care that the lid does not touch the samples, as it will smudge the photoresist.

After soft-bake, the samples are exposed in a Karl Sss MA6 mask aligner. For S1818 spun with the above recipe, we use hard contact and expose for 15s at 10mW (channel 1) on the lamp power supply (*N.B.*: As the lamp ages, this value can change. Always do a test run on a scrap piece if you haven't done lithography in a while). We are fortunate enough to have a Heidelberg Instruments DWL 66 mask writer in house, so we design and write the own photomasks. If the samples stick to the mask or the mask begins to look dirty, remove it from the MA6 and gently clean with acetone.

Following exposure, the samples are developed for 60s in MF-319 developer while gently agitating. The sample is immediately rinsed in DI water, then blow-dried with nitrogen. Inspect the sample to make sure it turned out well; if not, strip the resist with acetone, follow the 3-step cleaning procedure, and start again at the first lithography step (dehydrating the sample).

If the lithography looks good, hard bake for 30min at 120C. Note that the hard bake oven may be set to 180C by other users, which can permanently bake the photoresist onto the samples. Take care that temperature is properly set. *N.B.*: The dehydration, soft bake, and hard bake can all potentially cause small spots of spontaneous local domain inversion! LN is pyroelectric, and temperature changes cause a buildup of charge on the surface. This can be enough to cause local poling or even fracture the sample, particularly if the temperature change is abrupt. This motivates the use of ovens, instead of hot plates.

After hard baking, etch the titanium in 20:1:1 H_2O:HF: H_2O_2 (Etch rates given in (Williams et al., 2003). This typically takes about 30s. The rule of thumb is wait

for the sample to go clear, then wait 5 more seconds and rinse in DI water. Inspect under the microscope, then remove remaining resist by soaking the samples in an 80-100C bath of Shipley 1165 remover for 10 minutes to an hour. Longer soaks and temperatures of up to 120C may be required for especially stubborn photoresist.

Once the sample is completely free of photoresist, repeat the cleaning process, and thoroughly dry the samples with the nitrogen gun. At this point, it is wise to double-check the dimensions of the titanium stripes with the surface profiler! Discrepancies in the Ti thickness will not only degrade the optical confinement in the waveguide, but also change the effective index and shift the degeneracy point for the nonlinear processes.

A.8 Diffusion

The samples are diffused in a quartz tube furnace. Following the procedure used at University of Paderborn (per Abu Thomas), the diffusion occurs in 3 stages as described in Table 1.

	Temperature	Time	Gas
Ramp up	Room temperature to 1060C	1 hr	2000sccm argon, bubbled through 90C H2O
Soak	1060C	7 hrs	2000sccm argon, bubbled through 90C H2O
Ramp down	1060C to room temperature	1 hr	100sccm oxygen, bubbled through 90C H2O

Table A.1: Diffusion procedure

The diffusion apparatus contains the following elements: furnace, quartz process tube, quartz boat, tube-to-vacuum interconnects, input and output bubbler systems, and the gas flow systems. The setup is shown in Fig. A·2.

Argon and oxygen tanks are connected to mass flow controllers, and the gas is

selected with a manual switch. The gas picks up water vapor by flowing through a warm (90C) bubbler filled with DI water, then flows into the quartz process tube. The bubbler sits in a dish full of water atop the hot plate to improve heat transfer. The gas flows over the sample and exits the system through a second bubbler filled with mineral oil, which acts as a one-way valve to prevent other gases from backing up into the furnace. The gases vent to the fume hood.

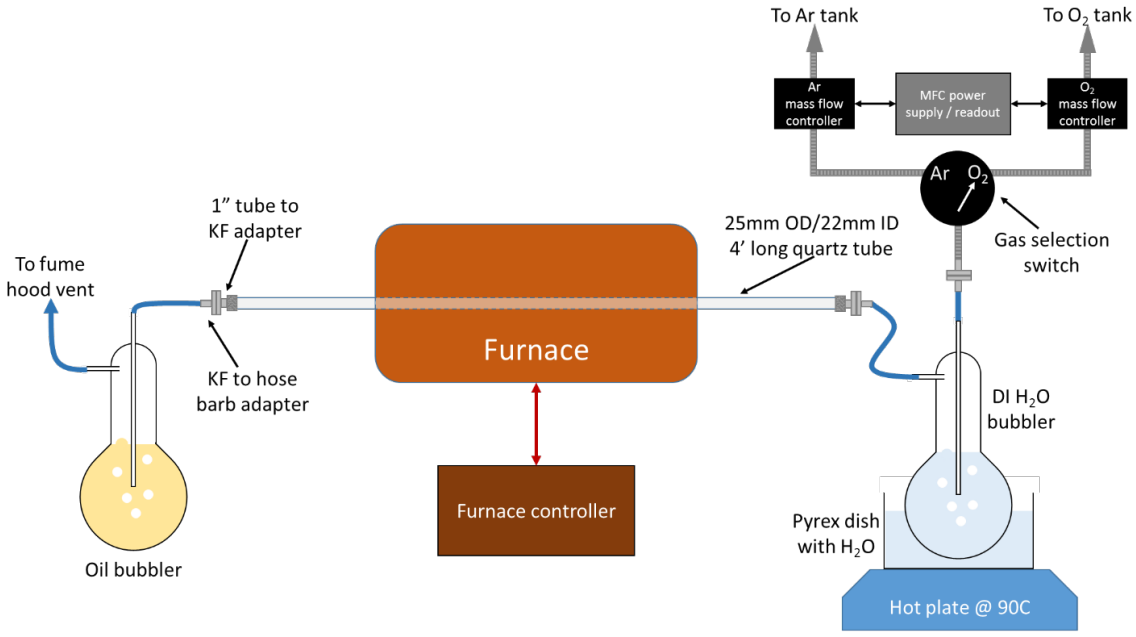

Figure A·2: Titanium diffusion setup.

Inside the quartz tube, the samples sit on a quartz holder, or boat. The boat has a loop in one end to allow for easy retrieval of the samples with a hooked push/pull rod. The boat and rod are also ordered from G. Finkenbeiner. Care must be taken to arrange the samples in the center of the furnace, and to avoid temperature gradients greater than 1-2C. The furnace has a large flat temperature region in the center, and we have successfully diffused up to ten 2cmx1cm samples at a time.

After diffusion, inspect the samples under the microscope and with the surface

profiler due to presence of water vapor in the tube furnace. It is normal for the samples to turn slightly yellow during diffusion. The waveguides typically have light speckling on the surface, as shown in Fig. A·3. The surface profiler shows 100nm swelling of the waveguides from the distortion of the material caused by diffusion.

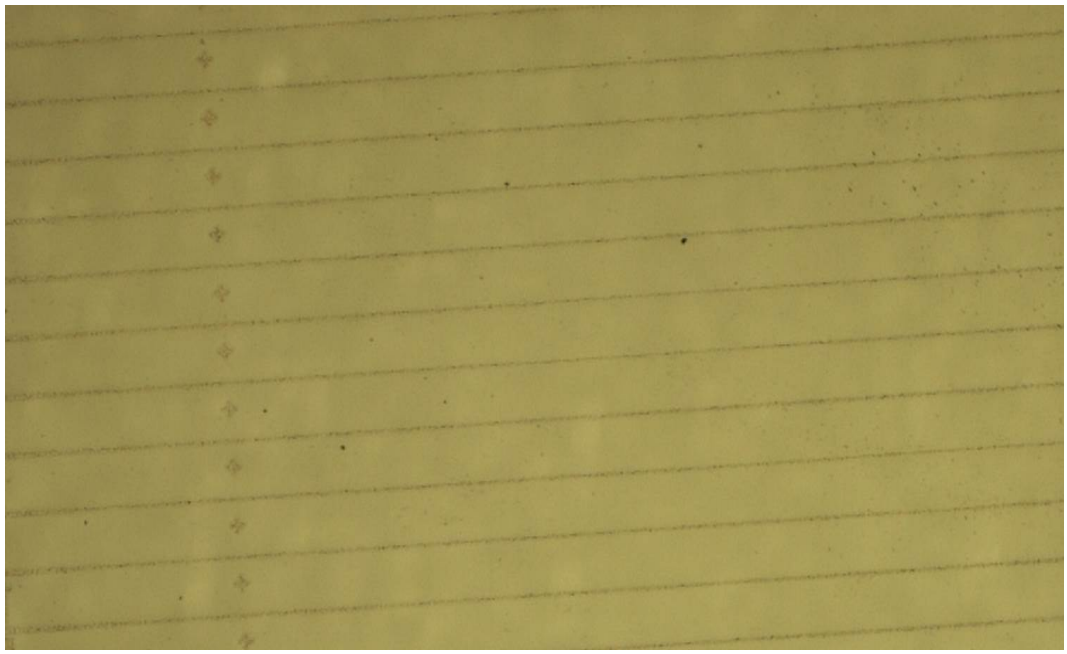

Figure A·3: Photograph of Ti:LN waveguides after diffusion. The speckles on the top surface are normal, and are presumed to be due to lithium oxide out diffusion.

A.9 Grinding and back-poling

Domains nucleate on the +z face of lithium niobate. Due to its pyroelectric properties, the diffusion process creates a ˜50um thick layer of poling "noise" on the +z face. This must be removed to allow proper poling to take place. This is done downstairs in B14 at the South Bay Technology polishing station. The backgrinding recipe is as follows:

- Prepare the chemical-mechanical polishing slurry by dilluting approximately 1

Figure A·4: Mount used for grinding the back face of the sample after titanium diffusion.

capful of South Bay Technologies colloidal silica polishing slurry (SBT CS1-16) in 1 liter of DI water.

- Gently place the sample in the polishing mount with the waveguides (smooth -z face) facing inward, so that the rough +z face ends up in contact with the polishing pad.
- Place the 6μm polishing pad on the rotating mount, holding it in place with the adhesion of a few drops of the water/silica mixture
- Place the polishing mount on the pad, hold it in place with the bracket, and place a 100g weight on top.
- Polish for 30 minutes at speed 2
- Repeat with the 1μm pad for 15 minutes

After grinding, the +z face should be smooth and the sample should be transparent.

The sample must then be "backpoled" to invert the bulk of the sample so that the waveguides are on the +z face. This will allow for clean domain nucleating when we do the periodic poling. The poling procedure is presented in detail below. ***Gloves must be worn at all times.***

Cleaning the chamber and gaskets:

- Set up a bucket with DI water and some dish soap, this will be critical for removing the emulsified mixture of mineral oil and electrolyte from the chamber.
- Immerse the chamber in the wash bucket and clean off any visible residue by hand. A soak of 5-10 minutes helps, but vigorous agitation and scrubbing is always required for complete cleanliness.
- Rinse off the chamber in DI water, then wash in a dish of isopropanol to remove any remaining electrolyte residue. Use a cotton bud with isopropanol to remove gasket residue which may be present.
- Before every poling run new gaskets are required. The laser cutting process leaves a soot-like residue on the gaskets, which can be removed by aggressively scrubbing with mineral oil. Then use dish soap and DI water to remove the mineral oil, and finally clean and rinse with isopropanol and DI water to remove soap residue.

Loading the sample:

- Apply mineral oil to each gaskets, they should be covered evenly on all sides with visible beading
- Place the gaskets in each side of the poling chamber, with the flatter side facing out. Use a finger to coat the oil evenly around the gaskets where they meet the chamber, taking care to make sure oil does not pool in the chamber

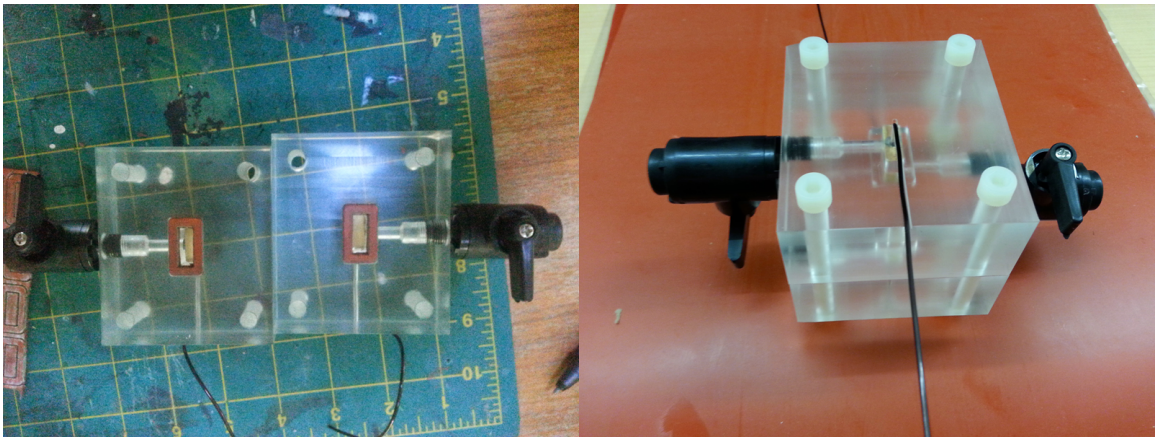

Figure A·5: Left: the halves of the poling chamber, with gaskets. Right: the assembled poling chamber.

- Identify the half of the poling chamber marked with a +. The +z face of the sample must face this mark. Holding that half of the chamber in your hand, carefully place the sample +z face down on the gasket using clean tweezers. Take care to center the sample on the gasket.

- Put the 4" steel screws through the mounting holes and carefully lower the other half of the chamber (with its gasket) on top of the sample.

- Put nuts on the screws and tighten by hand, then use a wrench to snug them up. Take care not to over-tighten; this will break the sample.

- Open the valves and, using a pipette,fill each side of the chamber with a saturated solution of LiCl in isopropanol The solution must be prepared in advance, as follows: Take a clean laboratory bottle with a screw cap and add isopropanol. Add lithium chloride powder and shake to dissolve. If it all dissolves, add more and repeat. Keep adding and shaking until there is a distinct layer of LiCl at the bottom of the bottle that will not dissolve. Let sit for at least 30min so any suspended particles can settle. When pipetting solution from the bottle, take

care not to disturb the LiCl layer, taking care to shake out any bubbles that are in the chamber.

- Inspect the outside of the poling chamber. Rinse with DI water and blow dry if any electrolyte solution dripped out while you were filling it.
- Carry the loaded poling chamber over to the poling station and place on top of a piece of glass, on top of a sheet of silicone. This insulation is to protect you and the table!
- Use a multimeter to check the resistance between the terminals of the chamber. The resistance across lithium niobate at low voltages should be essentially infinite; if you see anything other than OVLD, there is a leak and the chamber must be emptied, cleaned, and reloaded.

Performing poling:

- Connect the positive (white) cable from the amplifier to the + side of the chamber, and the ground (black) side to the unmarked side.
- New as of June 2016: Connect the Zedboard FPGA and Maxim MAXREFDES71 analog front end to the computer via USB to micro USB cables. Connect the Zedboard to its power supply, and connect a lab power supply set to 24V to the power supply connections on the MAXREFDES71# using grabber clips.
- Open TeraTerm. Select the appropriate serial port (usually COM3 but may vary) and set the baud rate to 115200. Do not change any of the other parameters. If the COM port does not show up, turn on the Zedboard and try again.
- Cycle power on the Zedboard once. The lights on the board will flash, and a user prompt will appear in the terminal. The code will request verification of

the DAC output. If it is within +/-50mV of 0V, you may proceed. Otherwise, connect the DAC to the amplifier via the labeled connections on the breakout box. The amplifier input goes to VOUT1 anSd GND, and the measurement output goes to V1+ and V1- (differential measurement).

- Turn on and enable the Trek 20/20 high voltage amplifier
- Press the spacebar to run the poling sequence. Be sure to take standard high voltage precautions. Watch the chamber during poling. If you see a pink arc, hear a hiss, or see any electrolyte forced out of the closed valves, this is a sign that the sample broke down during poling.
- Turn off the amplifier and Zedboard, disconnect the poling chamber, and empty the electrolyte solution into an appropriate hazardous waste container.
- Repeat the cleaning and drying process on the chamber, and rinse the sample in DI water then gently blow dry.
- Check the monitor output file from the poling code in MATLAB.

A.10 Nichrome deposition

A layer of nichrome is then deposited via RF sputtering to form electrodes. The Angstrom system may also be used for RF sputtering in addition to E-beam deposition. The nichrome sputtering target is property of our group (order from Kurt Lesker, part number EJTNICR303A2). Sputtering is performed in a 5mTorr argon atmosphere at 320V and 250mA for 1500 seconds to produce an $\approx$ 100nm film. RF sputtering is a time-power process without direct measurement, but gives repeatable results for thickness.

A.11 Lithography: periodic poling

The samples are then brought back up to the cleanroom, and cleaned, dried, primed, and spun as in the waveguide lithography. Before soft baking, edge bead removal must once again be performed (see the waveguide lithography section).

The electrode pattern is then exposed on the sample using the MA6 mask aligner with hard contact and 15s exposure. Develop as normal, for 60s in MF319 developer.

If the lithography looks good, hard bake for 12 hours at 120C. If it looks bad, strip the resist with acetone, clean the samples following the usual procedure, and try again.

Next, the electrodes are etched with chromium etchant (of the same variety used for photomasks). This process takes about 30 seconds per sample. Once this is done the photoresist can be removed with Shipley 1165 Remover as usual. Perform the cleaning process again to prepare for the final round of lithography.

The poling lithography is conducted as above, producing a layer of insulating photoresist with small windows for the electrodes. The only difference for this step is that the samples are baked much longer because we need to ensure the resist will not dissolve in the electrolyte solution during poling. ***If there is any photoresist residue on the back side of the sample, clean it off very carefully with a cotton bud and acetone before hard baking!*** An overnight bake of approximately 12 hours works well. Baking more than 24 hours is NOT recommended, as the resist may burn permanently onto the sample and become difficult or impossible to remove.

A.12 Periodic poling

Periodic poling is done in the same way as backpoling, except the target charge accumulation is set to 18uC (As with the backpoling, this is about 1.5x larger than

the calculated value for this mask + gasket combination (12uC)). Take care when loading the sample into the poling chamber after backpoling, the side with the waveguides is now +z and should face the + mark on the chamber.

To confirm successful poling, take the samples back to the cleanroom and carefully deposit 1-2 drops of HF on the z face (the side without waveguides) using a HF-resistant dropper or spoon. DO NOT GET ANY HF ON THE WAVEGUIDES. Let sit for 15min, then rinse and dry. Inspect under the microscope. Periodic domains should be clearly visible. Some merging of domains on the backside is ok.

After successful periodic poling, strip the resist at 120C in the Shipley 1165 Remover, 3-step clean the samples, place each sample in its own foil pouch, and anneal in the oven in B15 for 12 hours at 325C, with a temperature ramp up/down rate of 10C/min.

A.13 End-face polishing

Polishing is done similarly to grinding, but with the sample mounted vertically in our custom end-face polishing mount. This mount uses a friction fit, so do not use adhesive. Metal shims are inserted into the mount to adjust how much of the sample protrudes for polishing. Place the sample in the mount so that the waveguides are facing the soft orange rubber pad.

Begin by selecting a shim that will leave 2mm of the sample protruding, and polish at speed 1 on the 30um (green) pad until at least 1mm of material is removed. This is necessary because the waveguides

Next, switch to the 6um (red) pad and wet with a few drops of water and a few drops of South Bay Technologies alkaline polishing solution. This softens up the lithium niobate and reduces chipping. Polish on speed 1 until the surface quality no longer improves (check periodically under the microscope; do not remove the sample

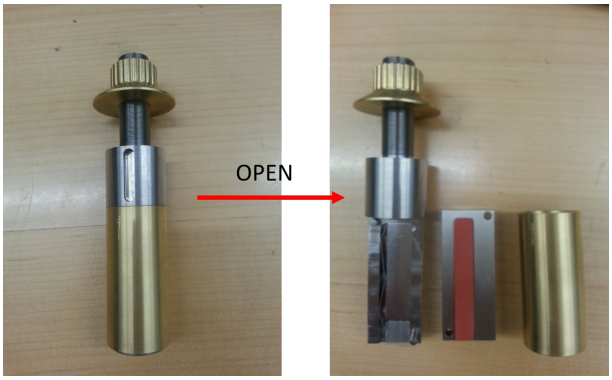

Figure A·6: Mount used for end-face polishing.

from the mount, but do rinse the sample end-face with DI water and gently clean with isopropanol and a lens tissue before inspecting).

Repeat with the 3um, 1um, and final polishing pads. Ideally, the end face should be free of scratches and there should not be any chipping along the edge with the waveguides (closest to the orange pad).

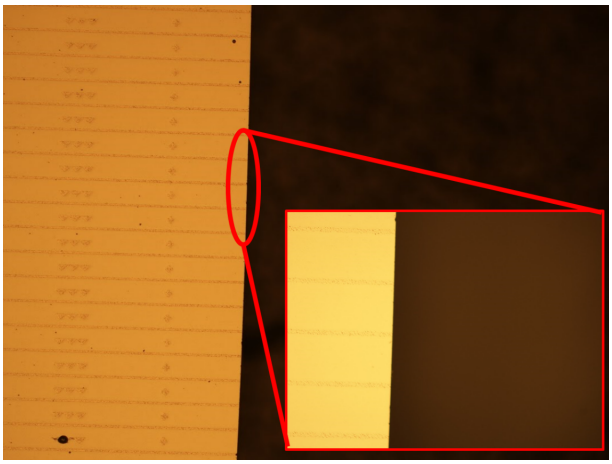

Figure A·7: Microscope image of a polished waveguide end-face

Remove the sample from the mount, move up to the next length of shim, and re-insert the sample with the other end facing out. Repeat on the second face.

After polishing, remove the sample from the mount, rinse with DI water, and gently clean all surface with isopropanol and a lens tissue. After installing the sample in

the experiment, carefully clean the end-faces again with a lens tissue held in tweezers, taking care not to knock the sample out of the holder.

Appendix B

Relationship between SPDC and SH bandwidths

Recall that the two-photon probibility amplitude for SPDC with perfect phase matching or uniform periodic poling (QPM) is

$$\tilde{\chi}^{(2)}\left(\omega_S, \omega_P - \omega_S\right) = \operatorname{sinc}\left(\Delta k L/2\right) e^{-i\Delta k L/2}. \tag{B.1}$$

Consider the wavevector $k\left(\omega\right) = n\omega/c$ and let $\omega = \omega_0 + \Omega$, and Taylor expand it to first order about $\Omega = 0$. This yields

$$k\left(\omega_0 + \Omega\right) \approxeq k\left(\omega_0\right) + \Omega \left.\frac{\partial k\left(\omega_0 + \Omega\right)}{\partial_\Omega}\right|_{\Omega=0} = k\left(\omega_0\right) + \frac{\Omega}{v_g\left(\omega_0\right)}, \tag{B.2}$$

where $v_g\left(\omega_0\right)$ is the group velocity at ω_0.

The spectral intensity of the down-converted photons $I\left(\omega_S, \omega_P - \omega_S\right)$ is proportional to $\operatorname{sinc}^2\left(\Delta k L/2\right)$. Using the approximation above, the argument $\Delta k L/2$ can be re-written as

$$\frac{\Delta k L}{2} \approxeq \frac{1}{2}\left[\Delta k\left(\omega_0\right) L + \frac{\Omega L}{\Delta v_g\left(\omega_0\right)}\right] = \frac{1}{2}\left[\Delta k\left(\omega_0\right) L + \Omega \Delta\tau\right], \tag{B.3}$$

where $\Delta\tau = \frac{L}{v_g^o(\omega_0)} - \frac{L}{v_g^e(\omega_0)}$ is the time delay between the degenerate ordinary and extraordinary polarized SPDC photons at frequency ω_0 when they exit the crystal.

B.1 SPDC bandwidth

SPDC bandwidth is measured in terms of the down-converted photon wavelength, so let $\omega_S = \omega_0 + \Omega$, $\omega_I = \omega_0 - \Omega$, and $\omega_P = 2\omega_0$.

Thus for Type-II SPDC,

$$\Delta k_{SPDC}(\Omega) = k_P^o(2\omega_0) - k_S^o(\omega_0 + \Omega) - k_S^e(\omega_0 - \Omega) \tag{B.4}$$

$$\frac{\Delta k_{SPDC} L}{2} \approxeq \frac{L}{2}\left[k_P^o(2\omega_0) - k_S^o(\omega_0) - k_S^e(\omega_0 \Delta\tau)\right] + \frac{\Omega\Delta\tau}{2}, \tag{B.5}$$

where o, e superscripts denote ordinary and extraordinary polarization.

Dropping the constant terms, $\frac{\Delta k_{SPDC} L}{2} \propto \frac{\Omega\Delta\tau}{2}$. The FWHM of a general $\mathrm{sinc}^2(\alpha x)$ function is $\approxeq \frac{2.7831}{\alpha}$, so for SPDC we have $FWHM = \frac{1.39155}{\Delta\tau}$.

B.2 SH bandwidth

SH is a stimulated process, so to see the entire phase-matching bandwidth it is necessary to sweep the *fundamental*. Consider the case where $\omega_F = \omega_0 + \Omega$:

$$\Delta k_{SH}(\Omega) = k_F^o(\omega_0 + \Omega) + k_F^e(\omega_0 + \Omega) - k_{SH}^o(2\omega_0 + 2\Omega) \tag{B.6}$$

$$\frac{\Delta k_{SH} L}{2} \approxeq \frac{L}{2}\left[k_F^o(\omega_0 + \Omega) + k_F^e(\omega_0 + \Omega) - k_{SH}^o(2\omega_0 + 2\Omega)\right] + \frac{\Omega\Delta\tau_{SH}}{2}, \tag{B.7}$$

where $\Delta\tau_{SH} = \tau^o(\omega_0) + \tau^e(\omega_0) - 2\tau^e(2\omega_0)$ differs from the SPDC $\Delta\tau$ due to the active sweeping of the input wavelength.

Dropping the constant terms, $\frac{\Delta k_{SH} L}{2} \propto \frac{\Omega\Delta\tau_{SH}}{2}$. The FWHM of a general $\mathrm{sinc}^2(\alpha x)$ function is $\approxeq \frac{2.7831}{\alpha}$, so for SPDC we have $FWHM = \frac{1.39155}{\Delta\tau_{SH}}$.

B.3 SPDC/SH bandwdth ratio

The ratio of the FWHMs is $\left.\frac{FWHM_{SPDC}}{FWHM_{SH}}\right|_{\omega_0} = \frac{\tau^o(\omega_0)+\tau^e(\omega_0)-2*\tau^e(2\omega_0)}{/}\tau^o\left(\omega_0\right) - \tau^e\left(\omega_0\right)$, where ω_0 is both the fundamental (input) frequency of the SH and the down conversion (output) frequency of the SPDC.

In terms of the group index $n_g = \frac{c}{v_g} = \frac{c\tau}{L}$, which can be looked up for bulk LN (see, e.g., refractiveindex.info),

$$\left.\frac{FWHM_{SPDC}}{FWHM_{SH}}\right|_{\omega_0=1560nm} = \frac{n_g^o\left(\omega_0\right) + n_g^e\left(\omega_0\right) - 2 * n_g^e\left(2\omega_0\right)}{n_g^o\left(\omega_0\right) - n_g^e\left(\omega_0\right)} = 3.54 \tag{B.8}$$

References

Abernethy, J. A. (2002). *Novel devices in perodically poled lithium niobate*. PhD thesis, University of Southampton.

Abouraddy, A. F., Nasr, M. B., Saleh, B. E. A., Sergienko, A. V., and Teich, M. C. (2002). Quantum-optical coherence tomography with dispersion cancellation. *Physical Review A*, 65(5):053817.

Amin, J., Pruneri, V., Hanna, D. C., and Wilkinson, J. S. (1997). Blue light generation in a periodically poled Ti:LiNbO3 channel waveguide. *Optics Communications*, 135:41–44.

Arahira, S., Kishimoto, T., and Murai, H. (2012). 1.5um band polarization entangled photon-pair source with variable Bell states. *Optics Express*, 20(9):9862–9875.

Arfken, G. and Weber, H. J. (2005). *Mathematical Methods for Physicists*, volume 19852. Elsevier Academic Press, sixth edition.

Atikian, H. A., Eftekharian, A., Jafari Salim, A., Burek, M. J., Choy, J. T., Hamed Majedi, A., and Lončar, M. (2014). Superconducting nanowire single photon detector on diamond. *Applied Physics Letters*, 104(12).

Ballato, J. and Gupta, M. C., editors (2006). *The Handbook of Photonics*. CRC Press.

Batchko, R. G., Miller, G. D., Shur, V. Y., Rumyantsev, E. L., Fejer, M. M., and Byer, R. L. (1999). Domain patterning in lithium niobate using spontaneous backswitching. In *Proceedings of SPIE Conference on Laser Material Crystal Growth and Nonlinear Materials and Devices*, volume 3610, pages 36–43.

Boes, A. S. (2016). *Laser light induced domain engineering of lithium niobate for photonic and phononic applications*. PhD thesis, Royal Melbourne Institute of Technology.

Bortz, M. L., Fujimura, M., and Fejer, M. M. (1994). Increased acceptance bandwidth for quasi-phasematched second harmonic generation in LiNbOe waveguides. *Electronics Letters*, 30(1):34–35.

Boyd, R. W. (2008). *Nonlinear Optics*. Academic Press, third edition.

Burghoff, J., Nolte, S., and Tünnermann, A. (2007). Origins of waveguiding in femtosecond laser-structured LiNbO3. *Applied Physics A*, 89(1):127–132.

Chang, L., Li, Y., Volet, N., Wang, L., Peters, J., and Bowers, J. (2016). Thin film wavelength converters for photonic integrated circuits. *Optica*, 3(5):531–535.

Chen, X., Karpinski, P., Shvedov, V., Hnatovsky, C., Boes, A., Mitchell, A., and Krolikowski, W. (2016). Ferroelectric domain engineering using infrared femtosecond laser and its application to optical frequency conversion. In *Photonics Fiber Technology Congress*.

Dauler, E., Jaeger, G., Muller, A., and Migdall, A. (2000). Tests of a Two-Photon Technique for Measuring Polarization Mode Dispersion With Subfemtosecond Precision. *Journal of Research of the National Institute of Standards and Technology*, 104(1):1–10.

Fernandez-Gonzalvo, X., Corrielli, G., Albrecht, B., Grimau, M. L., Cristiani, M., and de Riedmatten, H. (2013). Quantum frequency conversion of quantum memory compatible photons to telecommunication wavelengths. *Optics Express*, 21(2008):19473–87.

Fontaine, M., Delâge, A., and Landheer, D. (1986). Modeling of titanium diffusion into LiNbO3 using a depth-dependent diffusion coefficient. *Journal of Applied Physics*, 60(7):2343–2350.

Fraine, A., Minaeva, O., Simon, D., Egorov, R., and Sergienko, A. V. (2012). Evaluation of polarization mode dispersion in a telecommunication wavelength selective switch using quantum interferometry. *Optics Express*, 20(3):2025–2033.

Fraine, A. M. (2015). *Engineering photonic entanglement and its practical applications*. Phd thesis, Boston University.

Fukuma, M. and Noda, J. (1980). Optical properties of titanium-diffused LiNbO3 strip waveguides and their coupling-to-a-fiber characteristics. *Applied Optics*, 19(4):591–597.

Giovannetti, V., Lloyd, S., and MacCone, L. (2006). Quantum metrology. *Physical Review Letters*, 96(1):13–16.

Gui, L. (2010). *Periodically Poled Ridge Waveguides and Photonic Wires in LiNbO 3 for Efficient Nonlinear Interactions*. PhD thesis, University of Paderborn.

Hartung, H., Kley, E.-B., Tünnermann, A., Gischkat, T., Schrempel, F., and Wesch, W. (2008). Fabrication of ridge waveguides in zinc-substituted lithium niobate by means of ion-beam enhanced etching. *Optics letters*, 33(20):2320–2.

Herrmann, H., Yang, X., Thomas, A., Poppe, A., Sohler, W., and Silberhorn, C. (2013). Post-selection free , integrated optical source of non-degenerate , polarization entangled photon pairs. *Optics Express*, 21(23):27981–27991.

Hickman, G. T. (2017). *Nonlinear optics at ultralow power using metastable xenon in a high finesse cavity*. PhD thesis, University of Maryland, Baltimore County.

Hofmann, D., Schreiber, G., Haase, C., Herrmann, H., Grundk, W., Ricken, R., and Sohler, W. (1999). Quasi-phase-matched difference-frequency generation in periodically poled Ti:LiNbO 3 channel waveguides. *Optics Letters*, 24(13):896–898.

HOLOEYE Photonics (2017a). GAEA 10 Megapixel Phase Only Spatial Light Modulator.

HOLOEYE Photonics (2017b). Spatial Light Modulator Principles.

Hong, C., Ou, Z., and Mandel, L. (1987). Measurement of subpicosecond time intervals between two photons by interference. *Physical Review Letters*, 59(18):2044–2046.

Hu, H., Ricken, R., Sohler, W., and Wehrspohn, R. B. (2007). Lithium niobate ridge waveguides fabricated by wet etching. *IEEE Photonics Technology Letters*, 19(6):417–419.

Jackel, J. L., Rice, C. E., Veselka, J. J., Rice, J. L. J. C. E., and Veselka, J. J. (1982). Proton exchange for highindex waveguides in LiNbO3. *Applied Physics Letters*, 607(1982):42–44.

Jaeger, G., Horne, M. A., and Shimony, A. (1993). Complementarity of one-particle and two-particle interference. *Physical Review A*, 48(2):1023–1027.

Janner, D., Tulli, D., Belmonte, M., and Pruneri, V. (2007). Microengineered integrated electrooptic modulators in LiNbO3. *AIP Conference Proceedings*, 992:254–259.

Janner, D., Tulli, D., Lucchi, F., Vergani, P., Guirgola, S., and Puneri, V. (2008). Grinding free electric-field poling of Ti indiffused z -cut LiNbO 3 wafer with submicron. *Applied Physics A*, 91:319–321.

Jin, H., Liu, F. M., Xu, P., Xia, J. L., Zhong, M. L., Yuan, Y., Zhou, J. W., Gong, Y. X., Wang, W., and Zhu, S. N. (2014). On-chip generation and manipulation of entangled photons based on reconfigurable lithium-niobate waveguide circuits. *Physical Review Letters*, 113(10):1–5.

Kahl, O., Ferrari, S., Kovalyuk, V., Goltsman, G. N., Korneev, A., and Pernice, W. H. P. (2015). Waveguide integrated superconducting single-photon detectors with high internal quantum efficiency at telecom wavelengths. *Nature Scientific Reports*, 5(February):10941.

Kielpinski, D., Meyer, V., Rowe, M. A., Sackett, C. A., Itano, W. M., Monroe, C., and Wineland, D. J. (2001). A decoherence-free quantum memory using trapped ions. *Science (New York, N.Y.)*, 291(5506):1013–1015.

Kim, S., Gopalan, V., and Gruverman, A. (2002). Coercive fields in ferroelectrics: A case study in lithium niobate and lithium tantalate. *Applied Physics Letters*, 80(15):2740–2742.

Klyshko, D. N., Penin, A. N., and Polkovnikov, B. F. (1970). Parametric luminescence and light scattering by polaritons. *Journal of Experimental and Theoretical Physics Letters*, 11(1):5–7.

Koetitz, G. (1990). Properties of lithium niobate. *Crystal Research and Technology*, 25(6):720–720.

Kokhanchik, L. S., Borodin, M. V., Burimov, N. I., Shandarov, S. M., Shcherbina, V. V., and Volk, T. R. (2012). Surface Periodic Domain Structures for Waveguide Applications. *IEEE Transactions on Ultrasonics, Ferroelectrics, and Frequency Control*, 59(6):1076–1084.

Krapick, S., Brecht, B., Herrmann, H., Quiring, V., and Silberhorn, C. (2016). On-chip generation of photon-triplet states. *Optics Express*, 24(3):2836–2849.

Kumar, P. (1990). Quantum frequency conversion. *Optics Letters*, 15(24):1476.

Kuo, P. S., Pelc, J. S., Slattery, O., Kim, Y.-S., Fejer, M. M., and Tang, X. (2013). Reducing noise in single-photon-level frequency conversion. *Optics Letters*, 38(8):1310.

Kwon, S., Yang, W., Lee, H., Kim, W., Lee, H., Yoon, D., Song, Y., and JOURNAL (2006). Investigation of domain wall velocity to external fields for high-quality waveguide-type periodically poled LiNbO3 fabrication. *Journal of Rare Earths*, 24:131–135.

Langrock, C., Fejer, M. M., Hartl, I., and Fermann, M. E. (2007). Generation of octave-spanning spectra inside reverse-photon-exchanged periodically poled lithium niobate waveguides. *Optics letters*, 32(17):2478–2480.

Lee, Y. L., Suche, H., Min, Y. H., Lee, J. H., Grundkötter, W., Quiring, V., and Sohler, W. (2003). Wavelength- and Time-Selective All-Optical Channel Dropping in Periodically Poled Ti:LiNbO 3 Channel Waveguides. *IEEE Photonics Technology Letters*, 15(7):978–980.

Manzo, M., Laurell, F., Pasiskevicius, V., and Gallo, K. (2013). Lithium Niobate: The Silicon of Photonics! In Di Bartolo, B., Collins, J., and Silvestri, L., editors, *Nano-optics for enhancing light-matter interactions on a molecular scale*, page 421. Springer.

Meadowlark Optics (2017). Polarization Independent SLM - Custom Capabilities.

Miller, G. D. (1998). *Periodically poled lithium niobate: modeling, fabrication, and nonlinear-optical performance*. PhD thesis, Stanford University.

Miller, G. D., Batchko, R. G., Fejer, M. M., and Byer, R. L. (1996). Visible quasi-phase-matched harmonic generation by electric-field-poled lithium niobate. *Proceedings of SPIE*, 2700:34–45.

Ming, L. (2005). *Fabrication and applications of zinc indiffused channel waveguides in periodically poled lithium niobate*. PhD thesis, University of Southampton.

Miyazawa, S. (1979). Ferroelectric domain inversion in Ti-diffused LiNbO3 optical waveguide. *Journal of Applied Physics*, 50:4599.

Mizeikis, V. (2012). Direct Laser Writing: Versatile Tool for Microfabrication of Lithium Niobate. *Journal of Laser Micro/Nanoengineering*, 7(3):345–350.

Mohan, N., Minaeva, O., Goltsman, G. N., Saleh, M. F., Nasr, M. B., Sergienko, A. V., Saleh, B. E. a., and Teich, M. C. (2009). Ultrabroadband coherence-domain imaging using parametric downconversion and superconducting single-photon detectors at 1064 nm. *Applied optics*, 48(20):4009–17.

Montaut, N., Sansoni, L., Meyer-scott, E., Ricken, R., Quiring, V., and Herrmann, H. (2017). High-efficiency plug-and-play source of heralded single photons. *Physical Review Applied*, accepted f.

Morton, J. J. L., Tyryshkin, A. M., Brown, R. M., Shankar, S., Lovett, B. W., Ardavan, A., Schenkel, T., Haller, E. E., Ager, J. W., and Lyon, S. a. (2008). Solid-state quantum memory using the 31P nuclear spin. *Nature*, 455(7216):1085–1088.

Myers, L. E., Eckardt, R. C., Fejer, M. M., Byer, R. L., Bosenberg, W. R., and Pierce, J. W. (1995). Quasi-Phase-Matched Optical Parametric Oscillators in Bulk Periodically Poled Linbo3. *Journal of the Optical Society of America B*, 12(11):2102–2116.

Nakamura, K., Ando, H., and Shimizu, H. (1987). Ferroelectric domain inversion caused in LiNbO₃ plates by heat treatment. *Applied Physics Letters*, 50(20):1413.

Nakamura, K., Kurz, J., Parameswaran, K., and Fejer, M. M. (2002). Periodic poling of magnesium-oxide-doped lithium niobate. *Journal of Applied Physics*, 91(7):4528–4534.

Nishida, Y., Miyazawa, H., Asobe, M., Tadanaga, O., and Suzuki, H. (2003). Direct-bonded QPM-LN ridge waveguide with high damage resistance at room temperature. *Electronics Letters*, 39(7):609–611.

Novikova, I., Walsworth, R. L., and Xiao, Y. (2012). Electromagnetically induced transparency-based slow and stored light in warm atoms. *Laser and Photonics Reviews*, 6(3):333–353.

Nozawa, T., Miyazawa, H., and Miyazawa, S. (1990). Water Vapor Effects on Titanium Diffusion into LiNbO3 substrates. *Japanese Journal of Applied Physics*, 29(10):2180–2185.

Prezas, P. R. and Graca, M. P. F. (2016). Structural characterization of lithium niobate nanoparticles prepared by the sol-gel process, using x-ray and Raman spectroscopy and scanning electron microscopy. In Stauffer, D. M., editor, *Applications of Molecular Spectroscopy to Current Research in the Chemical and Biological Sciences*, chapter 3, page 45. InTech.

Rarity, J. G., Tapster, P. R., and Loudon, R. (2005). Non-classical interference between independent sources. *Journal of Optics B*, 7:6.

Restoin, C., Darraud-taupiac, C., Decossas, J.-l., Vareille, J.-c., Couderc, V., and Barthe, A. (2001). Electron-beam poling on Ti:LiNbO3. *Applied Optics*, 40:6056.

Riedl, S., Lettner, M., Vo, C., Baur, S., Rempe, G., and Dürr, S. (2012). Bose-Einstein condensate as a quantum memory for a photonic polarization qubit. *Physical Review A*, 85(2):1–11.

Schmidt, R. V. and Kaminow, I. P. (1974). Metaldiffused optical waveguides in LiNbO3. *Applied Physics Letters*, 25:458.

Schwesyg, J. R. M.-l. (2011). *Interaction of light with impurities in lithium niobate crystals*. PhD thesis, Rheinischen Friedrich-Wilhelms-Universität Bonn.

Sergienko, A. V., Pittman, T. H., Strekalov, D. V., Rubin, M. H., and Shih, Y. H. (1996). Demonstration of two-photon itnerference with postponed compensation and the "quantum vernier" effect. In *European Quantum Electronics Conference*.

Smolenskii, G. A., Krainik, N. N., Khuchua, N. P., Zhdanova, V. V., and Mylnikova, I. E. (1966). The Curie Temperature of LiNbO3. *Physica Status Solidi (B)*, 13(2):309–314.

Sohler, W., Das, B. K., Dey, D., Reza, S., Suche, H., and Ricken, R. (2005). Erbium-doped lithium niobate waveguide lasers. *IEICE Transactions on Electronics*, E88-C(5):990–996.

Strake, E., Bava, G. P., and Montrosset, I. (1988). Guided Modes of Ti:LiNbO3 Channel Waveguides: A Novel Quasi-Analytical Technique in Comparison with the Scalar Finite-Element Method. *Journal of Lightwave Technology*, 6(6):1126–1135.

Sung, W. J. (2013). *Investigation of a polarization controller in titanium diffused lithium niobate waveguide near 1530nm wavelength.* PhD thesis, Texas A&M University.

Thomas, A. (2010). *Photon Pair Sources in Periodically Poled Ti:LiNbO3 Waveguides.* PhD thesis, University of Paderborn.

Thomas, A., Van Camp, M., Minaeva, O., Simon, D., and Sergienko, A. V. (2016). Spectrally engineered broadband photon source for two-photon quantum interferometry. *Optics Express*, 24(22):24947–24958.

Thomas, A., Van Camp, M. A., Fraine, A. M., and Sergienko, A. V. (2015). Low-noise Quantum Frequency Conversion in Titanium- diffused Lithium Niobate waveguide. In *Frontiers in Optics/Laser Science 2015*.

Valdivia, C. E., Sones, C. L., Mailis, S., Mills, J. D., and Eason, R. W. (2006). Ultrashort-Pulse Optically-Assisted Domain Engineering in Lithium Niobate. *Ferroelectrics*, 340(1):75–82.

Van Camp, M., Thomas, A., and Sergienko, A. (2016). Waveguided source of broadband entangled photons for quantum interferometry and sensing. In *CLEO (Conference on Lasers and Electro-Optics)*.

van der Tol, J. J. G. M. and Laarhuis, J. H. (1991). A polarization splitter on LiNbO3 using only titanium diffusion. *Journal of Lightwave Technology*, 9(7):879–886.

Williams, K. R., Gupta, K., and Wasilik, M. (2003). Etch Rates for Micromachining ProcessingPart II. *Journal of Microelectromechanical Systems*, 12(6):761–778.

Yamada, M., Nada, N., Saitoh, M., and Watanabe, K. (1993). First-order quasi-phase matched LiNbO3 waveguide periodically poled by applying an external field for efficient blue second harmonic generation. *Applied Physics Letters*, 62(5):435–436.

Ying, Y. J., Valdivia, C. E., Sones, C. L., Eason, R. W., and Mailis, S. (2009). Latent light-assisted poling of LiNbO 3. *Optics Express*, 17(21):18681–18692.

Zaske, S., Lenhard, A., and Becher, C. (2011). Efficient frequency downconversion at the single photon level from the red spectral range to the telecommunications C-band. *Optics Express*, 19(1):12825–12836.

CURRICULUM VITAE